

TOPOLOGICAL ENGINEERING AND SURFACE CHEMISTRY OF  
ULTRASMALL FLUORESCENT SILICA NANOPARTICLES FOR CANCER  
NANOMEDICINES

A Dissertation

Presented to the Faculty of the Graduate School  
of Cornell University

In Partial Fulfillment of the Requirements for the Degree of  
Doctor of Philosophy

by

Melik Ziya Turker

August 2019

© 2019 Melik Ziya Turker

TOPOLOGICAL ENGINEERING AND SURFACE CHEMISTRY OF  
ULTRASMALL FLUORESCENT SILICA NANOPARTICLES FOR CANCER  
NANOMEDICINES

Melik Ziya Turker, Ph. D.

Cornell University 2019

In the evolution of life on earth, complex biological molecules, viruses, and microorganisms have first emerged. The fascinating complexity of these biological structures at the nanoscale, with topologies varying from spheres to icosahedral objects to rings and with different surface chemistries, have always been an inspiration to scientists from a number of disciplines. Although the role of such topologies and respective surface chemistries on modulating biological response is still an open question, there have been numerous efforts in both synthesizing such nanoscale structures and their applications in medicine, particularly cancer diagnostics and therapeutics. In this dissertation, ultrasmall fluorescent silica nanoparticles with diameters around 10 nm and spherical, dodecahedral, and torus-type topologies are investigated. First, orthogonal pathways for surface functionalization of inside and outside surfaces of torus-shaped ultrasmall silica nanoparticles are explored using high-performance liquid chromatography (HPLC). Second, the formation mechanisms of ultrasmall spherical silica nanoparticles are investigated in order to minimize surface chemical heterogeneities as detected by HPLC that result from incomplete covalent encapsulation of fluorescent dye molecules. Finally, *in-vivo* studies in mice elucidate the effects of nanoparticle topology on pharmacokinetics and biodistribution.

Results suggest synthetic pathways to next generation nanomaterials for advanced applications in bioimaging and nanomedicine.

## BIOGRAPHICAL SKETCH

Melik Turker was born and raised in Trabzon, Turkey. He went to Trabzon Yomra Science High School, where he has started growing aspirations for science. After his graduation from high school, he decided to study Metallurgical and Materials Engineering upon the advice from Dr. Orhan Aydin. He earned his B.S. degree from Istanbul Technical University in 2012. He has been awarded a scholarship from Turkish Government to study abroad. He has decided to work on bio-related nanomaterials as Dr. Eyup Sabri Kayali and Dr. Mustafa Urgan advised him to do so, and he agreed. He joined Dr. Ulrich Wiesner's laboratory in Materials Science and Engineering Department of Cornell University in 2013. He earned his Master of Science degree in 2015, and Doctor of Philosophy degree on June 21<sup>st</sup> 2019, the first day of summer and his 30<sup>th</sup> birthday, on his work focused on ultras-small fluorescent silica nanoparticles for cancer diagnostics and therapeutics. He also worked in Memorial Sloan Kettering-Cornell Center for Translation of Cancer Nanomedicines (MC<sup>2</sup>TCN) as a researcher starting from 2015, and he supplied the collaboration with the synthesis of numerous types of silica nanoparticles with different surface chemistries and topologies for clinical applications. When he was not in the laboratory, he enjoyed the nature of beautiful Finger Lakes region with his friends and on his own, biking around the lakes and forests, and swimming in the gorges.

Dedicated to my mother *Hanife* and my father *Mustafa Fehmi*

## ACKNOWLEDGMENTS

Alas, thirty years is far too short to live among such excellent and admirable people, I do not know half of you half as well as I should like, and I like less than half of you half as well as you deserve. I would like to first thank my family, my parents Hanife and Mustafa, and my brothers Emre and Alperen for believing in me, and their full support, as it could have been impossible for me to even survive otherwise. I would like to thank my committee members Dr. Ulrich Wiesner, Dr. Lara Estroff, and Dr. Barbara Baird for their time and support to make this dissertation come into existence. I did not know much when I come to Cornell, and I still do not know much, and that is kind of a bummer, but yet I learned many valuable things and lessons during my stay in Ithaca, lovely town I considered home. I would like to thank Uli personally for creating an environment where I could improve myself in many different ways in academia, and his unique style as an academic advisor. I would love to thank Dr. Kai Ma for teaching me his secrets and letting me learn from him, an excellent experimentalist and a great scientist. Dr. Thomas Gardinier deserves special thanks as my comrade in the office and PhD program, and also as an HPLC guru who helped to get Cornell dots to the next level. I would like to thank Dr. Feng Chen, Dr. Brian Madajewski, and Dr. Michelle Bradbury from MSKCC, Dr. Fabio Gallazzi and Dr. Thomas Quinn from University of Missouri, Dr. William Katt, and Dr. Richard Cerione from Cornell University for being excellent collaborators to help getting Cornell dots technology potentially in use, especially in clinic. I would like to especially thank Feng for believing in the nanoparticles I synthesize, and spending his valuable time on them, it was a privilege for me to work with him. I would like to thank Fem Woodruff for being such a nice person, and her excellent help in getting work done in the laboratory, I am sure Fem will become a great scientist in the future.

I would like to thank Dr. Mahmut Aksit, and Dr. Syed Ahsan for helpful discussions and their friendship. I would like to thank my colleagues Joshua Hinckley, Rachel Lee, Jacob Erstling, Dana V. Chapman, Randal Thedford, Dr. Teresa Kao, Dr. Ferdinand Kohle, Shaun Alvarado, Ying Cong, Dr. Yao Sun, Dr. Tangi Aubert, Dr. Kasia Oleske, Dr. Yuk Mun Li, Dr. Qi Zhang, Dr. Hiroaki Sai, Naedum DomNwachukwu, Jessica Hersh, Dr. Christina “C” Cowman-Eggert, Jonathan Wang, Clara Dwyer, Kathie Lin, Henry Malarkey V, Fei Yu, and Will Tait for all the help and friendship inside and outside the laboratory. I would like to thank Nicole Wiles for her great company, friendship, and sharing the journey in the PhD program. I would like to thank Dr. Bruce van Dover for giving me the opportunity to improve myself in teaching. I would like to thank Dr. Huseyin Turker, Dr. Mehmet Akbas, and both of their families for support in my graduate studies. I would like to especially thank Dr. Murat Kara and Ahmet Emir Kara for all their, support, help, and considering me as one of their family.

I would like to thank my roommates Dr. Canbekir Bilir, Nicholas Tanen, and Mehmet Ekinici for being such great human beings. I truly enjoyed their company inside and outside 437 North Aurora #2, and learned a lot from them, it was a real privilege. I would like to thank Omer Bilgen and Dr. Gokhan Arikan for their true friendship and all the help from the beginning to the end of my graduate school experience. I would like to thank the lovely people I have met during my years in Ithaca, Dr. Radwan Tajeddine, Julia Franke, Sahar Tavakoli, and Chris Hesselbein, for sharing their friendship and precious time with me, it was truly a pleasure for me to get to know them. Sahar deserves special thanks as being such a beautiful person inside and outside, and an inspiration for the people around her, and certainly for me. I would like to thank Louise Lauritzen for her great company, cheerful personality and all the fun times we shared together. I would like to especially thank Kubra Turker,

Burak Yunus Cetin, Orkun Onal, and Dr. Yakup Yurekturk for their support and friendship, I feel lucky to have met them. I would like to thank my good friends Nora Matland, Lara Fresko, and Zeynep Saraoglu for great company, great conversations and friendship. I would like to specifically thank Emre Gonultas and Kursat Mestav for their great friendship, help, and sense of humor. I would like to gratefully thank Dr. Meryem Oznur Pehlivaner Kara, Dr. Vural Kara, Jorge Arriaza, Nagiane Lacka, Ecem Saricayir, Michael Allen, Dr. Efe Gencer, Dr. Ahmet Serdar Simsek, Brian Wiles, Dr. Gozde Arabaci, Dr. Heather Hunt, Dr. Ben Mac Murray, Dr. Deniz Gunceler, Simge Uzun, Dr. Janet Hendrickson, Aslihan Gunhan, Dr. Yucel Altug, Dr. Serhan Ardanuc, Dr. Abdurrahman Gumus, Dr. Anil Akturk, Dr. Ali Erkan, Asli Menevse, Dr. Damien Palin, Sabrina Li, Ela Correa, Nilay Duzen, Zach Rouse, Michelle Smeaton, Dr. Alex Boys, Dr. Ozan Sener, Dr. Abby Goldman, Maya Martirosyan, Mane Mehrabyan, and Matias Borg Oviedo for all their help, company, and fun times. I would like to thank Bart Feberwee, Victoria Hantout, and Ben Salinas from Gimme for pouring coffee for me at least three times a day along with our coffee drinking partner Dr. Alice Wiesner, and also David Thomas from Watershed, Chuck from Two Goats for good conversations. I would like to thank Dr. Buzz Aldrin, Che Guevara, Jeff Bridges, and Coen Brothers for being an inspiration for my work and life in general. I would like to thank the local musicians and friends including Joseph Prusch, Dr. Greg Ezra, Dr. Rebecca Couillard, Doga Tekin, Alicia Freedman, Sarah Schneider, Hanan Zaman, David “Melnick” Zakalik, Nikolai Ruskin, and Dr. Phil Robinson for the jams. I would like to thank Derin Malzeme with all its members throughout the years including Mustafa Boluk, Dr. Ridvan Gecu, Cagatay Yelkarasi, Bilgecan Cakici, Cem Selcuk, Hakan Ozkan, Selcuk Yesiltepe, Caglar Tufekcioglu, and Dr. Erdem Sesen. I would like to thank my neighbors including Dr. Theodore

Korzukhin, Dr. Michelle Kosch, Joseph Tonzola, Suzanne Scholten, and Ben from across the street, who is also a doctor.

I would also like to thank my good old friends Ozan Cavdar, Alp Cagatay Yenilmez, Hazar Erturk, Haldun Akdogan, Samet Kara, Ali Gumusel, Yunus Sarihan and Veysel Onur Ickale. Finally, I would like to thank myself, in the name of all my other great friends not mentioned here but definitely present in my heart, for keeping it real.

## TABLE OF CONTENTS

Biographical Sketch	v
Dedication	vi
Acknowledgements	vii
Table of Contents	xi
List of Figures	xii
List of Tables	xv
List of Abbreviations	xvi
<b>CHAPTER 1</b>	<b>1</b>
Introduction	
<b>CHAPTER 2</b>	<b>10</b>
Inner and Outer Surface Functionalizations of Ultrasmall and Fluorescent Silica Nanorings as Shown by High-Performance Liquid Chromatography	
<b>CHAPTER 3</b>	<b>44</b>
Controlling Surface Chemical Heterogeneities of Ultrasmall Fluorescent Core-Shell Silica Nanoparticles as Revealed by High Performance Liquid Chromatography	
<b>CHAPTER 4</b>	<b>76</b>
Ultrasmall Silica Nanoparticle Topology Modulates Biodistribution and Renal Clearance	
<b>CHAPTER 5</b>	<b>102</b>
Conclusion	
<b>APPENDIX 1</b>	<b>106</b>
Supplementary Methods	

## LIST OF FIGURES

Fig. 2.1:	Steps to orthogonally PEGylate and functionalize inside and outside surfaces of ultrasmall silica nanorings.	34
Fig. 2.2:	Molecular structures of compounds and silica networks as well as dye-silane conjugation chemistry.	35
Fig. 2.3:	Comparison between fluorescent silica nanorings with and without inner surface PEGylation.	36
Fig. 2.4:	Comparison between fluorescent silica nanorings with TMR dye functionalization inside and outside.	37
Fig. 2.5:	Comparison of fluorescent silica nanorings with increasing inner surface functionalization with TMR dye.	38
Fig. 2.6:	HPLC chromatograms of inside and outside TMR dye loaded fluorescent silica nanorings, and Cy5 dye loaded silica nanorings.	39
Fig. 3.1:	Structures of sulfonated and unsulfonated Cy5 and Cy5.5 maleimide derivatives.	65
Fig. 3.2:	HPLC chromatograms of spherical fluorescent silica nanoparticles synthesized with sulfonated and unsulfonated Cy5 and Cy5.5 maleimide derivatives.	66
Fig. 3.3:	GPC, HPLC and FCS analysis on spherical nanoparticles synthesized with unsulfonated Cy5 maleimide dye at different pH conditions.	67
Fig. 3.4:	Illustration of spherical silica nanoparticle growth via the aggregation of primary silica clusters in the presence of unsulfonated dye molecules.	67
Fig. 3.5:	GPC, HPLC and FCS analysis on spherical nanoparticles synthesized with unsulfonated Cy5.5 maleimide dye at different pH conditions.	68
Fig. 3.6:	GPC coupled HPLC chromatograms of spherical nanoparticles synthesized with unsulfonated Cy5.5 maleimide at low pH condition	70

Fig. 3.7:	Cell death experiments on MDA-MB-468 cells using spherical nanoparticles synthesized with sulfonated and unsulfonated Cy5 maleimide	71
Fig. 4.1:	Structures of different sphere, dodecahedron and torus UNP topologies with their representative TEM images.	90
Fig. 4.2:	In vivo PET imaging studies in mice comparing the PK of sphere, dodecahedron and torus UNP topologies.	90
Fig. 4.3:	TEM images of renally cleared dodecahedron and torus UNP topologies, and the illustration of deformability of torus UNP via “squeezing”	91
Fig. 4.4:	Comprehensive characterization of sphere, dodecahedron and torus UNP topologies.	92
Fig. 4.5:	TEM analysis of sphere, dodecahedron and torus UNP topologies.	93
Fig. 4.6:	Biodistribution studies for sphere, dodecahedron and torus UNP topologies.	94
Fig. 4.7:	In vivo PET imaging studies in mice comparing the PK of sphere UNP topologies with different hydrodynamic sizes.	95
Fig. 4.8:	Biodistribution studies for sphere UNPs with different hydrodynamic sizes.	96
Fig. 4.9:	Biodistribution and clearance profile for torus UNPs.	97
Fig. 4.10:	Metabolic cage study on torus UNPs showing the renal and hepatic clearance rates.	98
Fig. 4.11:	TEM image, PK profile, and biodistribution for a renally clearable 13.5 nm torus UNP sample.	99
Fig. 6.1:	Comparison of results from different HPLC methods performed on functionalized and unfunctionalized fluorescent silica nanorings.	111

Fig. 6.2:	Molecular structures and dimensions of “stretched” TMR-silane and Cy5-silane dye conjugates.	112
Fig. 6.3:	Characterization of plan silica nanorings with inside and outside Cy5 dye functionalizations.	113

## LIST OF TABLES

Table 3.1: Tabulated results of FCS analysis of the fluorescent silica 69 nanoparticles synthesized with unsulfonated Cy5 and Cy5.5 maleimide derivatives at different pH conditions.

## LIST OF ABBREVIATIONS

AA:	Amino acid
APTES:	(3-aminopropyl) trimethoxysilane
C rings:	Cornell rings
C' dots:	Cornell prime dots
Cryo-EM:	Cryogenic electron microscopy
CTAB:	Hexadecyltrimethyl ammonium bromide
Cy5:	Cyanine 5 maleimide
Cy5.5:	Cyanine5.5 maleimide
DEAC:	7-diethylaminocoumarin-3-carboxylic acid, succinimidyl ester
DFO:	Deferoxamine
DI:	Deionized
DMSO:	Dimethyl sulfoxide
EPR:	Enhanced permeability and retention
FBS:	Fetal bovine serum
FCS:	Fluorescence correlation spectroscopy
GPC:	Gel permeation chromatography
HPLC:	High performance liquid chromatography
IV:	Intravenous
MPTMS:	(3-mercaptopropyl) trimethoxysilane
MWCO:	Molecular weight cut-off
NIR:	Near-infrared
NP:	Nanoparticles
PEG:	Poly(ethylene glycol)
PET:	Positron emission tomography
PK:	Pharmacokinetics
PPSMI:	Post-pegylation surface modification by insertion
PTFE:	Polytetrafluoroethylene
RES:	Reticuloendothelial system
SWNT:	Single wall carbon nanotubes
TEM:	Transmission electron microscopy
TMB:	Mesitylene
TMOS:	Tetramethyl orthosilicate
TMR:	Tetramethylrhodamine-6 C2 maleimide
UNP:	Ultrasmall nanoparticles
UV:	Ultraviolet
%ID/g:	Injected dose per gram tissue

## CHAPTER 1

### INTRODUCTION

Cancer is an important health problem, and one of the leading causes of death all around the world.<sup>1</sup> There are many efforts to provide diagnosis and therapy solutions for cancer treatment on all fronts. Following the clinical approval of liposomes in 1995, nanomedicines have become an attractive field in cancer research.<sup>2</sup> Molecular or near molecular probes in particular, with different chemistries and functionalities are used in cancer diagnosis and therapy. Owing to their small size, such probes clear out via urinary excretion, with minimum accumulation in healthy tissues.<sup>3</sup> While generally regarded as a benefit, rapid renal excretion leads to short blood circulation half-life, limiting their ability to effectively target tumor tissues.<sup>4</sup> To overcome these shortcomings, inorganic nanoparticles like quantum dots, with enhanced optical properties for imaging, are also explored as nanoprob es.<sup>5</sup> However, these inorganic nanoparticles may end up in organs of the reticuloendothelial system (RES) like liver and spleen. Hence, surface modification with poly(ethylene glycol) (PEG) chains, a process called PEGylation, is applied for nanoparticle surface coating to reduce non-specific RES uptake by decreasing the adsorption of blood serum proteins onto nanoparticle surfaces and increasing colloidal stability.<sup>6</sup> Without the use of specific targeting moieties, nanoparticles can target tumor sites by an effect referred to as enhanced permeability and retention (EPR), which is the passive accumulation of nanoparticles at tumor sites at high concentrations due to the leaky vasculature of the

tumor environment.<sup>4</sup> The pharmacokinetics (PK) performance of quantum dots strongly depends on nanoparticle size. The cut-off for renal clearance was estimated to be somewhere between 3 and 7 nm hydrodynamic diameter.<sup>7,8</sup> This also introduces the challenge to synthesize small enough nanoparticles, and such ultrasmall nanoparticles may then clear out too fast via the renal clearance pathway, resulting in low tumor targeting efficiency.

Although, quantum dots show a stronger EPR effect than molecular probes,<sup>4</sup> depending on composition they are highly toxic, which limits their clinical use.<sup>9</sup> Single wall carbon nanotubes (SWNT) with PEG surface coating are also used for *in vivo* tumor targeting experiments and show relatively high targeting efficiency. However, RES uptake of these nanomaterials are far from being clinically relevant.<sup>10</sup> Therefore, there is a need for a nanoparticle platform combining the advantages of molecular probes and quantum dots, while still avoiding their limitations and disadvantages as much as possible to be relevant for clinical translation. These nanoparticles should have narrow size distributions and high surface chemical homogeneity, so that their PK performance and targeting efficiency would not change from batch to batch. The nanoparticle platform should allow for multimodality, combining *e.g.* fluorescence for imaging, radiolabeling for positron emission tomography (PET), surface ligands for tumor targeting, and viable surface chemistry for drug loading.<sup>4,11</sup> Such nanoparticles should also have a strong EPR effect with long blood-circulation half-life, high physiological stability, efficient renal clearance, and minimum accumulation in healthy tissues, in particular low RES uptake, to limit off-target toxicity, which would limit their use in clinic applications.

There could be many different approaches applied here, and one of them is to look into nature for inspiration. Life on earth has emerged from complex biological structures that have fascinating symmetries and specific surface chemistries.<sup>12</sup> It is still an ongoing question how such specific properties modulate biological response. Learning from the evolution of life forms on earth for over four billion years, with countless permutations and possibilities,<sup>13</sup> we can try to mimic nature for the discovery of new nanomedicines, especially for cancer diagnostics and therapeutics.<sup>14</sup> Silica nanoparticles have been one of the main building blocks for some of the oldest organisms on earth like diatoms and radiolaria, with fascinating morphologies.<sup>15</sup> It has further been shown that when using silica nanoparticles synthesized in water with ~10 nm hydrodynamic diameter, they do not induce toxicity and show low RES uptake, which is favorable for applications in nanomedicine.<sup>16,17</sup> Silica chemistry has also been proven a good platform for synthesizing mesoporous nanomaterials with different morphologies.<sup>18-21</sup> Furthermore, using silica chemistry in water, it is possible to synthesize ~10 nm fluorescent silica nanoparticles with different topologies.<sup>22-26</sup> It has been shown that final topology and surface chemistry of these nanoparticles are controlled by subtle differences in the synthesis conditions, like concentration of reactants, stirring rate, pH, or the net charge of molecules added to the synthesis.<sup>27-28</sup> Therefore, fundamental understanding of the formation mechanisms and what governs the surface chemical homogeneity of such silica nanoparticles is vital for generating the next generation cancer nanomedicines.

In this dissertation, first it is investigated how ring-type nanoparticles with torus shape can be orthogonally surface functionalized on their inside and outside surfaces. Torus nanoparticles are formed through the self-assembly of negatively charged primary silica clusters that are ~2 nm in size and that initially form through hydrolysis and condensation of silica precursors. Through electrostatic attractive interactions, these clusters arrange around positively charged surfactant micelles.<sup>26</sup> Micelle templates that direct the synthesis of these nanoparticle topologies can subsequently be removed, leaving only the silica skeleton behind that now can also be surface functionalized in regions of the rings that were formerly protected by the micelles. This opens up possibilities to orthogonally functionalize the inside and outside of the silica ring surface, depending on whether the micelle template has been removed or not. Employing polyethylene glycol (PEG) carrying silane moieties for the outer surface, and hydrophobic moieties for the inside, provides access to model systems for drug delivery. The first part of the dissertation demonstrates how high-performance liquid chromatography (HPLC) can be used to characterize such nanomaterials by providing high enough resolution to distinguish between such moieties on the ring inside or outside.<sup>28</sup>

In the absence of micelle templates, the sol-gel synthesis of silica in water as solvent medium and added fluorescent dye-silane conjugates leads to the formation of ultrasmall fluorescent core-shell silica nanoparticles with spherical shape, referred to as Cornell dots or C dots.<sup>23</sup> The net charge of the primary silica clusters first formed in solution depends on solution pH, which governs their electrostatic stability. In the sol-

gel synthesis, primary silica clusters aggregate and grow together until they reach a size, where the resulting nanoparticle is electrostatically stable at that specific solution pH.<sup>29-31</sup> In this dissertation, key synthesis conditions are next elucidated that enable full encapsulation of positively charged fluorescent dye molecules leading to spherical nanoparticle topologies of C dots with minimal surface chemical heterogeneities.<sup>28</sup> To that end, it is demonstrated that HPLC can distinguish between particles that are fully PEGylated, and particles that have hydrophobic “patches” on their surface that originate from dye molecules sitting on the silica core surface and preventing homogeneous surface coverage by the PEG layer.<sup>28</sup> Finally, in this section of the dissertation it is investigated, whether such surface patchiness modulates biological response by using a particle induced cell death mechanism recently discovered for C dots.<sup>32</sup>

In the final part of the dissertation, ultrasmall silica nanoparticles with ~10 nm hydrodynamic diameter and spherical, dodecahedral, and torus shapes are synthesized and their pharmacokinetics (PK) and biodistribution studied *in vivo* using mice models in order to elucidate the effects of particle topology on biological response. Whereas for the spherical and ring type structures protocols are used that are similar to what is described in the first sections of this dissertation, the synthesis of dodecahedral silica cages is based on a surfactant micelle directed mechanism recently discovered.<sup>25,26</sup> To the best of this authors knowledge, this is the first time that the effects of topology of such ultrasmall inorganic nanoparticles on biological response are investigated. Results are highlighting how structural characteristics of such ultrasmall vehicles can

alter properties like renal clearance and blood circulation half-times, parameters that are key for the design of advanced nanomedicines for the next generation of diagnostic and therapeutic applications.

## REFERENCES

1. Cancer Facts and Figures 2019. *U.S. Am. Cancer Soc.* **2019**.
2. Lasic, D. D.; Papahadjopoulos, D. Liposomes Revisited. *Science* **1995**, *267*, 1275–1277.
3. Gambhir, S. S. Molecular Imaging of Cancer with Positron Emission Tomography. *Nat. Rev. Cancer* **2002**, *2*, 683–693.
4. Yu, M.; Zheng, J. Clearance Pathways and Tumor Targeting of Imaging Nanoparticles. *ACS Nano* **2015**, *9*, 6655–6674.
5. Gao, X.; Cui, Y.; Levenson, R. M.; Chung, L. W. K.; Nie, S. In Vivo Cancer Targeting and Imaging with Semiconductor Quantum Dots. *Nat. Biotechnol.* **2004**, *22*, 969–976.
6. Jokerst, J. V.; Lobovkina, T.; Zare, R. N.; Gambhir, S. S. Nanoparticle PEGylation for Imaging and Therapy. *Nanomedicine* **2011**, *6*, 715–728.
7. Choi, H. S.; Liu, W.; Misra, P.; Tanaka, E.; Zimmer, J. P.; Itty Ipe, B.; Bawendi, M. G.; Frangioni, J. V. Renal Clearance of Quantum Dots. *Nat. Biotechnol.* **2007**, *25*, 1165–1170.
8. Burns, A. a; Vider, J.; Ow, H.; Herz, E.; Penate-Medina, O.; Baumgart, M.; Larson, S. M.; Wiesner, U.; Bradbury, M. Fluorescent Silica Nanoparticles with Nanomedicine 2009. *Nano Lett.* **2009**, *9*, 442–448.
9. Chen, N.; He, Y.; Su, Y.; Li, X.; Huang, Q.; Wang, H.; Zhang, X.; Tai, R.; Fan, C. The Cytotoxicity of Cadmium-Based Quantum Dots. *Biomaterials* **2012**, *33*, 1238–1244.
10. Liu, Z.; Cai, W.; He, L.; Nakayama, N.; Chen, K.; Sun, X.; Chen, X.; Dai, H. In Vivo Biodistribution and Highly Efficient Tumour Targeting of Carbon Nanotubes in Mice. *Nat. Nanotechnol.* **2007**, *2*, 47–52.
11. Truong, N. P.; Whittaker, M. R.; Mak, C. W.; Davis, T. P. The Importance of Nanoparticle Shape in Cancer Drug Delivery. *Expert Opin. Drug Deliv.* **2015**, *12*, 129–142.
12. Watson, J. D.; Crick, F. H. C. Structure of Small Viruses. *Nature* **1956**, *177*, 473–475.

13. Betts, H. C.; Puttick, M. N.; Clark, J. W.; Williams, T. a.; Donoghue, P. C. J.; Pisani, D. Integrated Genomic and Fossil Evidence Illuminates Life's Early Evolution and Eukaryote Origin. *Nat. Ecol. Evol.* **2018**, *2*, 1556–1562.
14. Geng, Y.; Dalhaimer, P.; Cai, S.; Tsai, R.; Tewari, M.; Minko, T.; Discher, D. E. Shape Effects of Filaments versus Spherical Particles in Flow and Drug Delivery. *Nat. Nanotechnol.* **2007**, *2*, 249–255.
15. Round, F., Crawford, D. *The Diatoms* Cambridge University Press, Cambridge, UK **1990**.
16. Burns, A. A.; Vider, J.; Ow, H.; Herz, E.; Penate-Medina, O.; Baumgart, M.; Larson, S. M.; Wiesner, U.; Bradbury, M., Fluorescent Silica Nanoparticles with Efficient Urinary Excretion for Nanomedicine. *Nano Lett* **2009**, *9* (1), 442–448.
17. Phillips, E.; Penate-Medina, O.; Zanzonico, P. B.; Carvajal, R. D.; Mohan, P.; Ye, Y.; Humm, J.; Gonen, M.; Kalaigian, H.; Schoder, H.; Strauss, H. W.; Larson, S. M.; Wiesner, U.; Bradbury, M. S., Clinical Translation of an Ultrasmall Inorganic Optical-PET Imaging Nanoparticle Probe. *Sci Transl Med* **2014**, *6* (260), 1-9.
18. Kresge, C. T.; Leonowicz, M. E.; Roth, W. J.; Vartuli, J. C.; Beck, J. S. Ordered Mesoporous Molecular Sieves Synthesized by a Liquid-Crystal Template Mechanism. *Nature* **1992**, *359*, 710–712.
19. Beck, J. S.; Vartuli, J. C.; Roth, W. J.; Leonowicz, M. E.; Kresge, C. T.; Schmitt, K. D.; Chu, C. T.-W.; Olson, D. H.; Sheppard, E. W.; McCullen, S. B.; et al. A New Family of Mesoporous Molecular Sieves Prepared with Liquid Crystal Templates. *J. Am. Chem. Soc.* **1992**, *114*, 10834–10843.
20. Zhao, D.; Feng, J.; Huo, Q.; Melosh, N.; Frederickson, G. H.; Chmelka, B. F.; Stucky, G. D. Triblock Copolymer Syntheses of Mesoporous Silica with Periodic 50 to 300 Angstrom Pores. *Science* **1998**, *279*, 548–552.
21. Schmidt-Winkel, P.; Lukens, W. W.; Zhao, D.; Yang, P.; Chmelka, B. F.; Stucky, G. D. Mesocellular Siliceous Foams with Uniformly Sized Cells and Windows. *J. Am. Chem. Soc.* **1999**, *121*, 254–255.
22. Ma, K.; Sai, H.; Wiesner, U. Ultrasmall Sub-10 Nm Near-Infrared Fluorescent Mesoporous Silica Nanoparticles. *J. Am. Chem. Soc.* **2012**, *134*, 13180–13183.
23. Ma, K.; Werner-Zwanziger, U.; Zwanziger, J.; Wiesner, U. Controlling Growth of Ultrasmall Sub-10 Nm Fluorescent Mesoporous Silica Nanoparticles. *Chem. Mater.* **2013**, *25*, 677–691.

24. Ma, K.; Mendoza, C.; Hanson, M.; Werner-Zwanziger, U.; Zwanziger, J.; Wiesner, U. Control of Ultrasmall Sub-10 Nm Ligand-Functionalized Fluorescent Core-Shell Silica Nanoparticle Growth in Water. *Chem. Mater.* **2015**, *27*, 4119–4133.
25. Ma, K.; Gong, Y.; Aubert, T.; Turker, M. Z.; Kao, T.; Doerschuk, P. C.; Wiesner, U. Self-Assembly of Highly Symmetrical, Ultrasmall Inorganic Cages Directed by Surfactant Micelles. *Nature* **2018**, *558*, 577–580.
26. Ma, K.; Spoth, K. A.; Cong, Y.; Zhang, D.; Aubert, T.; Turker, M. Z.; Kourkoutis, L. F.; Mendes, E.; Wiesner, U. Early Formation Pathways of Surfactant Micelle Directed Ultrasmall Silica Ring and Cage Structures. *J. Am. Chem. Soc.* **2018**, *140*, 17343–17348.
27. Turker, M. Z.; Ma, K.; Wiesner, U. B., Bimodal Morphology Transition Pathway in the Synthesis of Ultrasmall Fluorescent Mesoporous Silica Nanoparticles. *The Journal of Physical Chemistry C* **2019**, *123*, 9582-9589.
28. Gardinier, T. C.; Kohle, F. F. E.; Peerless, J. S.; Ma, K.; Turker, M. Z.; Hinckley, J. A.; Yingling, Y. G.; Wiesner, U., High-Performance Chromatographic Characterization of Surface Chemical Heterogeneities of Fluorescent Organic-Inorganic Hybrid Core-Shell Silica Nanoparticles. *ACS Nano* **2019**, *13* (2), 1795-1804.
29. Carcouet, C. C.; van de Put, M. W.; Mezari, B.; Magusin, P. C.; Laven, J.; Bomans, P. H.; Friedrich, H.; Esteves, A. C.; Sommerdijk, N. A.; van Bentem, R. A.; de With, G., Nucleation and growth of monodisperse silica nanoparticles. *Nano Lett* **2014**, *14* (3), 1433-1438.
30. Ocana, M.; Rodriguez-Clemente, R.; Serna, C. J., Uniform Colloidal Particles in Solution - Formation Mechanisms. *Advanced Materials* **1995**, *7* (2), 212-216.
31. Caruso, F.; Lichtenfeld, H.; Giersig, M.; Möhwald, H., Electrostatic Self-Assembly of Silica Nanoparticle–Polyelectrolyte Multilayers on Polystyrene Latex Particles. *Journal of the American Chemical Society* **1998**, *120* (33), 8523-8524.
32. Kim, S. E.; Zhang, L.; Ma, K.; Riegman, M.; Chen, F.; Ingold, I.; Conrad, M.; Turker, M. Z.; Gao, M.; Jiang, X.; *et al.* Ultrasmall Nanoparticles Induce Ferroptosis in Nutrient-Deprived Cancer Cells and Suppress Tumour Growth. *Nat. Nanotechnol.* **2016**, *11*, 977–985.

CHAPTER 2

INNER AND OUTER SURFACE FUNCTIONALIZATIONS OF ULTRASMALL  
AND FLUORESCENT SILICA NANORINGS AS SHOWN BY HIGH-  
PERFORMANCE LIQUID CHROMATOGRAPHY

*Abstract*<sup>1</sup>

In the past two decades, ultrasmall fluorescent nanomaterials have garnered significant interest in the fields of bioimaging and nanomedicine. More recently, attention has shifted from purely spherical nanoparticles to objects with a variety of different shapes, such as high aspect ratio, hollow, and star shaped nanomaterials. We have recently reported the synthesis and characterization of ultrasmall silica nanoparticles with complex shapes, including silica nanocages, silica nanorings, and single-pore silica nanoparticles. Here we focus on fluorescent silica nanorings that are of particular interest for theranostic applications in nanomedicine. We present in-depth studies of the synthesis and orthogonal surface functionalization successfully distinguishing the inside and outside of the silica nanorings, utilizing a combination of spectroscopic and analytical techniques including fluorescence correlation

---

<sup>1</sup> Manuscript is already published with the reference below.

Turker, M. Z.; Gardinier, T. C.; Hinckley, J. A.; Contreras, C. B.; Woodruff, F.; Ma, K.; Kohle, F. F. E.; Wiesner, U. B. Inner and Outer Surface Functionalizations of Ultrasmall Fluorescent Silica Nanorings As Shown by High-Performance Liquid Chromatography. *Chem. Mater.* **2019**. 10.1021/acs.chemmater.9b01236

spectroscopy (FCS) and reversed phase high performance liquid chromatography (HPLC). Results suggest that despite the small silica ring size around 10 nm and below it is possible to effectively “hide” hydrophobic moieties on the inside of the rings, but that their number must be carefully engineered. We expect the chemistry and methods developed here to be of interest to a range of differently shaped porous nanoparticles within the ultrasmall size regime.

### ***Introduction***

In the past two decades, the field of ultrasmall nanoparticles (NPs) with sizes below 10 nm and potential applications ranging from catalysis to nanomedicine has garnered significant interest.<sup>1-3</sup> While early efforts focused on dense spherical NPs, the field has since expanded to NPs with a variety of forms and shapes including high aspect ratio materials (*i.e.*, rods and worms), star shaped NPs, as well as nanocages.<sup>4-6</sup> These classes of NPs are distinguished from their spherical counterparts by often having multiple types of distinct surfaces, which can potentially be functionalized with different chemistries.<sup>7-9</sup> Mesoporous silica based NPs have played a crucial role in this context as the typical surfactant based template synthesis approach enables straightforward functionalization of inside and outside surfaces with orthogonal chemistries.<sup>10, 11</sup> The resulting silica nanomaterials have many advantages, including robust synthetic protocols and high potential drug payloads.<sup>10,12</sup> They do not, however, typically activate the renal pathway for rapid whole particle excretion in mammalian organisms, which requires particle diameters below the cut-off for renal clearance, *i.e.* below ~10

nm, thereby lowering the potential for adverse side effects.<sup>13,14</sup> To overcome this challenge, in addition to spherical silica NPs (SNPs) our group has recently reported the synthesis and characterization of ultrasmall SNPs with a number of different morphologies including single-pore mesoporous SNPs, silica nanorings, and silica nanocages.<sup>3,9,15,16</sup> These types of NPs are of particular interest as they provide a pathway for clinical translation as a result of proven favorable biodistribution and pharmacokinetics profiles of ultrasmall SNPs,<sup>3,17,18</sup> while simultaneously offering distinguishable “inside” and “outside” surfaces for orthogonal functionalization critical for surface directed multi-functionalization of NPs.<sup>10,19</sup> Spherical multifunctional fluorescent oxide NPs have previously been reported with only one (“outside”) surface type available for ligand conjugation,<sup>20,21</sup> but having two distinct surfaces in combination with ultrasmall particle sizes offers unique advantages, *e.g.* in therapeutic applications in nanomedicine as well as other applications such as the self-assembly of NPs.<sup>9, 22, 23</sup>

In order to take advantage of distinct surfaces such as those present in ultrasmall torus shaped mesoporous NPs or nanorings, the surface chemistry must be carefully characterized. Surface chemistry assessments of NPs remain challenging, however, as results of standard characterization techniques such as zeta potential measurements or dynamic light scattering are often limited to ensemble measurements, which do not offer a comprehensive description of the heterogeneity of surface chemical NP properties within a single sample batch.<sup>24-26</sup> In contrast to larger sized mesoporous SNPs where inside and outside surfaces are well defined, these

difficulties are exacerbated for ultrasmall NPs like silica nanorings as the distinction between inside and outside may not be straight-forward as a result of the geometry of the object (see Figure 2.1). We recently reported a method to analyze the surface chemistry of spherical ultrasmall fluorescent SNPs using high performance liquid chromatography (HPLC).<sup>27</sup> HPLC is a ubiquitous and well established technique for the characterization of small molecules, synthetic macromolecules, and proteins,<sup>28-30</sup> but before our study had not been applied for the characterization of solid inorganic core-organic ligand based core-shell NPs. Since ultrasmall NPs have sizes comparable to medium sized macromolecules/proteins, we demonstrated that HPLC in combination with gel permeation chromatography (GPC) is indeed a very powerful tool to quantitatively assess heterogeneities in surface chemical properties of spherical particles (via HPLC) and their correlations to size (via GPC).<sup>27</sup> In the present study, we apply a combination of GPC and HPLC to the characterization of fluorescent silica nanorings, mesoporous torus shaped nanomaterials with a single pore, as a test bed for attempting to differentiate between inside and outside surfaces of the rings. For convenience we will refer to these nanomaterials as Cornell rings or simply C rings. We successfully demonstrate that HPLC is a rapid and reliable screening tool capable of differentiating the locations of ligands conjugated to either of the two surfaces of these torus shaped objects. Furthermore, we observe a transition regime in which as a function of synthesis conditions the ring's inner pore becomes too crowded resulting in the ligands being pushed more and more out of the inner pore of the rings. For a given dye-ligand model, using HPLC in combination with other characterization techniques including fluorescence correlation spectroscopy (FCS), we are able to

define an upper limit of effective ligand loading to the inner surface of the nanorings. We expect that our synthesis and characterization method development, enabling first the orthogonal preparation of such ligand functionalized silica nanorings and subsequently the quantitative characterization of the distribution of ligands between inside and outside surfaces of such ultrasmall torus shaped SNPs, will be of interest to other NP systems. Furthermore, the specific silica nanorings described herein constitute interesting vehicles for theranostic, *i.e.* combined therapeutic and diagnostic, applications in nanomedicine in general, and oncology in particular.

### ***Materials***

All materials were used as received. 7-diethylaminocoumarin-3-carboxylic acid, succinimidyl ester (DEAC), and tetramethylrhodamine-6 C2 maleimide (TMR) were purchased from Anaspec. Cyanine5 maleimide (Cy5) with net positive charge was purchased from Lumiprobe. Sulfo-Cyanine5 maleimide (sulfo-Cy5) with net negative charge was purchased from Click Chemistry Tools. Hexadecyltrimethyl ammonium bromide (CTAB,  $\geq 99\%$ ), tetramethyl orthosilicate (TMOS,  $\geq 99\%$ ), 2.0 M ammonium hydroxide in ethanol, and anhydrous dimethyl sulfoxide (DMSO,  $\geq 99\%$ ) were purchased from Sigma Aldrich. (3-aminopropyl) trimethoxysilane (APTES), 2-[methoxy (polyethyleneoxy) 6-9propyl] trimethoxysilane (PEG-Silane, 6-9 ethylene glycol units), (3-mercaptopropyl) trimethoxysilane (MPTMS, 95%), and methoxy triethyleneoxy propyl trimethoxysilane (PEG-silane, 3 ethylene glycol units) were obtained from Gelest. Mesitylene (TMB, 99% extra pure) was purchased from Acros

Organics. Absolute anhydrous ethanol (200 proof) was purchased from Koptec. Glacial acetic acid was purchased from Macron Fine Chemicals. 5.0 M sodium chloride irrigation USP solution was purchased from Santa Cruz Biotechnology. Syringe filters (0.2  $\mu\text{m}$ , PTFE membrane) were purchased from VWR International. Vivaspin sample concentrators (MWCO 30K) and Superdex 200 prep grade were obtained from GE Health Care. Snakeskin dialysis membrane (MWCO 10K) was purchased from Life Technologies. Deionized (DI) water was generated using Millipore Milli-Q system (18.2 M $\Omega$ .cm). Glass bottom microwell dishes for FCS were obtained from MatTek Corporation. Carbon film coated copper grids for TEM was purchased from Electron Microscopy Sciences. UHPLC grade acetonitrile was purchased from BDH. Xbridge Protein BEH C4 Column (300 Å, 3.5  $\mu\text{m}$ , 4.6 mm X 150 mm, 10K-500K) and BioSuite. High Resolution SEC Column (250 Å, 5  $\mu\text{m}$ , 7.8 mm X 300 mm, 10K – 500K) were purchased from Waters Technologies Corporation. Trifluoroacetic acid was purchased from Neta Scientific.

### ***Conjugation of Fluorescent Dyes DEAC, TMR, and Cy5***

For a 10 mL batch reaction, 0.2  $\mu\text{mol}$  succinimidyl ester derivative of DEAC dye was conjugated with 5  $\mu\text{mol}$  APTES (1:25 ratio) in 100  $\mu\text{L}$  DMSO for the synthesis of C rings that have DEAC dye covalently encapsulated in the silica matrix. For inner or outer surface dye functionalization of a 10 mL reaction batch, 0.4  $\mu\text{mol}$  of maleimido derivative of TMR dye was conjugated with 10  $\mu\text{mol}$  of MPTMS (1:25

ratio), and 0.18  $\mu\text{mol}$  of Cy5 was conjugated with 4.2  $\mu\text{mol}$  MPTMS (1:23 ratio) in 100  $\mu\text{L}$  DMSO. All of the dye conjugations were made one-day prior to their use in the synthesis by mixing the components by pipette and leaving the solution overnight in the glovebox.

### ***Synthesis of PEGylated Fluorescent C Rings***

Fluorescent C rings were synthesized in aqueous solution using surfactant-micelles templating the silica condensation. For a 10 mL batch reaction, 83 mg of CTAB was dissolved in 9 mL deionized water, and 1 mL of ammonium hydroxide solution (0.02 M) was added to the reaction in a 25 mL round-bottom flask. The solution was stirred at 600 r.p.m. at 30°C for 30 minutes before the addition of 100  $\mu\text{L}$  TMB to expand the micelles, which was followed by stirring for 1 hour. Afterwards, 68  $\mu\text{L}$  TMOS and 100  $\mu\text{L}$  DEAC dye-conjugate was added into the solution in subsequent steps, and the reaction was left stirring overnight at 30°C. The following day, 100  $\mu\text{L}$  PEG-silane (6-9 ethylene glycol units) was added into the 10 mL reaction under stirring at 600 r.p.m., and the solution was left stirring overnight at 30°C. The concentrations of TMOS, CTAB, TMB, and PEG-silane were approximately 45.6 mM, 22.7 mM, 71.9 mM, and 21.5 mM, respectively. The next day after PEG-silane addition, the sample solution was heated at 80°C overnight without stirring in order to enhance covalent PEG-silane condensation.<sup>31</sup>

### ***Purification of C Rings***

The day after 80°C heating, the solution was cooled down to room temperature, syringe-filtered (MWCO 0.2 μm, PTFE), and transferred into a dialysis membrane (MWCO 10K). Then the sample was dialyzed in 200 mL of ethanol/deionized water/glacial acetic acid solution (500:500:7 volume ratio), and the acid solution was changed once a day for three days to remove/etch CTAB from the pores of the C rings (micelle removal), and to remove unreacted reagents from the sample. Following the acid dialysis, the sample was transferred into 5 L deionized water, and the water was refreshed once a day for three days to remove ethanol and acetic acid solvents.

### ***Synthesis of Inner Surface-Pegylated Fluorescent C Rings***

Following all of the purification and CTAB micelle removal steps to have the C ring pores accessible for inner surface functionalization, 400 μL of PEG-silane (3-ethylene glycol units) was added into 10 mL of the C ring native synthesis solution (estimated concentration 6 μM) in a 25 mL round-bottom flask under stirring at 600 r.p.m. at room temperature. The solution was left stirring overnight. The concentration of PEG-silane (3-ethylene glycol units) was roughly 142 mM.

### ***Synthesis of Inner Surface-Dye-Functionalized Fluorescent C Rings***

Following all of the purification steps and CTAB micelle removal steps to have the C ring pores accessible for inner surface functionalization, 100  $\mu\text{L}$  of TMR-silane conjugate in DMSO was added into 10 mL of native C ring synthesis solution in a 25 mL round-bottom flask under stirring at 600 r.p.m., and room temperature overnight. The concentration of TMR dye was roughly 40  $\mu\text{M}$ . For the dye-loading series experiments, TMR concentrations were varied between 10  $\mu\text{M}$  to 120  $\mu\text{M}$  (see main text).

### ***Synthesis of Outer Surface-Dye-Functionalized Fluorescent C Rings***

Following the same procedure for the first day of the fluorescent C ring synthesis described above, 100  $\mu\text{L}$  of the TMR-silane conjugate DMSO solution described in the previous section was added into 10 mL of native C ring synthesis solution (with C rings still containing the CTAB micelles), just before the addition of PEG-silane (6-9 ethylene glycol units) to the outer surface of the rings in a 25 mL round-bottom flask under stirring at 600 r.p.m. at room temperature.

### ***Synthesis of Inner/Outer Surface-Dye-Functionalized Blank C Rings***

For the synthesis of inner/outer surface-dye-functionalized blank C rings, the addition of conjugated DEAC dye was skipped after the addition of TMOS on the first day of synthesis, so that the blank nanorings were formed without the encapsulation of fluorescent DEAC dyes in the silica matrix. Replacing the TMR dye-conjugate with

Cy5 dye-conjugate for functionalization, inner/outer surface-dye-functionalization procedures described above were followed. The concentration of Cy5 dye for both inner and outer-surface-functionalization was 18  $\mu$ M.

### ***Gel Permeation Chromatography (GPC)***

Following the dialysis step, the solutions were concentrated using spin filters (Vivaspin 20 MWCO 30K) in centrifugation (Eppendorf 5810R) at 4300 r.p.m. for 45 min. 400  $\mu$ L of the up-concentrated sample were injected into GPC column packed with Superdex 200 prep grade resin using 0.9 wt. % sodium chloride saline as buffer solution. Bio-Rad BioLogic LP system was used to operate the GPC column at 2 mL/min flow rate, and Bio-Rad BioFrac was used to collect the GPC fractions of the samples at 14 sec/fraction times absorbing at 275 nm. C rings were separated from the aggregation products and un-reacted reagents via GPC fractionation, and collected samples were run in GPC again to check sample purity via the single-peak particle distribution. These are the GPC control runs reported in the main text to demonstrate sample purity.

### ***High Performance Liquid Chromatography (HPLC)***

All HPLC runs were carried out on a Waters Alliance 2965 separations module equipped with a column heater, and a Waters 2996 photodiode array detector. The hardware was controlled by a computer running Empower 3 Feature Release 3.

Deionized water was generated from a Millipore IQ7000 water system (18.2 M $\Omega$  resistivity) and acetonitrile was obtained from BDH (UHPLC grade). The columns used were 150 mm Waters Xbridge BEH C4 Protein separation columns with 300 Å pore size and 3.5  $\mu$ m particle size and 50 mm Waters Xbridge BEH C18 Protein separation columns with a 300 Å pore size and 3.5  $\mu$ m particle size. All injections were 10  $\mu$ L of 15  $\mu$ M nanorings. Concentrations for injected samples were determined by FCS. For additional information please see Supporting Information.

### ***Transmission Electron Microscopy (TEM)***

TEM samples were prepared by dropping  $\sim$ 8  $\mu$ L of the sample solution diluted in ethanol onto a carbon film coated copper TEM grid, and letting the sample air-dry on the grid on a filter paper. Dry-state TEM images were taken using FEI Tecnai T12 Spirit microscope operated at 120 kV. Cryogenic electron microscopy (cryo-EM) was performed on a ring sample as described in the literature.<sup>9</sup>

### ***Fluorescence Correlation Spectroscopy (FCS) Of Fluorescent C Rings***

Fluorescence correlation spectroscopy (FCS) measurements were performed on C rings encapsulating DEAC dye, using a home-built FCS setup with HeNe 445 nm excitation source. FCS samples were prepared by diluting samples in water on a glass-bottom microwell dish. Photons were collected by an avalanche photodiode detector (SPCM 14, Perkin-Elmer). The photocurrent from the detector was digitally

auto-correlated with a correlator card (Correlator.com). Before each set of measurements, the focal/observation volume was calibrated with 6CR110 as standard dye such that the ratio of the radial to the axial radii of the focal volume is between 0.1 and 0.2. FCS auto-correlation curves were analyzed to obtain the hydrodynamic size, brightness per particle, and the concentration of the samples as described in previous publications.<sup>32, 33</sup> For additional information please see Supporting Information.

### ***Steady State Absorption Spectroscopy***

Varian Cary 5000 spectrophotometer was used to measure the absorption spectra of the samples in parallel to FCS measurements to calculate the number of dyes per particle as described in equation 3 below. To acquire the absorption spectra, first a baseline subtraction against 3 mL of fresh deionized water in a quartz cuvette was performed. After the blank was measured the sample was added directly to the cuvette and an absorption spectrum was acquired. The absorbance maxima of each sample were kept within the linear region of the Beer-Lambert Law for concentration determinations and further calculations as detailed in the Supporting Information.

### ***Results and Discussion***

#### ***Orthogonal Pathways to Inner and Outer C Ring Surface Functionalization***

In recent reports we have provided the full description of the synthesis approach to, and possible formation mechanism supported by in-depth structural

characterization of, surfactant micelle mediated formation of ultrasmall fluorescent silica nanorings (C rings).<sup>9,34</sup> Figure 2.1 shows representative cryo- and transmission electron microscopy (cryo-EM/TEM) images of planar and edge-on views of a silica nanoring formed around a TMB swollen CTAB micelle, originally used to unambiguously establish the ring geometry.<sup>9</sup> Since the inner surface of C rings in the surfactant mediated synthesis is originally shielded/covered by the surfactant micelle as illustrated in Figure 2.1, this micelle-directed formation mechanism should enable orthogonal functionalization of inner and outer C ring surfaces. As discussed in great detail in our original paper first disclosing this ultrasmall ring structure,<sup>9</sup> this effect is enhanced by partial wrapping of the TMB swollen micelle around the ring, driven by electrostatic attraction between the positively charged micelle surface (from quaternary ammonia surfactant head groups) and the negatively charged silica surface (from deprotonated Si-OH groups). After C ring synthesis as described in the Methods section, the inner surface is still covered by the micelle, while the outer bare silica surface is available for coating with a poly(ethylene glycol) layer (PEGylation step) and/or functionalization with other moieties as described in detail in earlier studies on conventional spherically shaped fluorescent core-shell SNPs with sizes below 10 nm referred to as Cornell dots or simply C dots.<sup>31,35</sup> Once the outer silica surface is covered with these moieties, removal/etching of the surfactant micelles *via e.g.* dialysis in acidic solutions (see Methods section) exposes bare inner silica surface, which can subsequently be functionalized in an orthogonal fashion with other moieties of interest. Possible steps of such orthogonal functionalization schemes are schematically depicted in Figure 2.1, while the molecular structures of all chemical

compounds used in the reactions described in this study are shown in Figure 2.2. In order to render the original C rings fluorescent for simple optical detection we chose to work with the succinimidyl ester of 7-diethylamino-coumarin-3-carboxylic acid (DEAC-dye), which has an absorption maximum around 440 nm, *i.e.* in the blue. This dye molecule can conveniently be reacted with APTES to provide a dye-silane conjugate (Figure 2.2d), which as a result of its neutral charge state and small size (MW ~350 g/mole) in turn should get covalently encapsulated reasonably well into the matrix of the silica rings.<sup>27</sup> DEAC-dye containing rings are therefore rendered in blue in all figure schematics of this study.

In a first set of experiments to examine orthogonal functionalization pathways, the inner surface of silica nanorings, outer-surface functionalized with a PEG-silane with 6-9 EO units, was either left naked or PEGylated using a 3 EO-chain length PEG-silane (Figure 2.2b). The same ring synthesis batch was used for the preparation of these two samples in order to minimize the effects of batch to batch synthesis variations. To that end, a mother batch was synthesized by taking the as-prepared C rings and PEGylating their outer silica surface. An aliquot of this batch was simply submitted to surfactant micelle removal/etching providing C rings with a bare inner surface, while a second aliquot underwent inner surface PEGylation after micelle etching. After final purification steps (see Methods section), in order to establish a baseline study, these two C ring samples underwent in-depth characterization via a combination of techniques (Figure 2.3) including FCS, GPC, absorption spectroscopy, HPLC, and TEM. FCS results (Figure 2.3a) suggested identical hydrodynamic sizes of

9.1 nm for both samples, corroborated by single-peak distributions and equal elution times in GPC (Figure 2.3b). A slightly higher absorption in the UV region of absorption spectra normalized to the 440 nm DEAC dye absorption maximum (Figure 2.3c) and characteristic for the presence of PEG,<sup>21</sup> was consistent with successful inner surface PEGylation of the C rings (but may also indicate insertion of additional smaller PEG moieties between existing PEG chains on the outer surface). Results of HPLC runs showed that both C rings elute at the same time and with similar peak shapes (Figure 2.3d), suggesting that in this particular case of simple PEG coating of the inner surface versus bare silica, HPLC is not very sensitive to the details of the inner surface chemical properties. The shape and fine structure of the HPLC chromatograms with multiple peaks on a curve that first rises sharply and then tapers off at longer times are very similar to those observed for conventional PEGylated fluorescent C dots suggesting incomplete encapsulation of one or more DEAC dyes leading to hydrophobic patches that prolong the corresponding elution times relative to a fully PEGylated surface.<sup>27</sup> Since the focus of the present study was a comparison of C rings with different inner and outer surface functionalities, we did not try to resolve these dye encapsulation details any further but rather used HPLC as a qualitative tool to compare different functionalized C rings. Finally, as expected TEM images of the two C ring batches showed no discernible differences in particle morphology (compare Figure 2.3e and 2.3f).

### ***Inner and Outer C Ring Surface Functionalization with TMR Dye as Revealed by HPLC***

Next, we functionalized either the inner or the outer surface of aliquots of the mother batch with zwitter-ionic (*i.e.* zero net charge) tetramethyl-rhodamine (TMR) dye, which has an absorption maximum around 550 nm, well separated from that of the DEAC dye around 440 nm encapsulated into the silica ring matrix (*vide supra*). To that end, TMR-silane was first generated from reaction of the maleimido derivative of TMR with mercaptopropyl-trimethoxysilane (MPTMS, Figure 2.2e). This dye derivative was then added to an aliquot of the mother batch either shortly before addition of the PEG layer on the outer surface in the presence of the CTAB micelles covering the inner surface or after this PEGylation step and micelle removal thereby functionalizing the inner ring surface with TMR dye (see Method section). In both cases, TMR-silane was added at the same concentration (40  $\mu$ M). Comparison of characterization results of these two C ring batches is shown in Figure 2.4. Figure 2.4a and c shows FCS correlation curves of inner (red) and outer (blue) surface functionalized batches, respectively (*i.e.* carrying TMR dye either on the inner or outer surface while both encapsulating DEAC dye in the silica ring matrix), plotted against those of unfunctionalized C rings (DEAC dye carrying rings only, see Figure 2.3a). FCS data analysis suggested that the hydrodynamic particle size for the inner surface functionalized C rings increased from 9.1 nm to 10 nm, while that for the outer surface functionalized rings increased from 9.1 nm to 11.1 nm when compared to the reference nanoring without TMR. Both functionalized samples showed a single-peak

distribution in GPC (Figure 2.4b). The outside functionalized C rings (blue) were slightly more size dispersed, which correlates with the slightly larger size increase observed in FCS. When comparing absorption spectra of the two TMR functionalized ring batches normalized to the 440 nm absorption of the DEAC dye (Figure 2.4d), even though TMR-silane was added at the same concentration for both samples it is apparent from the higher TMR absorption observed around 550 nm that there are substantially more TMR dyes on the outer (blue) than on the inner (red) surface. Combining information from FCS on particle concentration with these absorption results (see Methods), the number of TMR dyes per C ring was determined to be 4.5 and 1.8 for outer and inner surface functionalization, respectively, correlating well with the larger size for the former as detected by FCS. This higher dye number could be explained by the larger surface area available on the outside of the C rings, which translates into the availability of more surface silanol groups for TMR dye-silane attachment, as well as the higher accessibility of the outer versus the inner ring surface which suggests steric hindrance of TMR functionalization of the inner surface once the first TMR dye is in place.

In addition to larger hydrodynamic C ring size from higher TMR dye numbers on the outer ring surface relative to the inner surface, HPLC chromatograms collected with read out at 550 nm, the TMR dye absorption maximum, also showed substantial differences between these two batches (Figure 2.4e). Compared to the inner surface functionalized C rings (red), the outer surface-functionalized rings (blue) had a wider distribution and tailing that indicates substantially increased nanoring hydrophobicity.

Furthermore, using the 440 nm read out channel matching the DEAC dye absorption, HPLC results (Figure 2.4f) highlight that the inner surface-functionalized nanorings (red curve) eluted at more similar times and exhibited a more similar elution profile to C rings with no inside or outside surface functionality (black curve) as compared to the outside functionalized rings (blue). These results establish that in contrast to outer surface conjugations, functionalizing the inner ring surface with hydrophobic moieties, here TMR dyes, effectively “hides” these molecules in the pore of these ultrasmall nanorings, thereby shielding them from interactions with their environment. Taken together, the preceding results unambiguously demonstrate that we are able to selectively functionalize the inner versus the outer surface of ultrasmall silica nanorings, and that HPLC is a powerful experimental tool to differentiate between these two functionalization sites. In addition to the relatively rapid (short elution times) screening HPLC method (referred to as Method 2) employed here, we also applied our previously developed more quantitative HPLC method (referred to as Method 1 with longer elution times)<sup>27</sup> to both ring samples described in Figures 2.3 and 2.4. These studies summarized in Supplemental Figure 6.1 in Appendix 1 demonstrate that for DEAC and TMR functionalized rings HPLC results were robust against changes in both the HPLC parameters and columns. This is encouraging as it suggests that a variety of HPLC separation methods may be successful in differentiating between these types of chemical differences and that it may be possible to extend these chromatographic methods to other ultrasmall nanomaterial compositions and morphologies.

### ***Assessing “Effective” Inner Ring Surface Loading Capacity by HPLC***

The ability to distinguish between inner and outer surface functionalization via HPLC allowed us to determine an “effective” cargo loading capacity of the inner surface of C rings, *i.e.* the loading capacity for which a particular hydrophobic cargo can effectively be “hidden” in the pore. The loading capacity is a crucial parameter, *e.g.* in the context of the delivery of drugs and other pharmaceutically relevant molecules to sites of disease. Once the effective loading capacity of the inside surface of the nanorings is reached, further functionalization may still occur, but only on the outer surface of the nanorings exposing the cargo to interactions with the environment. In order to assess this quantity, the inner surface of C rings encapsulating DEAC dye in their silica matrix were functionalized employing increasing concentrations of TMR-silane (10  $\mu\text{M}$ , 30  $\mu\text{M}$ , 80  $\mu\text{M}$ , and 120  $\mu\text{M}$ ) using the same approaches as described before (see Methods). With a silica wall thickness of only around 2 nm, nanoring pore size of around 6 nm, and TMR-silane conjugate size of somewhere between 2-3 nm (Supplemental Figure 6.2 in Appendix 1), *i.e.* roughly equal to pore radius, as illustrated in Figure 2.5a we expected to see TMR dye being pushed towards the outside of the nanorings as the number of TMR dyes per nanoring increases beyond two (Figure 2.5a). This is consistent with what was experimentally observed *via* HPLC. Analysis of FCS measurements (Figure 2.5b) combined with that of absorption spectra (Figure 2.5c) normalized to the 440 nm DEAC dye peak of the four C ring samples obtained from increasing TMR-silane precursor in the synthesis suggested increasing hydrodynamic sizes of 9.6 nm, 10.4 nm, 10.7 nm and 11.0 nm as

well as 1.0, 2.2, 3.5 and 6.5 TMR dyes per nanoring, respectively. The associated GPC distributions got progressively more disperse as the number of TMR-silane per nanoring increased (Figure 2.5d). In the corresponding HPLC chromatograms taken at 440 nm (DEAC dye) and 550 nm (TMR dye) read out, see Figure 2.5e-f, respectively, relative to the unfunctionalized rings (black curve in Figure 2.5e) we saw increasing shifts and tailing towards longer elution times/more hydrophobic behavior, in particular for C rings with more than 2 dyes per particle. As schematically illustrated in Figure 2.5a, this suggests a shift from well-hidden TMR dyes in the pore to more and more TMR dyes exposed to the outside leading to increasingly hydrophobic nanoring behavior. Once the ring pore is significantly overloaded, the cargo is exposed to the outside so much that these inner-functionalized rings become more hydrophobic than outside functionalized rings. This is demonstrated in Figure 2.6a where HPLC traces from a ring with 6-7 TMR molecules on the inside begin eluting at later retention times as compared to a ring with 4-5 TMR molecules on the outside (see schematic) suggesting more hydrophobic character for the inner functionalized ring. This result demonstrates the critical importance of elucidating the “effective” loading capacity of the ring pore, as overloading the ring pore renders the vehicle more hydrophobic than functionalization of the outside surface. It is important to note, that the rings overloaded on the inside are likely more hydrophobic than the outside functionalized rings because hydrophobic ligands on the outside may benefit from partial shielding by the hydrophilic PEG layer. The inside surface was left unPEGylated so that hydrophilic versus hydrophobic behavior depended primarily on

localization and “hiding” of the hydrophobic cargo within the pore, which we wanted to elucidate.

### ***HPLC Derived Effective Inner Ring Loading Capacity as a Function of Cargo Size and Charge***

One would expect that the effective inner ring loading capacity is sensitive to the size of the hydrophobic cargo relative to the pore size. In other words, the larger the hydrophobic cargo the more difficult it is to hide it on the inside of the single pore of the ring. In order to test this hypothesis, we functionalized inner and outer surfaces of C rings with a Cy5 derivative of net positive charge (see Methods and Figure 2.2f), a fluorescent dye belonging to the cyanine dye family that is larger than TMR (see Supplemental Figure 6.2 in Appendix 1). Both inner and outer surface functionalized samples carried the same number of Cy5 dyes ( $n=3.2$  from FCS/UV-vis, see Supplemental Figure 6.3 in Appendix 1) thus removing the need for DEAC as a reference dye (*i.e.* no DEAC dye was used in the silica ring matrix, see synthesis of blank C rings in *Experimental Section*). As a first indication, fully characterized rings with an equal number of Cy5 dyes either on the ring inside or outside showed an increase in the left absorption shoulder of Cy5 around 600 nm for the inner surface functionalized material (red data set). Since this shoulder is sensitive to dye aggregation,<sup>36</sup> this result is consistent with dye crowding on the inside (Supplemental Figure 6.3c in Appendix 1). When applying our qualitative HPLC screening method (Method 2 in Figure 6.1 in Appendix 1) to these inside and outside surface

functionalized rings, chromatograms for rings with 3 Cy5 dyes on the inside started to elute at later times than those with Cy5 on the outside, suggesting more hydrophobic behavior (Figure 2.6b), consistent with dye overloading effects of the inner ring surface already becoming predominant for dye numbers as low as 3. Moreover, comparing this effect for Cy5 with the results for TMR (Figure 2.6a) reveals larger onset shifts between the two chromatograms for Cy5 consistent with the expected size effect. It is interesting to note that overall the position of both Cy5 chromatograms is shifted to smaller retention times relative to the two TMR traces. We believe this overall shift is due to the absence of DEAC in the Cy5 modified rings, supported by the fact that the HPLC peak structure and tailing to larger retention times observed in Figure 2.3d is all due to DEAC only partially incorporated into the silica matrix of the C rings thereby rendering these rings more hydrophobic than their undyed counterparts (*vide supra*).

We finally tried to functionalize the blank C rings using a Cy5 dye derivative with net negative charge. While this worked for the outer surface, it did not for the inner surface of the nanorings (data not shown). This is most likely due to repulsive electrostatic interactions between the negatively charged Cy5 dye and the negatively charged naked inner surface of C rings (from deprotonated silanol surface groups), an affect that is screened by the PEG chains on the outer surface. As shown above, neither zwitterionic TMR dye that is charge neutral nor positively charged Cy5 (Supplementary Figure 6.2 in Appendix 1) suffered from this problem further supporting this interpretation.

## ***Conclusion***

In this study we synthesized a class of non-spherical ultrasmall fluorescent silica nanoparticles in the form of rings (C rings) that were surface functionalized on chemically and spatially distinct inner and outer surfaces, respectively. We demonstrated that reversed phase HPLC is a sensitive tool able to distinguish between samples orthogonally functionalized on these surfaces with model dye-silane conjugates of different hydrophobicity, size, and charge. Results suggest that despite the small silica hydrodynamic ring size of 10 nm and below it is possible to “hide” hydrophobic moieties on the inside of the rings, but that to accomplish this effectively their number must be carefully engineered. We expect the class of ultrasmall nanorings described here to be of relevance for both diagnostic and drug delivery applications in nanomedicine. Furthermore, we anticipate that the chromatographic methods developed to characterize multiple spatially and chemically distinct surface chemistries on these nanoparticles will be applicable to a range of differently shaped porous nanoparticles within the ultrasmall size regime.

## *Acknowledgements*

This work was funded by the National Cancer Institute of the National Institutes of Health (NIH) under Award Number U54CA199081. HPLC and GPC experiments were supported by MC<sup>2</sup>TCN Center for Cancer Nanotechnology Excellence, which is also supported by NIH under Award Number U54CA199081. We thank John Grazul, and the Cornell Center for Materials Research (CCMR) for use of the electron microscopy facilities, which are supported by the National Science Foundation MRSEC program under Award Number DMR-1719875. Melik Turker thanks the Ministry of National Education of the Republic of Turkey for his student scholarship support. The authors gratefully thank Katherine Spoth, and Lena Kourkoutis for cryo-EM help. Melik Turker, Thomas Gardinier, Kai Ma, and Ulrich Wiesner designed experiments. Melik Turker, Joshua Hinckley, and Ferdinand Kohle performed FCS measurements. Melik Turker, Fem Woodruff, and Cintia Contreras synthesized fluorescent nanorings. Thomas Gardinier developed methods and performed HPLC. Melik Turker performed TEM.

## Figures

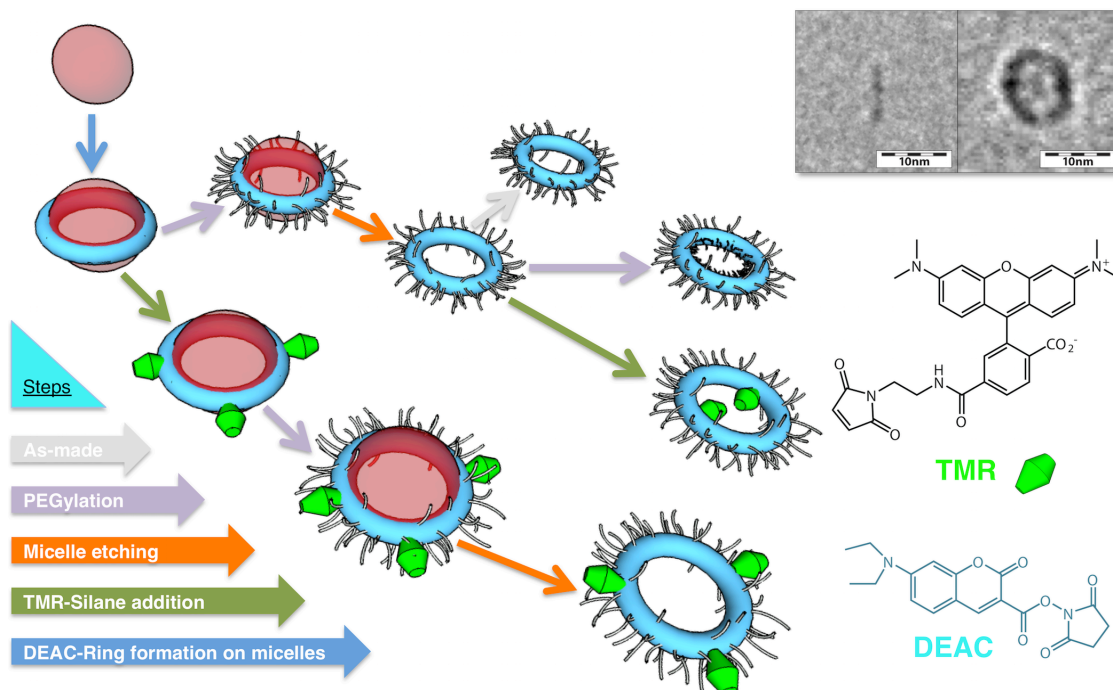


**Figure 2.1:** Steps (bottom left, not in representative sequence) to orthogonally PEGylate and functionalize inside and outside surfaces of ultrasilica nanorings. Surfactant micelles represented in red (top left) act as templates for silica nanoring growth (blue arrow), simultaneously encapsulating DEAC dye in the silica matrix. After dyed silica nanoring formation, individual steps along two different pathways are taken in order to be able to specifically PEGylate and/or functionalize the outside (bottom sequence) and inside (top sequence) surfaces of the rings. Individual steps include PEGylation (purple arrows), micelle removal (orange arrows), and TMR-silane additions (green arrows). Representative cryo-EM/TEM images show two orthogonal projections of a silica nanoring (edge on, left; planar, right) formed around a TMB swollen CTAB micelle (top right).

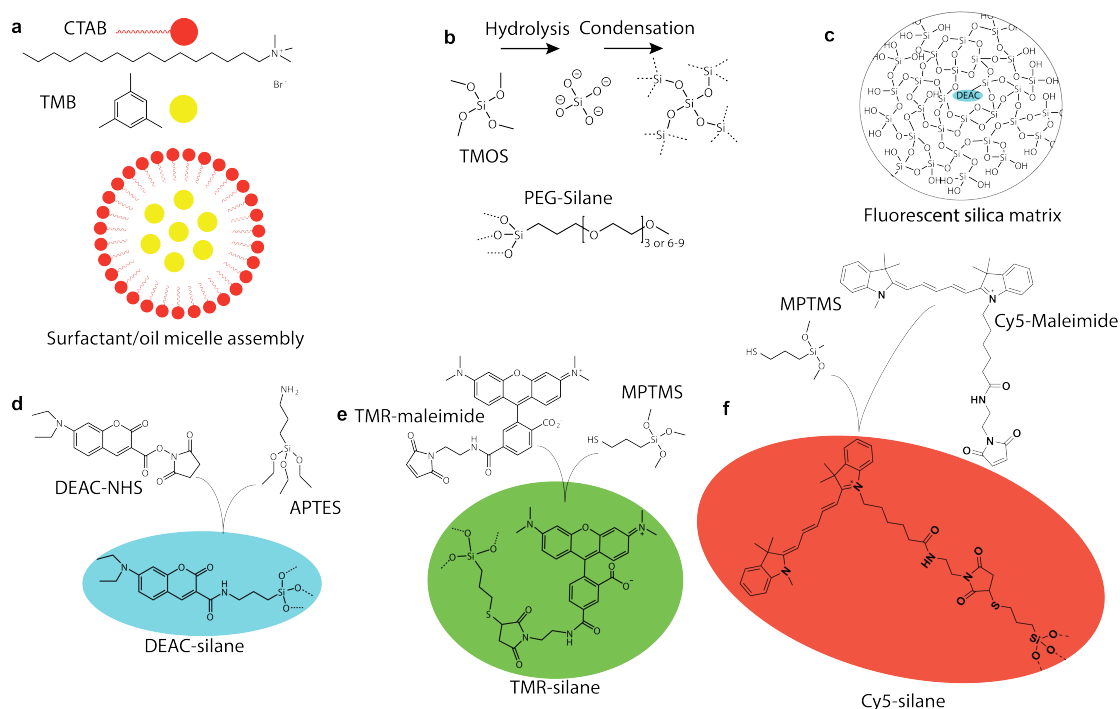


**Figure 2.2:** Molecular structure of compounds and silica networks as well as dye-silane conjugation chemistry. (a) Chemical structures of surfactant (CTAB) and oil-pore expander (trimethyl benzene, TMB). (b) Hydrolysis and condensation steps of silica precursor (TMOS), and chemical structure of PEG-silane molecule. (c) Molecular rendering of DEAC dye encapsulating silica matrix. (d,e,f) Conjugation of succinimidyl ester derivative of DEAC dye with aminopropyl-silane (d), as well as maleimido derivatives of TMR (e) and Cy5 dye (f) with mercaptopropyl-silane.

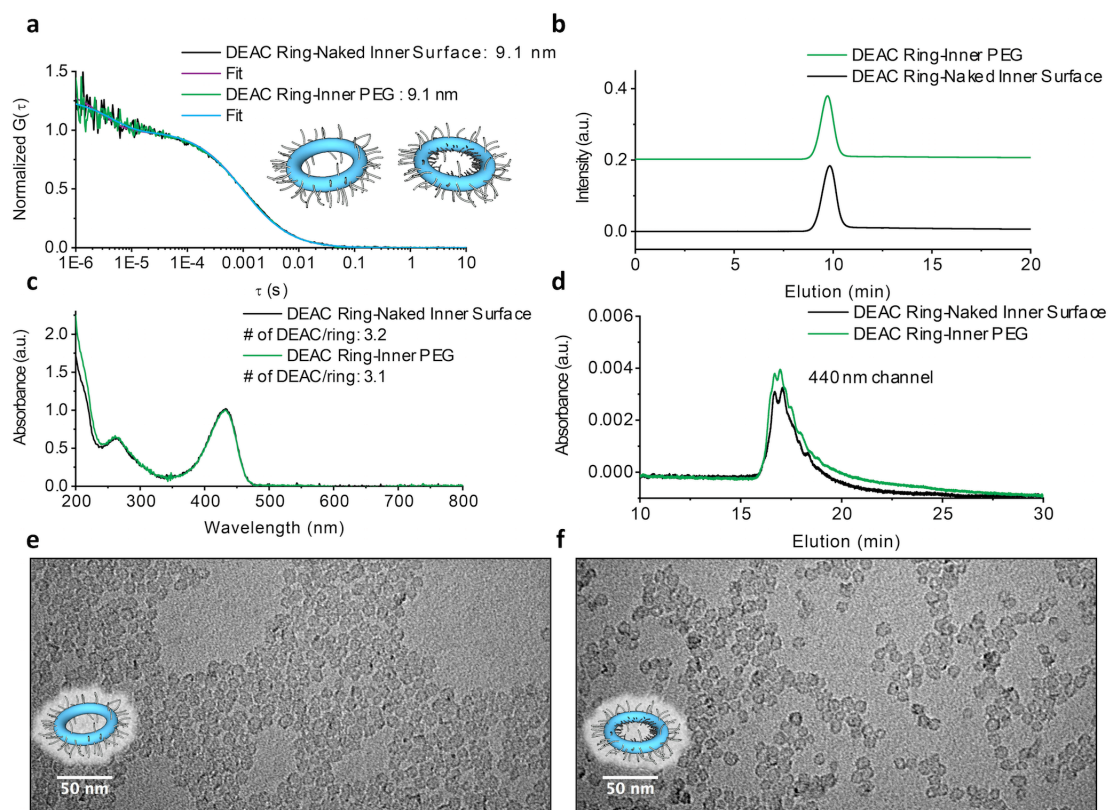


**Figure 2.3:** Comparison between fluorescent silica nanorings (DEAC-rings) with (green) and without (black) inner surface PEGylation (with 3 EO containing PEGs). (a) FCS auto-correlation curves suggesting 9.1 nm hydrodynamic sizes for both samples. (b) Analytical scale GPC chromatograms of both samples. (c) Absorption spectra for the naked and inner surface PEGylated DEAC-rings, suggesting (together with FCS results) 3.2 and 3.1 DEAC dyes per silica nanoring, respectively. (d) HPLC chromatograms at 440 nm read out channel (DEAC dye absorption). (e,f) TEM images of DEAC-rings with naked (e), and PEGylated (f) inner surfaces.

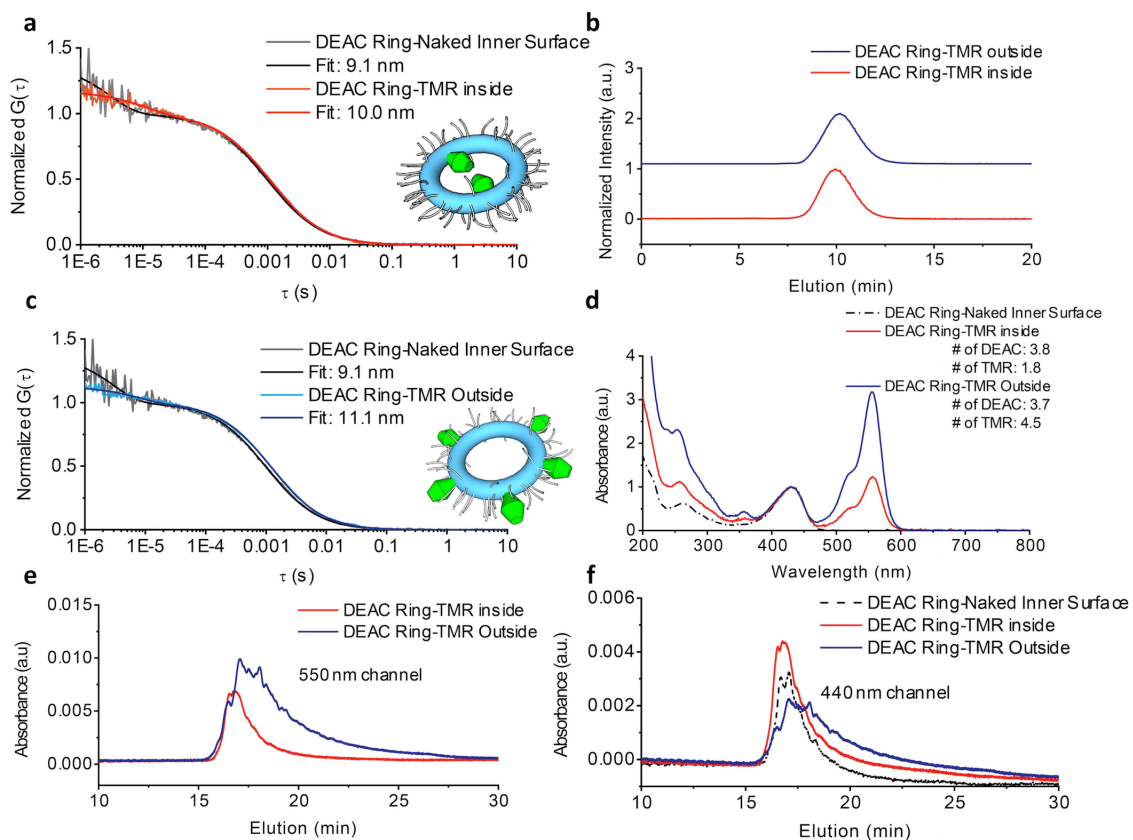


**Figure 2.4:** Comparison between DEAC-rings with TMR functionalization inside (red) and outside (blue). (a,c) FCS auto-correlation curves suggesting hydrodynamic sizes of inside (a) and outside (c) TMR functionalized DEAC-rings of 10.0 nm and 11.1 nm, respectively, both larger than the reference DEAC-rings with no extra functionality (9.1 nm, black). (b) GPC chromatograms of these two TMR functionalized ring samples. (d) Absorption spectra of inside and outside TMR functionalized DEAC-rings compared to reference DEAC-rings and normalized to DEAC absorption maximum at ~440 nm. Combination of absorption and FCS results confirm the same DEAC dye numbers for these two ring samples (3.8 and 3.7 dyes for inner and outer functionalized rings, respectively), but suggest different degrees of TMR functionalization with 1.8 and 4.5 TMR dyes for the inner and outer surface functionalized rings, respectively. (e,f) HPLC chromatograms of inside and outside TMR functionalized DEAC-rings at 550 nm read out channel (e, TMR dye absorption), and at 440 nm read out channel (f, DEAC dye absorption). In (f) results are plotted against the reference DEAC-rings with no TMR functionality (black curve).

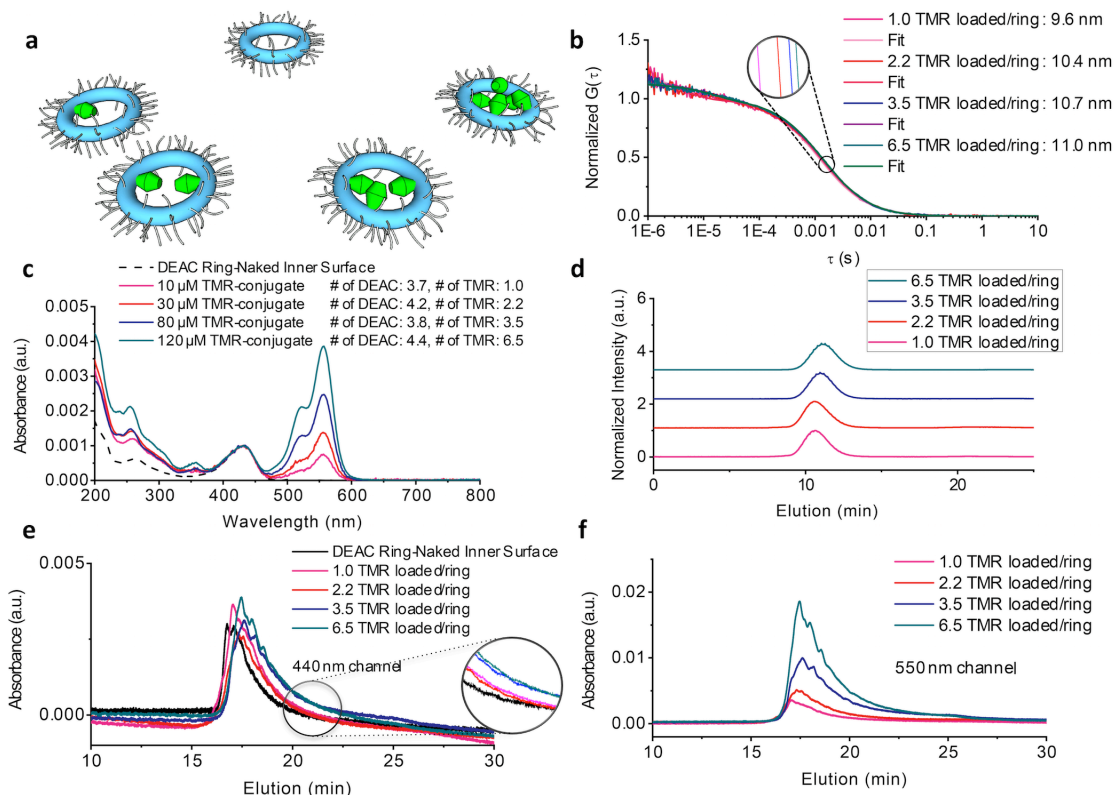


**Figure 2.5:** Comparison of DEAC rings with increasing inner surface functionalization with TMR dye. (a) Illustration of TMR loading to the inside surfaces of DEAC-rings, where as a function of TMR concentration in the synthesis, TMR dyes (shown in green) progressively get exposed to the ring outside as the number of TMR dyes per DEAC-ring increases. (b) FCS auto-correlation curves of ring samples obtained from TMR-dye concentrations in the synthesis of 10  $\mu$ M, 30  $\mu$ M, 80  $\mu$ M, and 120  $\mu$ M resulting in hydrodynamic sizes of 9.6 nm, 10.4 nm, 10.7 nm, and 11.0 nm, respectively. (c) Absorption spectra of the same four samples as in (b) normalized to the 440 nm DEAC dye absorption. Together with FCS results from (b) these data suggest 3.7, 4.2, 3.8, and 4.4 DEAC dyes encapsulated in the silica ring matrix, and 1.0, 2.2, 3.5, and 6.5 TMR dyes on the (inner) silica ring surface for each of the four batches, respectively. (d) GPC chromatograms of these four TMR functionalized ring samples. (e,f) HPLC chromatograms of the same four TMR functionalized DEAC-ring batches as in (b,c,d) measured at the 440 nm read out channel (e, DEAC dye absorption) and the 550 nm read out channel (f, TMR dye absorption). In (e) HPLC data of the four ring batches are compared to results of the parent (non-TMR functionalized, naked) rings (black curve).

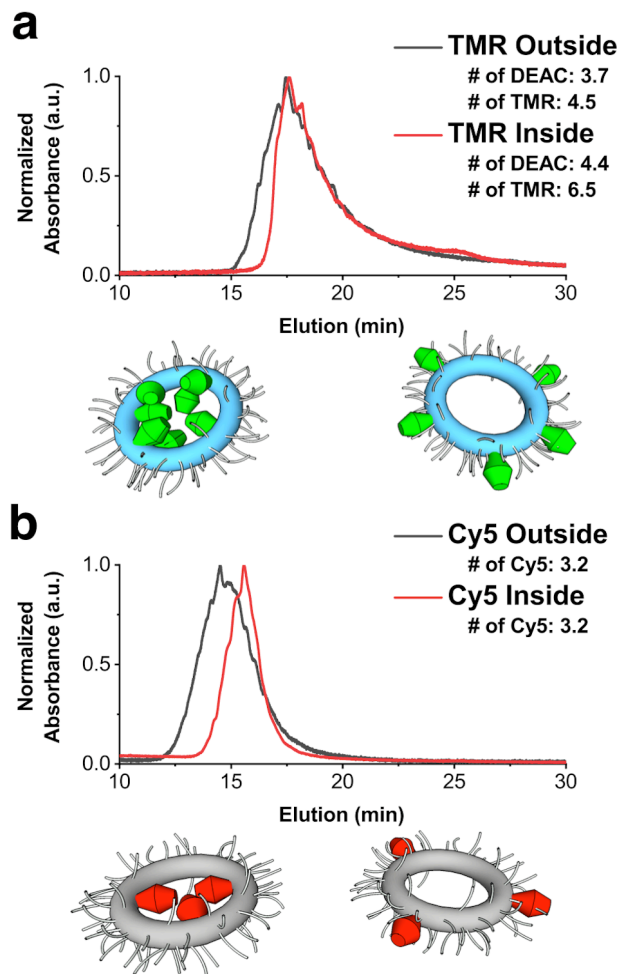


**Figure 2.6:** HPLC chromatograms at (a) 550 nm (TMR dye absorption), and (b) 647 nm (Cy5 dye absorption) read out channels for inside/outside TMR dye loaded DEAC rings, and inside/outside Cy5 dye loaded blank silica rings, respectively.

## REFERENCES

1. Jadzinsky, P. D.; Calero, G.; Ackerson, C. J.; Bushnell, D. A.; Kornberg, R. D., Structure of a Thiol Monolayer-Protected Gold Nanoparticle at 1.1 Å Resolution. *Science* **2007**, *318*, 430-433.
2. Turner, M.; Golovko, V. B.; Vaughan, O. P.; Abdulkin, P.; Berenguer-Murcia, A.; Tikhov, M. S.; Johnson, B. F.; Lambert, R. M., Selective Oxidation with Dioxygen by Gold Nanoparticle Catalysts Derived from 55-Atom Clusters. *Nature* **2008**, *454* (7207), 981-983.
3. Phillips, E.; Penate-Medina, O.; Zanzonico, P. B.; Carvajal, R. D.; Mohan, P.; Ye, Y.; Humm, J.; Gonen, M.; Kalaigian, H.; Schoder, H.; Strauss, H. W.; Larson, S. M.; Wiesner, U.; Bradbury, M. S., Clinical Translation of an Ultrasmall Inorganic Optical-PET Imaging Nanoparticle Probe. *Sci Transl Med* **2014**, *6* (260), 1-9.
4. Park, J. H.; von Maltzahn, G.; Zhang, L.; Schwartz, M. P.; Ruoslahti, E.; Bhatia, S. N.; Sailor, M. J., Magnetic Iron Oxide Nanoworms for Tumor Targeting and Imaging. *Adv Mater* **2008**, *20* (9), 1630-1635.
5. Jana, N. R.; Gearheart, L.; Murphy, C. J., Wet Chemical Synthesis of High Aspect Ratio Cylindrical Gold Nanorods. *J Phys Chem B* **2001**, *105* (19), 4065-4067.
6. Ma, K.; Gong, Y.; Aubert, T.; Turker, M. Z.; Kao, T.; Doerschuk, P. C.; Wiesner, U., Self-Assembly of Highly Symmetrical, Ultrasmall Inorganic Cages Directed by Surfactant Micelles. *Nature* **2018**, *558* (7711), 577-580.
7. Tessonier, J. P.; Ersen, O.; Weinberg, G.; Pham-Huu, C.; Su, D. S.; Schlogl, R., Selective Deposition of Metal Nanoparticles Inside or Outside Multiwalled Carbon Nanotubes. *Acs Nano* **2009**, *3* (8), 2081-2089.
8. Zhao, Z.; Jacovetty, E. L.; Liu, Y.; Yan, H., Encapsulation of Gold Nanoparticles in a DNA Origami Cage. *Angew Chem Int Ed Engl* **2011**, *50* (9), 2041-2044.
9. Ma, K.; Spoth, K. A.; Cong, Y.; Zhang, D.; Aubert, T.; Turker, M. Z.; Kourkoutis, L. F.; Mendes, E.; Wiesner, U., Early Formation Pathways of Surfactant Micelle Directed Ultrasmall Silica Ring and Cage Structures. *J Am Chem Soc* **2018**, *140* (50), 17343-17348.
10. Tang, F.; Li, L.; Chen, D., Mesoporous Silica Nanoparticles: Synthesis, Biocompatibility and Drug Delivery. *Adv Mater* **2012**, *24* (12), 1504-1534.

11. Lee, J. E.; Lee, N.; Kim, T.; Kim, J.; Hyeon, T., Multifunctional Mesoporous Silica Nanocomposite Nanoparticles for Theranostic Applications. *Acc Chem Res* **2011**, *44* (10), 893-902.
12. Chen, A. M.; Zhang, M.; Wei, D.; Stueber, D.; Taratula, O.; Minko, T.; He, H., Co-Delivery of Doxorubicin and Bcl-2 siRNA by Mesoporous Silica Nanoparticles Enhances the Efficacy of Chemotherapy in Multidrug-Resistant Cancer Cells. *Small* **2009**, *5* (23), 2673-2677.
13. Choi, H. S.; Liu, W.; Misra, P.; Tanaka, E.; Zimmer, J. P.; Ity Ipe, B.; Bawendi, M. G.; Frangioni, J. V., Renal Clearance of Quantum Dots. *Nat Biotechnol* **2007**, *25* (10), 1165-1170.
14. Burns, A. A.; Vider, J.; Ow, H.; Herz, E.; Penate-Medina, O.; Baumgart, M.; Larson, S. M.; Wiesner, U.; Bradbury, M., Fluorescent Silica Nanoparticles with Efficient Urinary Excretion for Nanomedicine. *Nano Lett* **2009**, *9* (1), 442-448.
15. Ma, K.; Sai, H.; Wiesner, U., Ultrasmall Sub-10 nm Near-Infrared Fluorescent Mesoporous Silica Nanoparticles. *J Am Chem Soc* **2012**, *134* (32), 13180-13183.
16. Ma, K.; Werner-Zwanziger, U.; Zwanziger, J.; Wiesner, U., Controlling Growth of Ultrasmall Sub-10 nm Fluorescent Mesoporous Silica Nanoparticles. *Chemistry of Materials* **2013**, *25* (5), 677-691.
17. Chen, F.; Ma, K.; Madajewski, B.; Zhuang, L.; Zhang, L.; Rickert, K.; Marelli, M.; Yoo, B.; Turker, M. Z.; Overholtzer, M.; Quinn, T. P.; Gonen, M.; Zanzonico, P.; Tuesca, A.; Bowen, M. A.; Norton, L.; Subramony, J. A.; Wiesner, U.; Bradbury, M. S., Ultrasmall Targeted Nanoparticles with Engineered Antibody Fragments for Imaging Detection of HER2-Overexpressing Breast Cancer. *Nat Commun* **2018**, *9* (1), 1-11
18. Chen, F.; Ma, K.; Zhang, L.; Madajewski, B.; Zanzonico, P.; Sequeira, S.; Gonen, M.; Wiesner, U.; Bradbury, M. S., Target-or-Clear Zirconium-89 Labeled Silica Nanoparticles for Enhanced Cancer-Directed Uptake in Melanoma: A Comparison of Radiolabeling Strategies. *Chem Mater* **2017**, *29* (19), 8269-8281.
19. Shin, J.; Anisur, R. M.; Ko, M. K.; Im, G. H.; Lee, J. H.; Lee, I. S., Hollow Manganese Oxide Nanoparticles as Multifunctional Agents for Magnetic Resonance Imaging and Drug Delivery. *Angew Chem Int Ed Engl* **2009**, *48* (2), 321-324.
20. Santra, S.; Kaittanis, C.; Grimm, J.; Perez, J. M., Drug/Dye-Loaded, Multifunctional Iron Oxide Nanoparticles for Combined Targeted Cancer

- Therapy and Dual Optical/Magnetic Resonance Imaging. *Small* **2009**, *5* (16), 1862-1868.
21. Ma, K.; Wiesner, U., Modular and Orthogonal Post-PEGylation Surface Modifications by Insertion Enabling Penta-Functional Ultrasmall Organic-Silica Hybrid Nanoparticles. *Chemistry of Materials* **2017**, *29* (16), 6840-6855.
  22. Jones, M. R.; Macfarlane, R. J.; Lee, B.; Zhang, J.; Young, K. L.; Senesi, A. J.; Mirkin, C. A., DNA-Nanoparticle Superlattices Formed from Anisotropic Building Blocks. *Nat Mater* **2010**, *9* (11), 913-917.
  23. Vivero-Escoto, J. L.; Slowing, II; Trewyn, B. G.; Lin, V. S., Mesoporous Silica Nanoparticles for Intracellular Controlled Drug Delivery. *Small* **2010**, *6* (18), 1952-1967.
  24. Cho, E. J.; Holback, H.; Liu, K. C.; Abouelmagd, S. A.; Park, J.; Yeo, Y., Nanoparticle Characterization: State of the Art, Challenges, and Emerging Technologies. *Mol Pharm* **2013**, *10* (6), 2093-2110.
  25. Mullen, D. G.; Desai, A. M.; Waddell, J. N.; Cheng, X. M.; Kelly, C. V.; McNerny, D. Q.; Majoros, I. J.; Baker, J. R., Jr.; Sander, L. M.; Orr, B. G.; Banaszak Holl, M. M., The Implications of Stochastic Synthesis for the Conjugation of Functional Groups to Nanoparticles. *Bioconjug Chem* **2008**, *19* (9), 1748-1752.
  26. Mullen, D. G.; Fang, M.; Desai, A.; Baker, J. R.; Orr, B. G.; Banaszak Holl, M. M., A Quantitative Assessment of Nanoparticle-Ligand Distributions: Implications for Targeted Drug and Imaging Delivery in Dendrimer Conjugates. *ACS Nano* **2010**, *4* (2), 657-670.
  27. Gardinier, T. C.; Kohle, F. F. E.; Peerless, J. S.; Ma, K.; Turker, M. Z.; Hinckley, J. A.; Yingling, Y. G.; Wiesner, U., High-Performance Chromatographic Characterization of Surface Chemical Heterogeneities of Fluorescent Organic-Inorganic Hybrid Core-Shell Silica Nanoparticles. *ACS Nano* **2019**, *13* (2), 1795-1804.
  28. Masters, C. L.; Simm, G.; Weinman, N. A.; Multhaup, G.; McDonald, B. L.; Beyreuther, K., Amyloid Plaque Core Protein in Alzheimer Disease and Down Syndrome. *Proceedings of the National Academy of Science USA* **1985**, *82*, 4245-4249.
  29. Lee, M. S.; Kerns, E. H., LC/MS Applications in Drug Development. *Mass Spectrom Rev* **1999**, *18* (3-4), 187-279.
  30. Peng, J.; Elias, J. E.; Thoreen, C. C.; Licklider, L. J.; Gygi, S. P., Evaluation of Multidimensional Chromatography Coupled with Tandem Mass

Spectrometry (LC/LC-MS/MS) for Large-Scale Protein Analysis: The Yeast Proteome. *Journal of Proteome Research* **2002**, 2 (1), 43-50.

31. Ma, K.; Zhang, D.; Cong, Y.; Wiesner, U., Elucidating the Mechanism of Silica Nanoparticle PEGylation Processes Using Fluorescence Correlation Spectroscopies. *Chemistry of Materials* **2016**, 28 (5), 1537-1545.
32. Larson, D. R.; Ow, H.; Vishwasrao, H. D.; Heikal, A. A.; Wiesner, U.; Webb, W. W., Silica Nanoparticle Architecture Determines Radiative Properties of Encapsulated Fluorophores. *Chemistry of Materials* **2008**, 20 (8), 2677-2684.
33. Kohle, F. F. E.; Hinckley, J. A.; Li, S.; Dhawan, N.; Katt, W. P.; Erstling, J. A.; Werner-Zwanziger, U.; Zwanziger, J.; Cerione, R. A.; Wiesner, U. B., Amorphous Quantum Nanomaterials. *Adv Mater* **2018**, 1806993-1-1806993-9.
34. Turker, M. Z.; Ma, K.; Wiesner, U. B., Bimodal Morphology Transition Pathway in the Synthesis of Ultrasmall Fluorescent Mesoporous Silica Nanoparticles. *The Journal of Physical Chemistry C* **2019**, 123, 9582-9589.
35. Ma, K.; Mendoza, C.; Hanson, M.; Werner-Zwanziger, U.; Zwanziger, J.; Wiesner, U., Control of Ultrasmall Sub-10 nm Ligand-Functionalized Fluorescent Core-Shell Silica Nanoparticle Growth in Water. *Chemistry of Materials* **2015**, 27 (11), 4119-4133.
36. Berlepsch, H. V.; Bottcher, C., H-Aggregates of an Indocyanine Cy5 Dye: Transition from Strong to Weak Molecular Coupling. *J Phys Chem B* **2015**, 119 (35), 11900-11909.

CHAPTER 3

CONTROLLING SURFACE CHEMICAL HETEROGENEITIES OF  
ULTRASMALL FLUORESCENT CORE-SHELL SILICA NANOPARTICLES AS  
REVEALED BY HIGH PERFORMANCE LIQUID CHROMATOGRAPHY

*Abstract*

Ultrasmall (diameter below 10 nm) fluorescent core-shell silica nanoparticles have garnered increasing attention in recent years as a result of their high brightness and favorable biodistribution properties important for applications including bioimaging and nanomedicine. Here we present an in-depth study that provides new insights into the physical parameters that govern full covalent fluorescent dye encapsulation within the silica core of poly(ethylene glycol) coated core-shell silica nanoparticles referred to as Cornell Prime Dots (C' dots). We use a combination of high-performance liquid chromatography (HPLC), gel permeation chromatography (GPC), and fluorescence correlation spectroscopy (FCS) to monitor the result of ammonia concentration in the synthesis of C' dots from negatively and positively charged versions of near infrared dyes Cy5 and Cy5.5. HPLC in particular allows the distinction between cases of full versus partial dye encapsulation in the silica particle core leading to surface chemical heterogeneities in the form of hydrophobic surface patches, which in turn modulate biological response in ferroptotic cell death experiments. Our results demonstrate that there is a complex interplay between dye-dye and dye-silica cluster interactions originally formed in the sol-gel synthesis

governing optimal dye encapsulation. We expect that the reduced surface chemical heterogeneities will make the resulting nanoparticles attractive for a number of applications in biology and medicine.

### ***Introduction***

Nanoparticle synthesis is ubiquitous in a host of research fields from energy to healthcare and provides access to a diverse array of materials such as quantum dots or polymer, metal, and oxide nanoparticles.<sup>1-4</sup> Key characteristics of successful nanoparticle preparation methods are the batch-to-batch reproducibility and control over properties such as size, brightness, and surface chemistry.<sup>5-8</sup> In the last five to ten years, increasing interest has focused on the synthesis of ultrasmall (diameter <10 nm) nanoparticles. In addition to unique properties emerging at this scale, their small size enables use of high performance liquid chromatography (HPLC) to quantitatively analyze particle surface chemical properties.<sup>9,10</sup> While HPLC is ubiquitous in fields with precisely defined molecular materials such as small molecules, macromolecular structures like dendrimers, and proteins,<sup>11-15</sup> the successful application of HPLC to inorganic core - organic shell (core-shell) nanoparticles is a recent development.<sup>9,10,16</sup> As a result of the well-established versatility of HPLC for synthesis product quality control, this adds a novel and intriguing dimension to the analysis of nanoparticles, e.g. in order to further tune their surface chemical properties for biological applications.<sup>9</sup> Within a single synthesis batch, HPLC allows mapping of variations in the surface chemistry of nanoparticles onto different peaks in the chromatograms.

Such quantitative assessments of the degree of heterogeneity in particle surface chemical properties are in stark contrast to the averaged particle surface properties as typically revealed, *e.g.* via zeta potential or spectroscopic measurements. Furthermore, in combination with other analytical techniques such as gel-permeation chromatography (GPC), HPLC enables multidimensional correlation analyses. In the case of coupled GPC-HPLC runs, *e.g.* this allows to map surface chemical heterogeneities onto particle size dispersity.<sup>9</sup> This in turn opens the door to answering questions of how particle batch heterogeneities modulate biological response, hitherto a largely unexplored area because of the lack of appropriate quantitative characterization techniques.

A system of particular interest for in-depth study with this type of analytical technique are Cornell prime dots (C' dots), a class of ultrasmall (diameter <10 nm) fluorescent core-shell silica nanoparticles currently in multiple clinical trials to test for both diagnostic and therapeutic clinical potential [for targeted PET and/or optical detection of metastatic melanoma (NCT01266096, NCT03465618) and malignant brain tumors (NCT02106598)].<sup>17,18</sup> C' dots are composed of a fluorescent dye covalently encapsulated within a silica core grown via sol-gel chemistry and covalently coated with a brush like poly(ethylene glycol)-(PEG-)silane shell.<sup>19,20</sup> The encapsulated fluorescent dye can be varied based on application, but typically dyes such as Cy5 and Cy5.5 are used for their near infrared (NIR) absorption and emission profiles advantageous for biological applications.<sup>17,18,21</sup> The underlying chemical structure of these dyes is extremely hydrophobic. Therefore, often sulfonate groups are

introduced in the dye periphery in order to increase their hydrophilicity and facilitate their use in aqueous media.<sup>19,22,23</sup>

In early iterations of the water-based C' dot synthesis, typically sulfonated analogues of Cy5 and Cy5.5 dyes were conjugated to a silane moiety via a maleimide-thiol coupling reaction.<sup>19</sup> The resulting dye-silane conjugates were then covalently encapsulated into the silica matrix via the sol-gel process and subsequently PEGylated, providing enhanced photophysical properties along with significantly increased hydrophilicity of the resulting core-shell dots relative to the free dye in water.<sup>19,23</sup> Recent work employing HPLC to elucidate the surface chemistry of such C' dots revealed, however, that use of negatively charged sulfonated Cy5 was the cause of significant surface chemical heterogeneity.<sup>9</sup> HPLC chromatograms of such particles exhibited multiple peaks (see Figure 3.2a below). The first peak at the shortest elution time corresponded to C' dots with the desired purely PEGylated nanoparticle surface with Cy5 dye either fully encapsulated or completely absent. Subsequent peaks could be assigned to one, two, or three Cy5 dyes on the silica nanoparticle surface, respectively, leading to hydrophobic patches between the PEG chains, which in turn were responsible for the observed shifts to longer elution times in the HPLC chromatograms. These results were corroborated using additional techniques such as after-pulse corrected fluorescence correlation spectroscopy (FCS), single particle photo-bleaching, and molecular dynamics simulations.<sup>9</sup> Dye charge was found to play a key role in the successful encapsulation of a specific dye into the silica matrix, rather than its covalent attachment onto the silica nanoparticle core surface.<sup>9</sup>

Dyes exposed on the particle surface have a greater propensity for chemical degradation or potential hydrolysis and may therefore have significant effects on the behavior of these types of nanoparticles in complex biological environments such as the human body. Having identified a method to quantitatively assess these surface chemical heterogeneities as well as their main driver, *i.e.* dye charge, now allows us to perform systematic studies in order to provide insights into the factors in the interactions between ~2 nm sized silica clusters originally formed in the sol-gel silica synthesis and the fluorescent dyes that govern optimal dye encapsulation. To that end here we work with negatively and positively charged variants of the NIR dyes Cy5 and Cy5.5 relevant for applications in nanomedicine. Combining HPLC with gel permeation chromatography (GPC) and FCS, we elucidate synthesis conditions under which full dye encapsulation into the silica core is achieved for both dyes, leading to minimal heterogeneity in particle surface chemical properties obtained from individual synthesis batches. In particular, we show that for different dyes successful encapsulation requires careful tuning of the starting concentration of ammonium hydroxide in aqueous solution. This directly effects the rate of hydrolysis and condensation of the silica precursors, and the surface charge of the resulting silica clusters formed initially in the sol-gel process, which in turn governs the electrostatics of both cluster-dye and cluster-cluster interactions critical for successful particle formation. Finally, we demonstrate how particle heterogeneities based on different degrees of dye encapsulation modulate biological response, using recently discovered C dot induced ferroptosis, an iron dependent cell death program, as a test bed.<sup>24</sup>

## ***Methods***

### ***Chemicals and Reagents***

UHPLC grade acetonitrile was purchased from BDH. Superdex 200 resin was purchased from GE Healthcare Life Sciences. Vivaspin 30k MWCO spin filters were purchased from GE Healthcare Life Sciences. 5 M NaCl in water solution was purchased from Santa Cruz Biotechnology. Dimethyl sulfoxide (DMSO), tetramethyl orthosilicate (TMOS), (3-mercaptopropyl)trimethoxysilane (MPTMS), Iron(III) nitrate, and 2.0 M ammonia in ethanol were all purchased from Sigma-Aldrich. Methoxy-PEG(6-9)-silane (~500 g/mol) was purchased from Gelest. Sulfo-Cy5-maleimide and sulfo-Cy5.5-maleimide were purchased from GE. Cy5-maleimide and Cy5.5-maleimide were purchased from Lumiprobe. DI water was generated using a Millipore IQ7000 system (18.2 M $\Omega$ -cm). Xbridge Protein BEH C4 Column (300 Å, 3.5  $\mu$ m, 4.6 mm X 150 mm, 10K-500K) was purchased from Waters Technologies Corporation. MDA-MB-468 cells were obtained from the ATCC, and were used within 3 months of thawing. RPMI-1640, fetal bovine serum (FBS), and dialyzed FBS were from Gibco. Amino-acid-free RPMI-1640 was from United States Biological. GlutaMax, Pen/Strep, and PrestoBlue reagent were from Invitrogen. All chemicals were used as received without further purification.

### ***Particle Synthesis and Purification***

C' dots were synthesized as previously described<sup>19</sup>. Briefly, for a 10 mL batch, 0.367  $\mu\text{mol}$  mono functional maleimido derivatized dye was dissolved in DMSO overnight in a glovebox. A 23-fold excess of mercaptopropyl-trimethoxysilane (MPTMS) was added to the dissolved dye and allowed to react overnight in the glove box. The next day a flask containing deionized water pH adjusted using between 0.5 mL and 2.5 mL of 0.02M ammonium hydroxide (ammonium hydroxide was prepared by mixing 100  $\mu\text{L}$  of 2.0 M ammonia in ethanol solution into 10 mL of deionized water) was prepared and stirred vigorously. For sulfonated dyed C' dot syntheses, 1 mL of 0.02 M ammonium hydroxide was added into 9 mL deionized water. 68  $\mu\text{L}$  tetramethylorthosilicate (TMOS) and the prepared dye-silane conjugate were added to the flask drop-wise and allowed to react overnight. The following day, 100  $\mu\text{L}$  of mPEG(6-9)-silane was added to the flask drop-wise and allowed to react overnight. The following day stirring of the solution was stopped and the flask heated to 80°C for 24 hours. Following this heating step, the particles were extensively dialyzed using 10K MWCO cellulose dialysis tubing, followed by syringe filtration with a 200 nm membrane, spin filtering with a 30K MWCO PES membrane spin filter, and finally GPC purification through Superdex 200 resin on a Bio-Rad FPLC. The particles were then characterized using fluorescence correlation spectroscopy (FCS) on a home-built setup and UV/Vis spectroscopy on a Cary 5000 spectrometer.

### ***High Performance Liquid Chromatography (HPLC)***

All injections were performed at a standardized injection volume of 8  $\mu\text{L}$  and concentration of 30  $\mu\text{M}$ . Concentrations for injected samples were determined prior to analysis by FCS. The columns used were 150 mm Waters Xbridge BEH C4 Protein separation columns with 300  $\text{\AA}$  pore size and 3.5  $\mu\text{m}$  particle size. The separation method used was as follows: The sample was first injected onto the column in a flow of 90:10 water:acetonitrile at a flow rate of 0.75 mL/min, and this isocratic segment of the method was maintained for 20 minutes. The mobile phase composition was then changed to 45:55 water:acetonitrile in a step-like fashion and the baseline was allowed to equilibrate for 5 minutes. Finally, a composition gradient of 45:55 to 5:95 water:acetonitrile was run over the course of 20 minutes. During this time the analyte eluted from the column.

### ***Gel Permeation Chromatography (GPC)***

Preparative scale gel permeation chromatography was carried out on a Bio-Rad FPLC equipped with a UV detector set to 275 nm. Particles were purified under isocratic conditions using 0.9 wt.% NaCl in deionized water. The eluent was prepared directly before nanoparticle purification by diluting 0.2  $\mu\text{m}$  membrane filtered 5 M NaCl in water (Santa Cruz Biotechnology) with deionized water (18.2  $\text{M}\Omega$  acquired from Millipore IQ7000). The column used was a standard glass Bio-Rad column with dimensions of 20 mm x 300 mm and was hand-packed with Superdex 200. The

column was operated at 2.0 mL/min and was allowed to equilibrate with the mobile phase for at least 30 minutes before sample purification. All samples were concentrated in GE Life Sciences 30 kDa MWCO VivaSpin filters prior to injection. The total injection volume was less than 1 mL per run. Particles eluted around the 15-minute mark and the total run lasted 30 minutes.

### ***Fluorescence Correlation Spectroscopy (FCS)***

FCS measurements were carried out on a home built set up using a 635 nm solid-state laser and a continuous wave laser. This is the standard laser setup for fluorescent dyes with absorbance maxima around 650 nm. The continuous wave laser was focused onto the image plane of a water immersion microscope objective (Zeiss Plan-Neofluar 63x NA 1.2). The emitted fluorescence was Stokes-shifted and therefore after it passed back through the same objective it could successfully pass through a dichroic mirror, after which it was spatially filtered by a 50  $\mu\text{m}$  pinhole and then finally through a spectrally filtered long pass filter (ET665lp, Chroma) before being detected by an avalanche photodiode detector (SPCM-AQR-14, PerkinElmer). The signal was autocorrelated by a digital correlator (Flex03LQ, Correlator.com) with a lag time resolution of 15 ns. Autocorrelation curves were fitted with equation (3.1) that accounts for fast photophysical processes and translational diffusion.

$$G(\tau) = 1 + \frac{1}{N_{\text{nz}}} \left( \frac{1}{1 + \tau/\tau_D} \right) \left( \frac{1}{1 + \tau/(\tau_D k^2)} \right)^{1/2} \frac{1}{(1 - P)} (1 - P + P \exp(-\tau/\tau_F)) \quad (3.1)$$

Where  $N_m$  is the number of fluorescent particles diffusing through the focal volume at any given time,  $\tau_D$  is the average translational diffusion time of the fluorescent material diffusing through the focal volume,  $\tau_p$  is the characteristic relaxation time for fast photophysical processes,  $K$  is the focal volume structure factor calculated from the radial and axial radii ( $K = \omega_x/\omega_{xy}$ ), and P is the fraction of fluorescent particles undergoing a fast photophysical process during the experiment.. All autocorrelation curves were normalized according to equation (3.2):

$$G(\tau) = (G(\tau) - 1) N_m \quad (3.2)$$

### ***UV/Vis Spectroscopy***

Absorbance spectra of C' dot samples were measured in DI water on a Varian Cary 5000 spectrophotometer in a 3 mL quartz cuvette with a 10 mm light path (HellmaAnalytics) from 200 nm to 800 nm in 1 nm increments. All spectra were baseline corrected using a cuvette with DI water as reference cell. Maximum absorption at the dye absorption wavelength was kept between 0.01 and 0.06.

## ***Cell Work***

MDA-MB-468 cells were maintained at 37 degrees Celcius, 5% CO<sub>2</sub>, in complete medium (RPMI-1640 supplemented with 10% FBS). Cells were plated in 96 well plates at a concentration of 2X10<sup>4</sup> cells per well and allowed to settle overnight. The medium was then removed, and replaced with amino-acid-free RPMI-1640 supplemented with 10% dialyzed FBS, 1X GlutaMax, and 1X Pen/Strep, along with the indicated amount of iron(III) nitrate or C' dots. In experiments with C' dots, all conditions also included 1 μM iron(III) nitrate. The cells were incubated for 6 days. The medium was then replaced with complete medium, and cell viability was assessed with PrestoBlue reagent per the manufacturer's instructions. Data was read out in absorbance mode on a Tecan Safire instrument.

## ***Results and Discussion***

### ***Positively Charged Dye Chemistry Greatly Improves Particle Surface Chemical Homogeneity***

Figure 3.1 shows sulfonated Cy5 that has a net charge of -1 (top row, left). As discussed in the introduction and shown in Figure 3.2a, because of repulsive Coulomb interactions with negatively charged silica at slightly basic synthesis conditions, this net negative charge causes a significant amount of nanoparticles surface chemical heterogeneity as manifested in the occurrence of three prominent and one weak peak

in HPLC chromatograms.<sup>9</sup> As indicated in the insets of Figure 3.2a, these peaks correspond to particles with 0, 1, 2, or 3 dyes covalently attached to the silica surface (purple curve in Figure 3.2a).<sup>9</sup> By switching to the unsulfonated derivative of Cy5 (Figure 3.1, top row, right), dye charge in solution changes from -1 to +1, which as shown in Figure 3.2a (green curve) promoted full encapsulation as the result of what are now attractive dye-silica interactions. As the HPLC chromatogram shows, the positively dye encapsulating particles all eluted at the same time giving rise to a single peak reflecting high particle surface homogeneity.<sup>9</sup>

While the surface chemical heterogeneity of C' dots caused by encapsulation of a dye with net -1 charge has been investigated *via* HPLC and is now understood,<sup>9</sup> the effects on particle surface heterogeneity of dyes with even higher net negative charge is still an outstanding question. This is particularly relevant for near infrared (NIR) dyes such as Cy5.5 (abs./em.: 675/695 nm), which are larger than Cy5 (abs./em.: 650/670 nm) in order to emit further out in the NIR and therefore are significantly more hydrophobic. The commercially available sulfonated analogue of Cy5.5 carries four sulfonate groups and has a net charge of -3 (Figure 3.1, bottom row, left) in order to provide good solubility in aqueous solutions despite the large hydrophobic molecular framework. This poses a significant challenge to the encapsulation into ultrasmall fluorescent core-shell silica nanoparticles due to strong repulsive interactions between the highly negatively charged primary silica clusters initially formed in the sol-gel synthesis of C' dots and the negatively charged dyes.<sup>25,</sup>

<sup>26</sup> The negative charge of the primary clusters in the pH range where the C' dot

synthesis is typically performed is attenuated as they aggregate and as more silicic acid is produced via hydrolysis of TMOS.<sup>27</sup> According to previous molecular dynamics simulations, it is this decrease in cluster surface charge as the synthesis proceeds which eventually allows the negatively charged dyes to condense onto the surface of the forming C' dots.<sup>9</sup> The HPLC chromatogram of C' dots synthesized with sulfo-Cy5.5 is shown in Figure 3.2b (blue curve). Compared to that of the sulfo-Cy5 derived particles (Figure 3.2c), it displays dramatically increased heterogeneity, as manifested in at least five peaks that extend to much longer elution times indicating a significantly more hydrophobic particle. It is clear from this data, that the majority of the dyes in the Cy5.5 based C' dot synthesis ended up on the particle surface.

### ***Primary Cluster Charge is a Critical Parameter to Control***

While switching from a negative dye to a positive dye analogue generally affords significant enhancement in nanoparticle homogeneity, synthesis parameters must be tuned as a function of individual dye chemistries to ensure optimal nanoparticle surface chemical properties. Switching to the positively charged, unsulfonated analogues of dyes like Cy5 and Cy5.5 allows for the dyes to act as nucleation sites for the nanoparticles formed from negatively charged primary silica clusters, which is responsible for the full encapsulation into silica as the C' dots grow. In turn, for fully optimized synthesis conditions (*vide infra*) this leads to a high degree of surface chemical homogeneity as evidenced by single peaks in HPLC chromatograms as shown in Figure 3.2a-b (green curves) for Cy5 and Cy5.5,

respectively. However, this switch of dye chemistry is not without challenges, as the positively charged NIR dyes do not have the benefit of increased water solubility of the sulfonated dye analogues, and as a result are prone to aggregation in water. In order to optimize NIR C' dot synthesis conditions we turned to a combination of gel permeation chromatography (GPC), high performance liquid chromatography (HPLC), and fluorescence correlation spectroscopy (FCS). The optimization of ultrasmall fluorescent core-shell silica nanoparticles with covalently encapsulated positive NIR dyes is more nuanced than the straightforward transfer from negatively charged dyes to positively charged dyes, but equally important in order to ensure a homogeneous PEGylated nanoparticle surface. Three main interactions must be taken into account for this process: dye-dye interactions, dye-primary cluster interactions, and cluster-cluster interactions.<sup>25</sup> Dye-dye interactions are more important with unsulfonated, positively charged dyes because the dyes are more hydrophobic and prone to aggregation.<sup>22,23</sup> The concentration of dye must be carefully controlled to not cause too much dye aggregation and precipitation, which will prevent efficient dye encapsulation, while maintaining a high enough free dye concentration to provide a sufficiently high synthesis yield.

The positively charged Cy5 and Cy5.5 dyes likely act as nucleation sites for the negatively charged ~2 nm primary silica clusters that form when the silica precursor, TMOS, is added into the aqueous reaction solution.<sup>28</sup> This promotes the growth of nanoparticles and the subsequent dye encapsulation, *vide supra*. As primary clusters aggregate around a positively charged dye, the positive charge becomes

electrostatically shielded and the growing nanoparticle becomes more repulsive towards additional cluster association as the particles reach electrostatic stabilization *via* growth. If the ammonia concentration in the synthesis solution is sufficiently high, these repulsive cluster-cluster interactions between highly negatively charged clusters may stop further cluster addition before the dye is fully encapsulated within silica primary clusters.<sup>29</sup> This would lead to overall smaller nanoparticles and larger numbers of hydrophobic dye patches on the surface.

### ***Surface Chemistry Optimization for covalent encapsulation of NIR Dye Cy5(+)***

This is exactly what is observed in C' dot synthesis experiments with positively charged Cy5 [Cy5(+)]: For increasing ammonia concentration the main nanoparticle peak in GPC moves to the right (Figure 3.3a,d,g,j) indicating smaller particles as corroborated by FCS (Figure 3.3c,f,i,l; Table 3.1); the corresponding HPLC traces (Figure 3.3b,e,h,k) show enhanced heterogeneity via additional peaks at higher elution times. To prevent the formation of nanoparticles with only partially encapsulated dyes, the surface charge of the primary silica clusters that form the core of the C' dots must be carefully controlled by modulating the concentration of ammonium hydroxide in solution. Ammonium hydroxide is a catalyst for the basic hydrolysis and condensation of silica in the C' dot synthesis.<sup>30</sup> It not only controls the rate of hydrolysis and condensation, but also the surface charge of the primary silica clusters formed at the beginning of the sol-gel synthesis.<sup>29</sup> Meanwhile, if the ammonium hydroxide concentration is too low, the primary silica clusters will be

significantly more prone to aggregation. While these nanoparticles will totally encapsulate the dye, the size increases significantly due to uncontrolled aggregation of primary silica clusters. This leads to the primary nanoparticle peak and the nanoparticle aggregate peak in GPC becoming inseparable as shown in Figure 3.3j. As previously demonstrated, even with extremely careful purification *via* GPC fractionation, the nanoparticle peak will always contain some aggregates that cannot be separated out.<sup>31, 32</sup> As demonstrated in Figure 3.3g-i, when working with positive Cy5-silane, the optimal starting primary cluster surface charge was reached for 10 mL batches (see Methods section) at a concentration of 1.0 mL (of 0.02 ammonia solution). Higher starting ammonia concentrations caused the dye to not be fully encapsulated, while lower ammonia concentration caused the clusters to aggregate too much due to very low surface charge. Figure 3.4 illustrates this principle of balancing primary silica cluster charge and dye charge and resulting encapsulation effects.

### ***Surface Chemistry Optimization for covalent encapsulation of NIR Dye Cy5.5(+)***

Next, this principle was applied to optimize the synthesis of NIR C' dots from positively charged Cy5.5 [Cy5.5(+)], a second clinically relevant variant of the C' dots. Evaluation of Cy5.5 C' dot syntheses along the lines of what was discussed for Cy5(+) based C' dots revealed that as a result of the different dye chemistry, the optimal synthesis conditions for Cy5.5(+) are different. Positively charged Cy5.5 is significantly larger and more hydrophobic than Cy5(+), and as a result, adjustments had to be made to the synthetic protocol. Comparing GPC, HPLC, and FCS results for

different ammonia concentrations in the synthesis (Figure 3.5), for a 10 mL batch the optimal ammonia concentration for Cy5.5 C' dots now was around 0.75 mL (of 0.02 M ammonia solution) rather than around 1 mL for Cy5(+), see Figure 3.5g-i.

The optimization of Cy5.5 C' dots highlights that for a given dye in order to obtain full dye encapsulation there is an optimal surface charge for the primary silica clusters. Simply decreasing the ammonia concentration at the beginning of the reaction is not a straightforward solution. As the pH at the beginning of the synthesis decreases as a result of TMOS hydrolysis and silicic acid formation (*vide supra*), the solubility of positively charged dyes increases, which leads to a higher propensity for dyes to condense onto the surface of the growing nanoparticles. As demonstrated with the help of GPC, HPLC, and FCS results in Figure 3.5j-l, when using 0.5 mL of ammonia solution in the reaction, the particle size further increases relative to the results for 1 mL. But this time the surface heterogeneity of the particles increases too (see Figure 3.5k). In contrast, Cy5(+)-C' dots had homogeneous surface chemistry even below the optimal ammonium hydroxide concentration (compare Figure 3.3k with 3.5k).

#### ***GPC-HPLC Elucidates Additional Heterogeneity for Low Deprotonation Conditions***

The case of Cy5.5(+) highlighted the importance of correctly optimizing the ammonium hydroxide concentration of the synthesis solution for each individual dye. In order to further understand the origin of the heterogeneity that occurred in the

regime of low primary silica cluster surface charge, we GPC-fractionated the sample of PEG-Cy5.5(+)-C' dots that showed reoccurring surface heterogeneity at 0.5 mL of 0.02 M ammonium hydroxide in the synthesis (Figure 3.6a-b), which is below the optimal ammonia concentration for Cy5.5(+) dye (0.75 mL). Three GPC fractions were then analyzed with HPLC (Figure 3.6c-e) showing surface heterogeneity is increased for earlier time fractions that reflect larger particle size, suggesting extra Cy5.5 dye condensing on the nanoparticle surface, and creating extra hydrophobic patches before the nanoparticle PEGylation step. Interestingly, the GPC trace reflecting the particle size distribution could still be well fitted with a single Gaussian function (Figure 3.6b), whereas this was not the case for Cy5(+) synthesis where the GPC peak was skewed below 1 mL ammonium hydroxide condition (compare quality of fits in Figure 3.3j and 3.5j). This suggests that at 0.5 mL ammonia synthesis conditions, after dye-mediated initial dye-cluster conjugate formation the particle growth mechanism of Cy5(+)-C' dots is primarily based on the continued addition of primary silica clusters to the growing nanoparticles, whereas in the Cy5.5(+)-dot synthesis continued addition of primary silica clusters is accompanied by extra dye condensation onto the nanoparticle surface. These results together demonstrate that simultaneous control of dye-dye and dye-silica interactions during C' dot synthesis is highly non-trivial, and synthesis conditions must be carefully tuned for any new dye candidate to achieve optimal fluorescent core-shell silica nanoparticle formation with minimal surface chemical heterogeneity.

## ***Different Degrees of Surface Chemical Heterogeneity Modulate Biological Response***

We finally were interested in determining whether nanoparticle heterogeneity in the form of hydrophobic surface patches from non-encapsulated NIR dyes had any effect on biological response. To that end we chose as a test bed the recently discovered C' dot induced iron-mediated cell death program ferroptosis observed under nutrient deprivation conditions of cancer cell populations, in which the core-shell silica nanoparticles, as a result of micropores of the silica core, chelate iron from solution and carry it into the cancer cells.<sup>24</sup> We began by assessing the sensitivity of MDA-MB-468 triple-negative breast cancer cells to treatment with iron(III) nitrate under amino-acid (AA) starved conditions. As shown in Figure 3.7a, the cells were insensitive to 1  $\mu$ M iron, but in contrast to full medium controls near-total cell death was elicited by 6  $\mu$ M iron. To determine the degree to which C' dots could modulate this biological response, we treated the cells with assorted concentrations of C' dots, while in the presence of a non-toxic amount of iron (1  $\mu$ M). As demonstrated in Figure 3.7b, the particles prepared with positively charged Cy5 dye were able to elicit a cell death response much greater than 1  $\mu$ M iron alone, in particular around and above 10  $\mu$ M particle concentrations, while particles prepared with negatively charged sulfo-Cy5 dye were able to elicit only a relatively small cell death response. Thus, the positively charged Cy5 dye encapsulating particles seem to be superior at introducing iron into the cancer cells and inducing ferroptotic cell death likely due to the decreased

hydrophobic surface patchiness of these particles and associated facilitated access to the micropores of the silica core.

### ***Conclusion***

In this study we have elucidated critical control parameters in the synthesis of fluorescent dye-encapsulating core-shell silica nanoparticles that determine surface chemical particle heterogeneities. The work highlights that depending on the dye used, small variations in synthetic conditions, here the concentration of ammonia as a catalyst in the sol-gel reaction, can lead to significant changes in surface chemical properties in the form of hydrophobic surface patches resulting from dyes conjugated to the silica core surface rather than being fully encapsulated. The complex interplay of dye-dye and dye-silica cluster interactions is critical to understand in order to effectively control the surface chemistry of the final nanoparticles. Variations in particle surface chemical properties/heterogeneities in turn modulate biological response to the nanoparticles, as demonstrated by ferroptotic cell death experiments with C' dots derived from either negatively and positively charged Cy5 dye. We therefore expect that these synthetic insights into the nucleation and growth of fluorescent core-shell silica nanoparticles prepared in aqueous solutions will have implications for application of such nanoparticles in bioimaging and nanomedicine.

## *Acknowledgements*

This work was funded by the National Cancer Institute of the National Institutes of Health (NIH) under Award Number U54CA199081. Richard Cerione thanks the Institute of General Medicine Award Number GM122575 for funding. Melik Turker thanks the Ministry of National Education of the Republic of Turkey for his student scholarship support. Melik Turker, Tom Gardinier, Joshua Hinckley, and Ulrich Wiesner designed experiments. Melik Turker synthesized fluorescent silica nanoparticles. Melik Turker and Joshua Hinckley performed FCS measurements. Thomas Gardinier developed methods and performed HPLC experiments. Thomas Gardinier, Melik Turker, and Joshua Hinckley performed GPC experiments. William Katt conducted cell experiments. Naedum DomNwachukwu, Fem Woodruff, Jessica Hersh, and Jonathan Wang helped with experiments. Thomas Gardinier, Melik Turker, Richard Cerione, and Ulrich Wiesner interpreted results and wrote the paper with input of all authors.

*Figures*

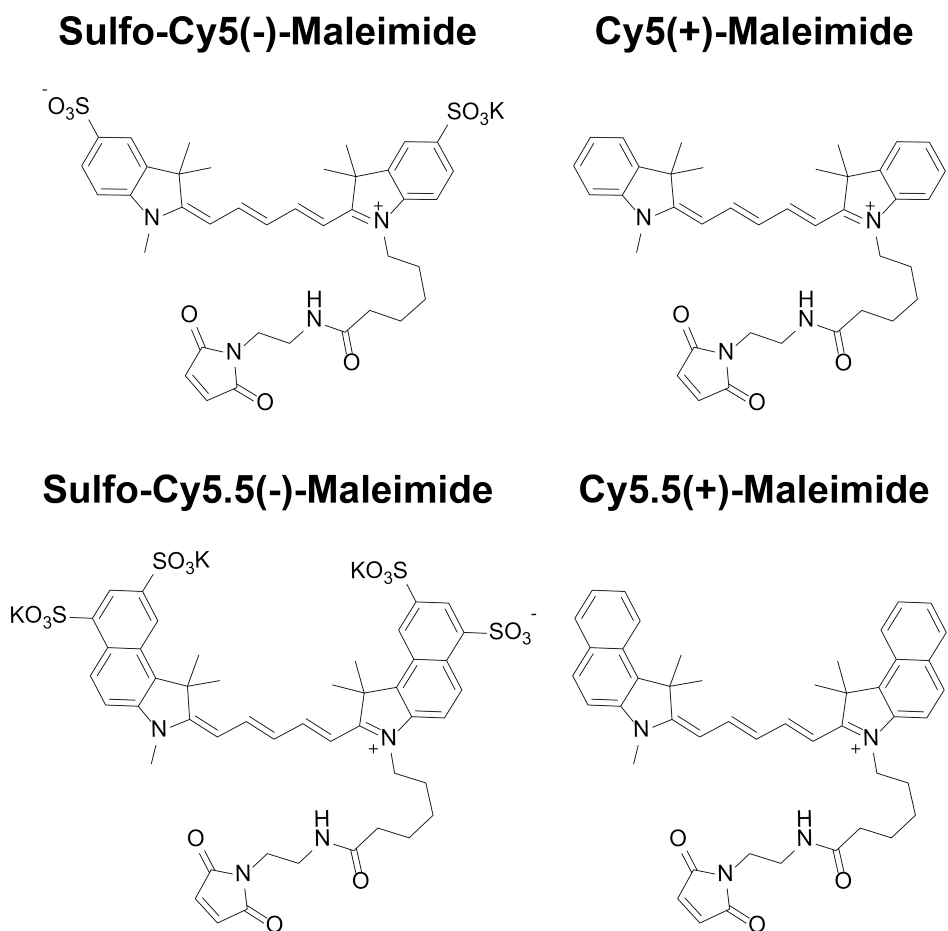


**Figure 3.1:** Structures of sulfonated and unsulfonate Cy5 and Cy5.5 maleimide derivatives. The sulfonated Cy5 has a net charge of -1 in aqueous solution, while the unsulfonated derivatives of both Cy5-maleimide and Cy5.5-maleimide have a net charge of +1 in aqueous solution. The sulfonated form of Cy5.5-maleimide has a net charge of -3 to counteract the significant hydrophobicity of this dye structure.

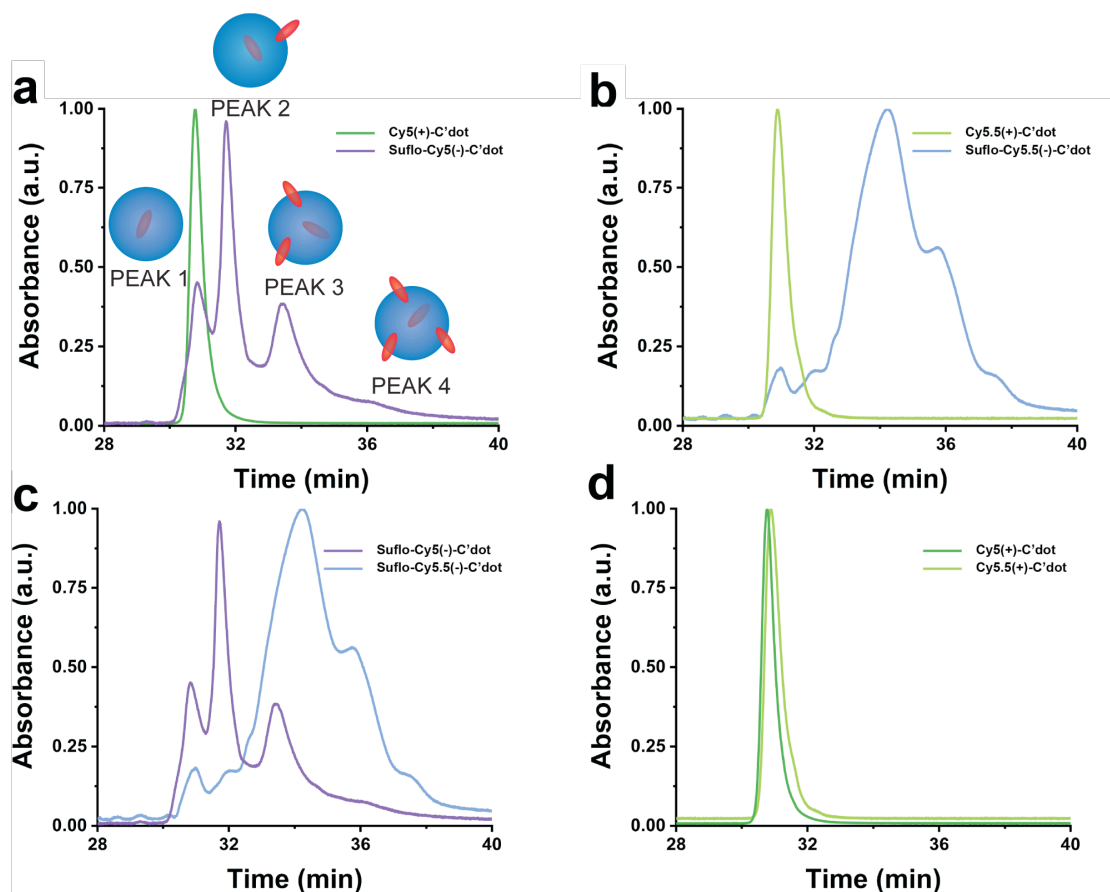


**Figure 3.2:** (a) HPLC chromatograms of PEG-sulfo-Cy5-C' dots (purple) and PEG-Cy5(+)-C' dots (dark green) with schematic representation of the type of nanoparticles that elute in each peak, and highlighting that the PEG-Cy5(+)-C' dot peak overlaps completely with the peak corresponding to purely PEGylated particles in the PEG-sulfo-Cy5-C' dot sample. (b) HPLC chromatograms of PEG-sulfo-Cy5.5-C' dots (blue) and PEG-Cy5.5(+)-C' dots (light green), again highlighting the complete overlap of the PEG-Cy5.5-C' dots with the purely PEGylated particles in the PEG-sulfo-Cy5.5-C' dot sample. (c) HPLC chromatograms of PEG-sulfo-Cy5-C' dots (purple) and PEG-sulfo-Cy5.5-C' dots (blue) highlighting the substantially more hydrophobic behavior of the latter. (d) HPLC chromatograms of PEG-Cy5(+)-C' dots (dark green) and PEG-Cy5.5(+)-C' dots (light green).

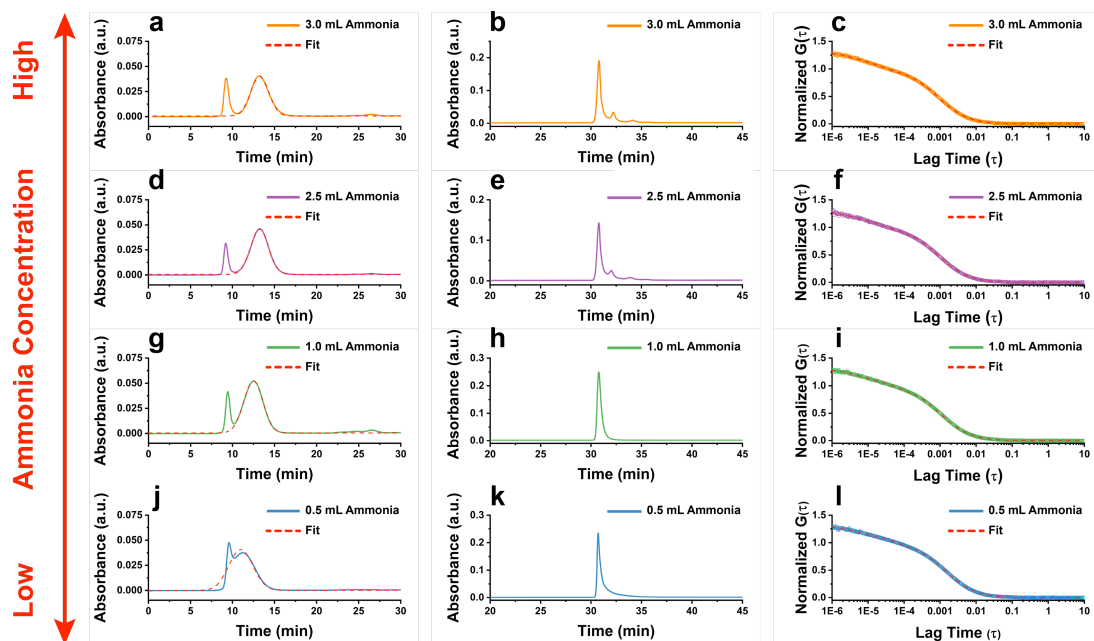


**Figure 3.3:** (a-c) GPC (left row), HPLC (middle row), and FCS (right row) of PEG-Cy5(+)-C' dots made with a starting ammonia concentration of 6 mM. (d-f) GPC, HPLC, and FCS of PEG-Cy5(+)-C' dots made with a starting ammonia concentration of 5 mM. (g-i) GPC, HPLC, and FCS of PEG-Cy5(+)-C' dots made with a starting ammonia concentration of 2 mM. (j-l) GPC, HPLC, and FCS of PEG-Cy5(+)-C' dots made with a starting ammonia concentration of 1 mM.

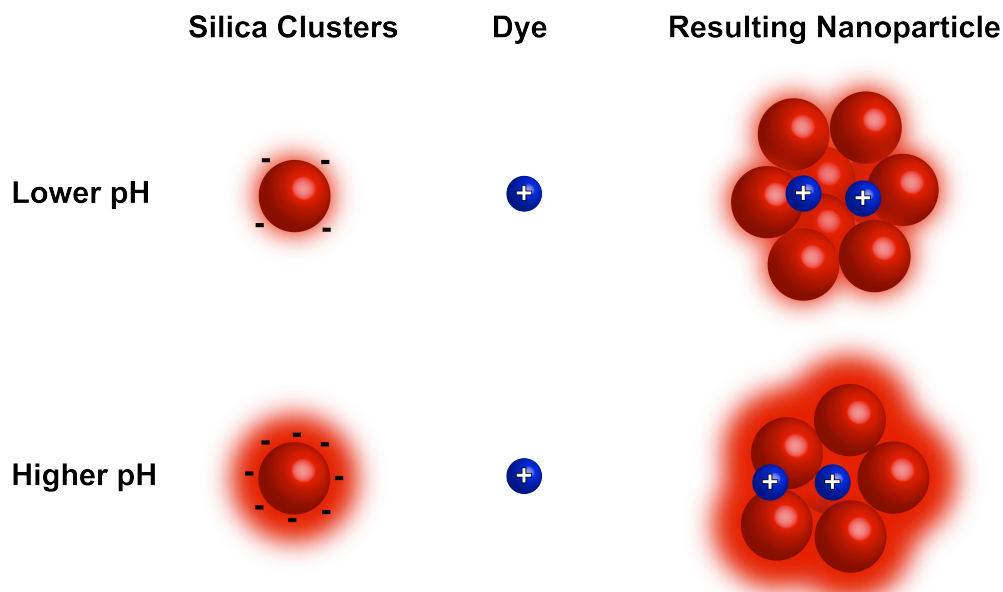


**Figure 3.4:** Schematic of silica nanoparticle growth via the aggregation of primary silica clusters (red) around positively charged dyes (blue). The red halo around the silica clusters symbolizes the net negative cluster charge increasing with higher pH conditions.

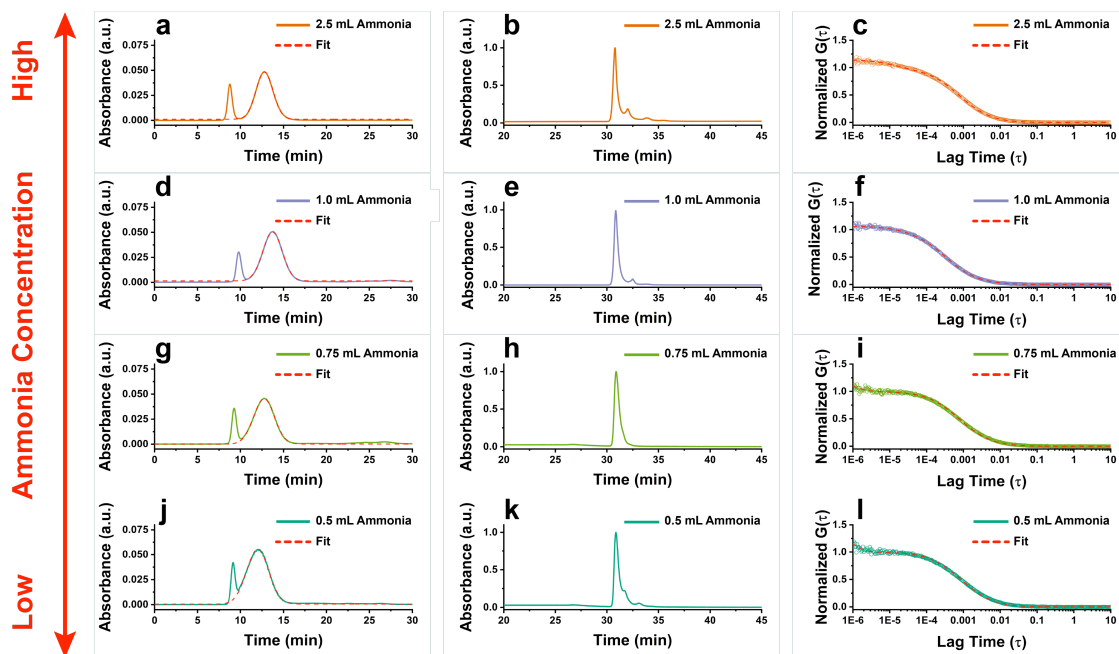


**Figure 3.5:** (a-c) GPC (left row), HPLC (middle row), and FCS (right row) of PEG-Cy5.5(+)-C' dots made with a starting ammonia concentration of 5 mM. (d-f) GPC, HPLC, and FCS of PEG-Cy5.5(+)-C' dots made with a starting ammonia concentration of 2 mM. (g-i) GPC, HPLC, and FCS of PEG-Cy5.5(+)-C' dots made with a starting ammonia concentration of 1.5 mM. (j-l) GPC, HPLC, and FCS of PEG-Cy5.5(+)-C' dots made with a starting ammonia concentration of 1 mM.

Dye	Volume of Ammonia [mL]	Size [nm]	Brightness Per Particle [kHz]	Dyes Per Particle [#]
<b>Cy5(+)-Maleimide</b>	<b>0.50</b>	<b>8.6 ± 0.3</b>	<b>2.42 x 10<sup>4</sup></b>	<b>2.0</b>
	<b>1.00</b>	<b>6.3 ± 0.2</b>	<b>2.27 x 10<sup>4</sup></b>	<b>1.9</b>
	<b>2.50</b>	<b>5.5 ± 0.1</b>	<b>2.22 x 10<sup>4</sup></b>	<b>1.6</b>
	<b>3.00</b>	<b>5.3 ± 0.0</b>	<b>2.14 x 10<sup>4</sup></b>	<b>1.9</b>
<b>Cy5.5(+)-Maleimide</b>	<b>0.50</b>	<b>6.1 ± 0.1</b>	<b>4.02 x 10<sup>3</sup></b>	<b>2.4</b>
	<b>0.75</b>	<b>5.5 ± 0.1</b>	<b>4.16 x 10<sup>3</sup></b>	<b>2.5</b>
	<b>1.00</b>	<b>5.5 ± 0.1</b>	<b>4.16 x 10<sup>3</sup></b>	<b>2.5</b>
	<b>2.50</b>	<b>5.0 ± 0.1</b>	<b>3.91 x 10<sup>3</sup></b>	<b>1.8</b>

**Table 3.1:** Tabulated results of the FCS analysis of the samples shown in Figures 3.3 and 3.4.

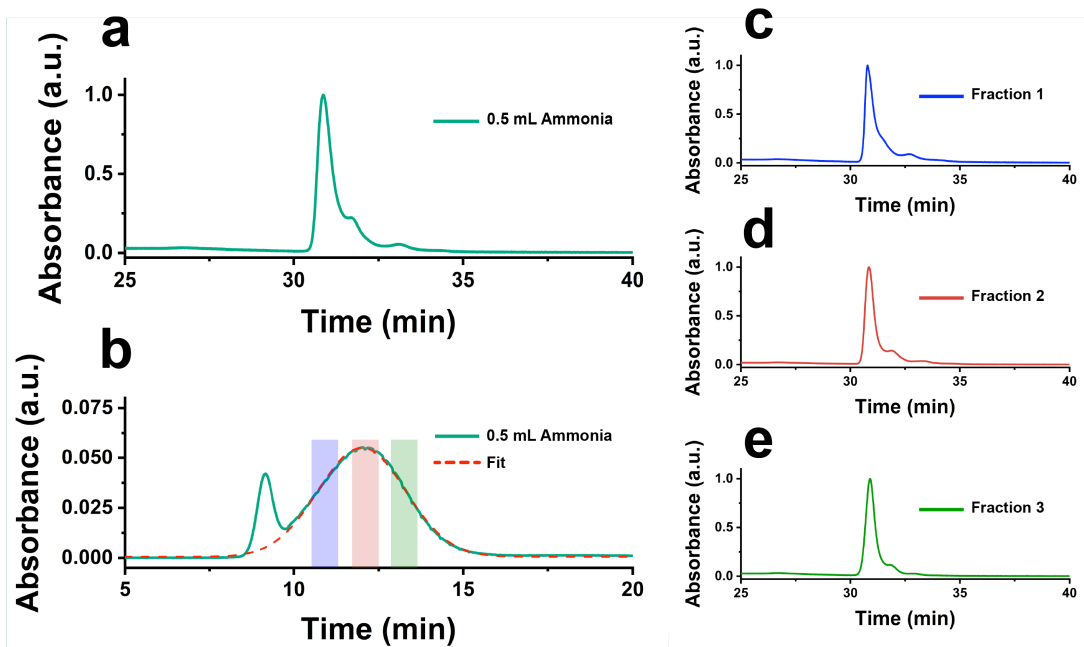


**Figure 3.6:** (a) HPLC chromatogram of PEG-Cy5.5-C' dots synthesized at a starting ammonia concentration of 1 mM. (b) GPC of PEG-Cy5.5-C' dots synthesized at a starting ammonia concentration of 1 mM, the shaded regions highlight the area under the curve that was fractionated and combined for GPC-HPLC of the sample in c-e. (c-e) HPLC chromatograms of GPC fractionated PEG-Cy5.5-C' dots (c) are the largest nanoparticles, (d) are average sized nanoparticles, and (e) are the smallest nanoparticles from the GPC fractionation.

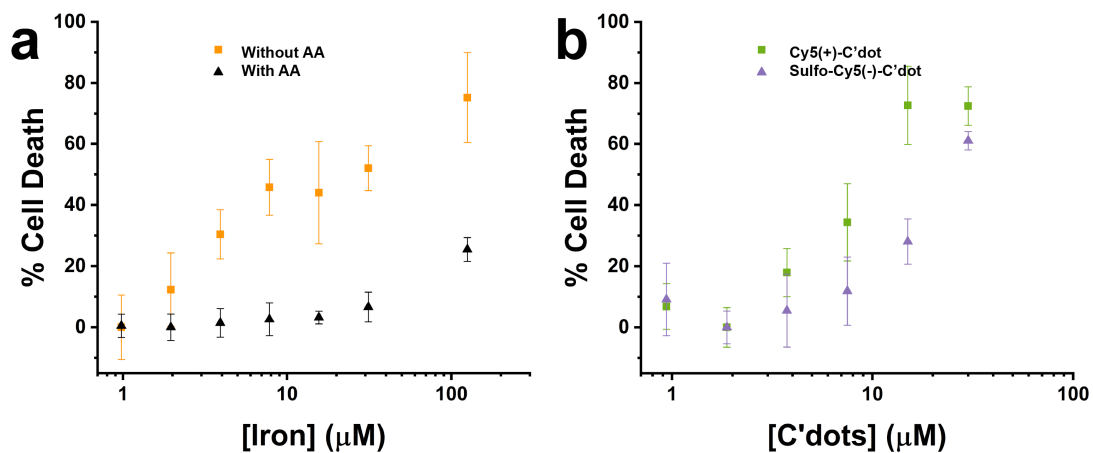


**Figure 3.7:** (a) Cell death experiments on MDA-MB-468 cells using iron(III) nitrate in both complete media (triangle) and in amino acid (AA) deprived media (square). (b) Cell death experiments on MDA-MB-468 cells in AA deprived media comparing the efficacy of PEG-Cy5(+)-C' dots and PEG-sulfoCy5-C' dots in the presence of a non-toxic amount of iron (1 μM).

## REFERENCES

1. Bobo, D.; Robinson, K. J.; Islam, J.; Thurecht, K. J.; Corrie, S. R., Nanoparticle-Based Medicines: A Review of FDA-Approved Materials and Clinical Trials to Date. *Pharm Res* **2016**, *33* (10), 2373-2387.
2. Sun, Y.; Xia, Y., Shape-controlled synthesis of gold and silver nanoparticles. *Science* **2002**, *298* (5601), 2176-2179.
3. Santra, S.; Kaittanis, C.; Grimm, J.; Perez, J. M., Drug/Dye-Loaded, Multifunctional Iron Oxide Nanoparticles for Combined Targeted Cancer Therapy and Dual Optical/Magnetic Resonance Imaging. *Small* **2009**, *5* (16), 1862-1868.
4. Schneider, C. S.; Xu, Q.; Boylan, N. J.; Chisholm, J.; Tang, B. C.; Schuster, B. S.; Henning, A.; Ensign, L. M.; Lee, E.; Adstamongkonkul, P.; Simons, B. W.; Wang, S. S.; Gong, X.; Yu, T.; Boyle, M. P.; Suk, J. S.; Hanes, J., Nanoparticles that do not adhere to mucus provide uniform and long-lasting drug delivery to airways following inhalation. *Science Advances* **2017**, *3*, 1-10.
5. Stylianopoulos, T.; Jain, R. K., Design considerations for nanotherapeutics in oncology. *Nanomedicine* **2015**, *11* (8), 1893-1907.
6. Dawidczyk, C. M.; Kim, C.; Park, J. H.; Russell, L. M.; Lee, K. H.; Pomper, M. G.; Searson, P. C., State-of-the-art in design rules for drug delivery platforms: lessons learned from FDA-approved nanomedicines. *J Control Release* **2014**, *187*, 133-144.
7. Murphy, C. J.; Buriak, J. M., Best Practices for the Reporting of Colloidal Inorganic Nanomaterials. *Chemistry of Materials* **2015**, *27* (14), 4911-4913.
8. Kao, T.; Kohle, F.; Ma, K.; Aubert, T.; Andrievsky, A.; Wiesner, U., Fluorescent Silica Nanoparticles with Well-Separated Intensity Distributions from Batch Reactions. *Nano Lett* **2018**, *18* (2), 1305-1310.
9. Gardinier, T. C.; Kohle, F. F. E.; Peerless, J. S.; Ma, K.; Turker, M. Z.; Hinckley, J. A.; Yingling, Y. G.; Wiesner, U., High-Performance Chromatographic Characterization of Surface Chemical Heterogeneities of Fluorescent Organic-Inorganic Hybrid Core-Shell Silica Nanoparticles. *ACS Nano* **2019**, *13* (2), 1795-1804.
10. Turker, M. Z.; Gardinier, T. C.; Hinckley, J. A.; Contreras, C. B.; Woodruff, F.; Ma, K.; Kohle, F. F. E.; Wiesner, U. B., Inner and Outer Surface Functionalization of Ultrasmall Fluorescent Silica Nanorings as shown by High-Performance Liquid Chromatography. *Chemistry of Materials* **2019**, 10.1021/acs.chemmater.9b01236.

11. Mullen, D. G.; Desai, A. M.; Waddell, J. N.; Cheng, X. M.; Kelly, C. V.; McNerny, D. Q.; Majoros, I. J.; Baker, J. R., Jr.; Sander, L. M.; Orr, B. G.; Banaszak Holl, M. M., The Implications of Stochastic Synthesis for the Conjugation of Functional Groups to Nanoparticles. *Bioconjug Chem* **2008**, *19* (9), 1748-1752.
12. Mullen, D. G.; Fang, M.; Desai, A.; Baker, J. R.; Orr, B. G.; Banaszak Holl, M. M., A Quantitative Assessment of Nanoparticle-Ligand Distributions: Implications for Targeted Drug and Imaging Delivery in Dendrimer Conjugates. *ACS Nano* **2010**, *4* (2), 657-670.
13. Lee, S.-W.; Berger, S. J.; Martinovic, S.; Pasa-Tolic, L.; Anerson, G. A.; Shen, Y.; Zhao, R.; Smith, R. D., Direct mass spectrometric analysis of intact proteins of the yeast large ribosomal subunit using capillary LC/FTICR. *PNAS* **2002**, *99* (9), 5942-5947.
14. Fenn, J. B.; Mann, M.; Meng, C. K.; Wong, S. F.; Whitehouse, C. M., Electrospray Ionization for Mass Spectrometry of Large Biomolecules. *Science* **1989**, *246*, 64-71.
15. Aebersold, R.; Mann, M., Mass Spectrometry-Based Proteomics. *Nature* **2003**, *422*, 198-207.
16. Yoo, B.; Ma, K.; Wiesner, U.; Bradbury, M., Expanding Analytical Tools for Characterizing Ultrasmall Silica-based Nanoparticles. *RSC Adv* **2017**, *7* (27), 16861-16865.
17. Bradbury, M. S.; Phillips, E.; Montero, P. H.; Cheal, S. M.; Stambuk, H.; Durack, J. C.; Sofocleous, C. T.; Meester, R. J.; Wiesner, U.; Patel, S., Clinically-translated silica nanoparticles as dual-modality cancer-targeted probes for image-guided surgery and interventions. *Integr Biol (Camb)* **2013**, *5* (1), 74-86.
18. Phillips, E.; Penate-Medina, O.; Zanzonico, P. B.; Carvajal, R. D.; Mohan, P.; Ye, Y.; Humm, J.; Gonen, M.; Kalaigian, H.; Schoder, H.; Strauss, H. W.; Larson, S. M.; Wiesner, U.; Bradbury, M. S., Clinical Translation of an Ultrasmall Inorganic Optical-PET Imaging Nanoparticle Probe. *Sci Transl Med* **2014**, *6* (260), 1-9.
19. Ma, K.; Mendoza, C.; Hanson, M.; Werner-Zwanziger, U.; Zwanziger, J.; Wiesner, U., Control of Ultrasmall Sub-10 nm Ligand-Functionalized Fluorescent Core-Shell Silica Nanoparticle Growth in Water. *Chemistry of Materials* **2015**, *27* (11), 4119-4133.
20. Ma, K.; Zhang, D.; Cong, Y.; Wiesner, U., Elucidating the Mechanism of Silica Nanoparticle PEGylation Processes Using Fluorescence Correlation Spectroscopies. *Chemistry of Materials* **2016**, *28* (5), 1537-1545.

21. Hong, G.; Antaris, A. L.; Dai, H., Near-infrared fluorophores for biomedical imaging. *Nature Biomedical Engineering* **2017**, *1* (1), 1-22.
22. Ernst, L. A.; Gupta, R. K.; Mujumdar, R. B.; Waggoner, A. S., Cyanine dye labeling reagents for sulfhydryl groups. *Cytometry* **1989**, *10* (1), 3-10.
23. Mujumdar, R. B.; Ernst, L. A.; Mujumdar, S. R.; Lewis, C. J.; Waggoner, A. S., Cyanine dye labeling reagents: Sulfoindocyanine succinimidyl esters. *Bioconjugate Chemistry* **2002**, *4* (2), 105-111.
24. Kim, S. E.; Zhang, L.; Ma, K.; Riegman, M.; Chen, F.; Ingold, I.; Conrad, M.; Turker, M. Z.; Gao, M.; Jiang, X.; Monette, S.; Pauliah, M.; Gonen, M.; Zanzonico, P.; Quinn, T.; Wiesner, U.; Bradbury, M. S.; Overholtzer, M., Ultrasmall nanoparticles induce ferroptosis in nutrient-deprived cancer cells and suppress tumour growth. *Nat Nanotechnol* **2016**, *11* (11), 977-985.
25. Carcouet, C. C.; van de Put, M. W.; Mezari, B.; Magusin, P. C.; Laven, J.; Bomans, P. H.; Friedrich, H.; Esteves, A. C.; Sommerdijk, N. A.; van Benthem, R. A.; de With, G., Nucleation and growth of monodisperse silica nanoparticles. *Nano Lett* **2014**, *14* (3), 1433-1438.
26. Herz, E.; Ow, H.; Bonner, D.; Burns, A.; Wiesner, U., Dye structure–optical property correlations in near-infrared fluorescent core-shell silica nanoparticles. *Journal of Materials Chemistry* **2009**, *19* (35).
27. Ocana, M.; Rodriguez-Clemente, R.; Serna, C. J., Uniform Colloidal Particles in Solution - Formation Mechanisms. *Advanced Materials* **1995**, *7* (2), 212-216.
28. Caruso, F.; Lichtenfeld, H.; Giersig, M.; Möhwald, H., Electrostatic Self-Assembly of Silica Nanoparticle–Polyelectrolyte Multilayers on Polystyrene Latex Particles. *Journal of the American Chemical Society* **1998**, *120* (33), 8523-8524.
29. Barisik, M.; Atalay, S.; Beskok, A.; Qian, S., Size Dependent Surface Charge Properties of Silica Nanoparticles. *The Journal of Physical Chemistry C* **2014**, *118* (4), 1836-1842.
30. Brinker, C. J.; Scherer, G. W., *Sol-Gel Science: The Physics and Chemistry of Sol-Gel Processing*. Academic Press: 1990.
31. Ma, K.; Wiesner, U., Modular and Orthogonal Post-PEGylation Surface Modifications by Insertion Enabling Penta-Functional Ultrasmall Organic-Silica Hybrid Nanoparticles. *Chemistry of Materials* **2017**, *29* (16), 6840-6855.
32. Barteau, K. P.; Ma, K.; Kohle, F. F. E.; Gardinier, T. C.; Beaucage, P. A.; Gillilan, R. E.; Wiesner, U., Quantitative Measure of the Size Dispersity in

Ultrasmall Fluorescent Organic-Inorganic Hybrid Core-Shell Silica Nanoparticles by Small-angle X-ray Scattering. *Chem Mater* **2019**, *31* (3), 643-657.

CHAPTER 4  
ULTRASMALL SILICA NANOPARTICLE TOPOLOGY MODULATES  
BIODISTRIBUTION AND RENAL CLEARANCE

***Abstract***

Nanoscale topologies and their functions in biology have always been an inspiration to, and driven the curiosity of, scientists across different disciplines.<sup>1-4</sup> Recently, there has been growing interest in the topological engineering of synthetic ultrasmall nanoparticles (UNPs) with dimensions around 10 nm.<sup>5-11</sup> In part, this is motivated by the physical cut-off for renal clearance in this regime,<sup>6,7</sup> *e.g.* in the human body. However, the precise role of UNP topology in modulating biological response largely remains unknown due to the lack of appropriate model systems.<sup>8,9</sup> Here we study the biodistribution and pharmacokinetics in mice of ultrasmall fluorescent silica NPs with three topologies: spheres, dodecahedral cages, and rings.<sup>5,11,12</sup> In contrast to spherical particles, whose uptake in organs (liver, spleen) of the reticuloendothelial system (RES) increases with increasing diameter, for this sequence of topologies we observe a decrease in RES uptake despite increasing size. Furthermore, rings still get cleared via the urine even for diameters as large as 13-14 nm, *i.e.* well above the renal cut-off.<sup>6</sup> We explain these findings *via* particle deformability increasing in the direction from spheres, cages, to rings. Results reveal a hitherto neglected parameter in UNP design, which may open up fascinating new research directions in bioimaging and nanomedicine.

## ***Introduction***

To precisely engineer the topology of UNPs made from silica, recently developed aqueous synthesis approaches were applied, in which tetramethyl orthosilicate (TMOS) with fast hydrolysis rate was used as silica precursor, while cetyl-trimethylammonium bromide (CTAB) and 1,3,5-trimethylbenzene (mesitylene, TMB) were used as structure directing and swelling agents, respectively.<sup>5,12,13</sup> The different UNP topologies were controlled, in part, by adjusting the concentration of CTAB and TMB, which directed the self-assembly of primary silica clusters formed upon the addition of TMOS into water at pH around 8.5.<sup>13</sup> When CTAB and TMB were absent, spherically shaped silica cores with diameters around 4 nm were formed via the aggregation and condensation of primary silica clusters in solution.<sup>13,14</sup> When TMB swollen CTAB micelles were introduced before the addition of TMOS, they directed the assembly of negatively charged primary silica clusters on their positively charged surfaces, leading to the formation of silica rings or dodecahedral silica cages depending on cluster concentration (Methods).<sup>5,12</sup> For all particle topologies, fluorescent dyes were covalently encapsulated in the silica matrix, endowing the particles with fluorescence,<sup>13</sup> and silica surfaces were coated with poly(ethylene glycol) (PEG) for steric stability and improved biocompatibility.<sup>13-17</sup> All particles were functionalized with deferoxamine (DFO),<sup>18</sup> a chelator *e.g.* for zirconium-89 (<sup>89</sup>Zr,  $t_{1/2}$ =78.4 h) enabling positron emission tomography (PET) based quantitative biodistribution analysis (see Methods). Particles were finally purified via gel

permeation chromatography (GPC) as described elsewhere,<sup>13</sup> providing single-GPC-peak high-purity products for further use (Figure 4.4c,f,i).

### ***Results and Discussion***

Hydrodynamic particle diameters were determined using fluorescence correlation spectroscopy (FCS),<sup>13</sup> while details of the particle topology and silica core diameters were characterized by transmission electron microscopy (TEM).<sup>5,12,13</sup> From TEM the larger size of cages and rings relative to spheres was easily discerned (Figure 4.1), while detailed inspection of individual images (see insets in Figure 4.1b,c) revealed characteristic features of silica cage and ring topologies, respectively, as established in earlier studies.<sup>5,12</sup> Silica core diameters measured by TEM for spheres, cages, and rings shown in Figure 4.1 were 7.3 nm, 11.8 nm and 12.1 nm, while their hydrodynamic sizes measured by FCS were 7.8 nm, 10.5 nm, and 8.2 nm, respectively (Figures 4.4 and 4.5). While for spherical particles FCS provides a larger diameter than TEM owing to PEG and dragged water shells, it underestimates the diameters of cages and rings due to the assumption of a spherical shape in the model-based analysis.<sup>16</sup> From the combination of FCS and UV/VIS spectroscopy analyses, the numbers of dyes/DFO per particle were 1.6/3.3, 2.9/4, and 1.5/1.7 for spheres, cages, and rings shown in Figure 4.1, respectively (Figure 4.4).

The fully characterized UNPs with different topologies were radiolabeled with <sup>89</sup>Zr, and intravenously (*i.v.*) injected into non-tumor-bearing nude mice, using

protocols described previously.<sup>18</sup> PET scans were then performed at different time points up to 1 week (see Methods) to study time-dependent particle biodistribution and clearance profiles. From results shown in Figure 4.2, as expected at the early time point of 1 hour after *i.v.* post-injection, for all topologies strong signals were observed in heart and liver, consistent with circulation of the particles in the blood stream. At one and two-day time points, signal is already strongly diminished, with signal in the bladder in particular for rings at 1 and 48 hour time points suggesting renal clearance. Most surprisingly, substantial liver uptake at the final time point was not observed for any of the three different particle topologies. Furthermore, for that time point liver uptake decreased from 6.5, to 4.1, and to 2.1 percent injected dose per gram tissue (%ID/g) in the sequence spheres, cages, and rings, with the value of 2.1 percent for rings being the lowest reported to date for such ultras-small silica nanoparticles over that time frame. The concomitant decrease in spleen uptake suggests reduced uptake by the reticuloendothelial system (RES) and increased renal clearance efficiency (Figure 4.6) in the same sequence.

The biodistribution of conventional spherical UNPs is highly dependent on particle diameter in this size regime; *e.g.* liver uptake substantially increases with increasing particle size while the ability to clear via the kidneys usually diminishes. To illustrate this behavior, in addition to the 7.8 nm dots we synthesized two more spherical nanoparticles with 5.1 nm and 6.9 nm hydrodynamic diameter, respectively, as determined by FCS (data not shown). As expected for this series of spherical silica nanoparticles with increasing size, but otherwise identical structure, liver uptake

increased from 1.4 to 4.4 to 6.5 %ID/g (Figure 4.7 and 4.8). Even though identical spherical particles with even larger sizes could not be synthesized as a result of limitations of the synthetic approach in water,<sup>13</sup> following this trend and supported by previous studies on similar particles,<sup>19</sup> even higher liver uptake is expected for the larger cage and ring shaped nanoparticles with diameters above 8 nm. Clearly, however, the opposite trend is observed with the largest diameter objects, *i.e.* the rings, showing the smallest liver uptake. To verify that cages and rings with silica core diameters slightly below and above 12 nm, respectively, as determined by TEM could get renally cleared without degradation, for both topologies we collected urine from mice at 2-hour time points post *i.v.* injection and performed TEM on these samples (Methods). Experiments confirmed the structural integrity of both particles after renal excretion (Figure 4.3).

Result suggest that biodistribution of UNPs is not only governed by particle size, but also depends on particle topology. We suspect that the silica cages and rings can easily deform as a result of the very thin structural elements from which they are built, *i.e.* ~2 nm diameter primary silica clusters that are condensed into the struts and vertices of the cages and the backbone of the rings.<sup>5,12</sup> At this length scale, almost every material is flexible.<sup>20</sup> Therefore, although their overall size is larger than the cut-off for renal clearance,<sup>6</sup> they can still undergo glomerular filtration<sup>7</sup> in the kidneys by being “squeezed” as illustrated for rings in Figure 4.3g. It is interesting to note that if *e.g.* rings are fully squeezed together to their backbone, the combined diameter of the two silica struts next to each other is about 4 nm, close to the silica core size of the

smallest spherical nanoparticle tested in this study, and consistent with its low liver uptake (1.8 vs. 2.1 %ID/g). The concept of nanoparticle deformation is supported by the blood circulation half-life of the rings that is substantially longer than that of the smaller spherical dots with similarly low liver uptake,<sup>18</sup> (see Figure 4.9), as the rings can only pass glomerular filtration when they get squeezed, which takes time.

Metabolic cage studies were performed (see Methods) on ring particles to elucidate the exact clearance pathways for this topology. About 30 and 40 %ID/g were cleared out by hepatic and renal pathways, respectively, as shown in Figure 4.10. Compared to ~5-6 nm spheres the hepatic clearance of this topology is higher (30 vs. ~5 %ID/g).<sup>18</sup> As hepatic clearance takes longer than renal clearance,<sup>21</sup> this is consistent with the increased blood circulation half-life of rings, where we measured blood-activity of 12 %ID/g at the 24-hour post *i.v.* injection point.

The largest silica ring structure we could synthesize and test in mice had a silica ring diameter as detected by TEM of 13.5 nm. Its biodistribution (Figure 4.11) was very similar to that of the 12.1 nm diameter rings shown in Figure 4.2, with liver uptake at the 1-week post *i.v.* injection time-point of only 2.6 % ID/g. Compared to the ~4 nm silica core sized spherical particles that showed similarly low liver uptake in mice (compare to Figure 4.7), this large ring with ~2 nm thick silica core has a much larger theoretical silica surface area, ~227 nm<sup>2</sup> as compared to ~50 nm<sup>2</sup> for the sphere. This suggests a substantially improved loading capacity for molecules like targeting moieties, chelators for radiolabels, or pharmaceutical drugs, via silica surface

functionalization. Relative to spherical UNPs, the combination of higher loading capacity, lower liver uptake, higher blood circulation times, and the ability to effectively “hide”, *e.g.* hydrophobic molecules on their inside,<sup>16</sup> makes these more complex topologies of cages and rings promising subjects for advanced nanomaterials applications in biology in general, and nanomedicine in particular.

## ***Methods***

### ***Chemicals and Materials***

All materials were used as received. 7-diethylaminocoumarin-3-carboxylic acid, succinimidyl ester (DEAC) was purchased from Anaspec. Cyanine5.0 maleimide (Cy5) was purchased from GE Healthcare. Hexadecyltrimethyl ammonium bromide (CTAB,  $\geq 99\%$ ), tetramethyl orthosilicate (TMOS,  $\geq 99\%$ ), 2.0 M ammonium hydroxide in ethanol, (3-aminopropyl)trimethoxysilane (APTMS, 97%), and anhydrous dimethyl sulfoxide (DMSO,  $\geq 99\%$ ) were purchased from Sigma Aldrich. (3-Aminopropyl) trimethoxysilane (APTMS), 2-[methoxy (polyethylene oxy) 6-9propyl] trimethoxysilane (PEG-Silane, 6-9 ethylene glycol units, PEG-silane (6EO)), (3-mercaptopropyl) trimethoxysilane (MPTMS, 95%), and methoxy triethyleneoxy propyl trimethoxysilane (PEG-silane, 3 ethylene glycol units, PEG-silane (3EO)) were obtained from Gelest. 1,3,5-Trimethylbenzene (Mesitylene/TMB, 99% extra pure) was purchased from Acros Organics. Deferoxamine-Bn-NCS-p (DFO-NCS, 94%) was purchased from Macrocyclics. Absolute anhydrous ethanol (200 proof) was purchased

from Koptec. Glacial acetic acid was purchased from Macron Fine Chemicals. 5.0 M sodium chloride irrigation USP solution was purchased from Santa Cruz Biotechnology. Syringe filters (0.2  $\mu\text{m}$ , PTFE membrane) were purchased from VWR International. Vivaspin sample concentrators (MWCO 30K) and Superdex 200 prep grade were obtained from GE Health Care. Snakeskin dialysis membranes (MWCO 10K) were purchased from Life Technologies. Deionized (DI) water was generated using Millipore Milli-Q system (18.2 M $\Omega$ .cm). Glass bottom microwell dishes for FCS were obtained from MatTek Corporation. Carbon film coated copper grids for TEM was purchased from Electron Microscopy Sciences. BioSuite High Resolution SEC Column (250 Å, 5  $\mu\text{m}$ , 7.8 mm X 300 mm, 10K – 500K) was purchased from Waters Technologies Corporation.

### ***Synthesis of Ultrasmall Nanoparticles with Spherical Shape***

Ultrasmall fluorescent core-shell silica nanoparticles with spherical shape were synthesized in aqueous solution as described previously.<sup>13</sup> Briefly, Cy5 maleimide was conjugated to MPTMS via thiol-maleimide click-chemistry (1:23 ratio) a day prior to synthesis. In the first day of synthesis for a 10 mL reaction batch, 68  $\mu\text{L}$  TMOS and 0.367  $\mu\text{mol}$  Cy5 dye-conjugate were added drop-wise into 0.002 M ammonium hydroxide solution under stirring at 600 r.p.m. at room temperature resulting in the smallest (~5 nm diameter) nanoparticles. For larger particle sizes, synthesis temperature was increased up to 80°C as described previously.<sup>13</sup> The following day, 100  $\mu\text{L}$  PEG-silane (6EO) was added into the reaction solution, which was left stirring

overnight at room temperature. The next day, in order to achieve full covalent attachment of PEG-silane molecules onto the silica core surface, the reaction was left heated at 80°C overnight without stirring. The reaction solution was then cooled down to room temperature, and 2  $\mu\text{L}$  APTMS was added into the reaction at 600 r.p.m. stirring at room temperature for post-pegylation surface modification by insertion (PPSMI).<sup>15</sup> The following day, 0.42 mmol of DFO-NCS chelator was added to the solution to react with the primary amines on the silica surface via amine-NCS conjugation.

### ***Synthesis of Ultrasmall Nanoparticles with Dodecahedral Cage and Ring Topologies***

Ultrasmall fluorescent dodecahedral silica cages and rings were synthesized in aqueous solution via micelle templating as described previously.<sup>5,12</sup> Briefly, succinimidyl ester derivative of DEAC dye was conjugated with APTES via amine-ester conjugation-chemistry (1:25 ratio) a day prior to synthesis. On the first day of synthesis for a 10 mL reaction batch, CTAB (125 mg for dodecahedral cages, and 83 mg for rings) was dissolved into 10 mL of 0.002 M ammonium hydroxide solution under stirring at 600 r.p.m. at 30°C for 1 hour before the addition of 100  $\mu\text{L}$  TMB to swell the micelles, which was followed by stirring for another hour. TMOS (100  $\mu\text{L}$  for dodecahedral cages, and 68  $\mu\text{L}$  for rings) and 0.2  $\mu\text{mol}$  DEAC-dye conjugate were then added drop-wise to the reaction. The following day, 6EO PEG-silane (150  $\mu\text{L}$  for dodecahedral cages, and 100  $\mu\text{L}$  for rings) was added into the reaction solution, which

was left stirring overnight at 30°C. The next day, in order to achieve full covalent attachment of PEG-silane molecules onto the silica surface, the reaction was left heated at 80°C overnight without stirring. The reaction solution was then cooled down to room temperature, syringe-filtered (MWCO 0.2 μm, PTFE), and transferred into a dialysis membrane (MWCO 10K). The sample was dialyzed in 200 mL of ethanol/deionized water/glacial acetic acid solution (500:500:7 volume ratio), and the acid solution was changed once a day for three days to remove CTAB micelles from the pores of dodecahedral cages and rings, as well as to remove unreacted reagents. Following acid dialysis, the sample was transferred into 5 L deionized water, and the deionized water was refreshed once a day for three days to remove ethanol and acetic acid solvents. Following these dialysis treatments, the reaction batch was transferred back into a round-bottom flask, and 2 μL APTMS was added into the reaction at 600 r.p.m. at room temperature for PPSMI. The following day, 0.42 mmol of DFO-NCS chelators was added to the solution to react with primary amines on the nanoparticle surface via amine-NCS conjugation. After the functionalization with DFO, 100 μL of PEG-silane (3EO) was added into the reaction under stirring overnight in order to further PEGylate the inside surfaces, which had been covered by micelles during the first PEGylation step.<sup>16</sup>

### ***Sample Purification***

After the syntheses of all UNPs, reaction batches were transferred into dialysis membranes (MWCO 10K) for dialysis in deionized water overnight prior to syringe-

filtration (MWCO 0.2  $\mu\text{m}$ , PTFE), after which they were concentrated using spin filters (Vivaspin 20 MWCO 30K) via centrifugation (Eppendorf 5810R) at 4300 r.p.m. for 45 min. Gel permeation chromatography (GPC) was performed on the concentrated samples on a GPC column packed with Superdex 200 prep grade resin using 0.9 wt.% sodium chloride saline as buffer solution, as described previously.<sup>13,15,16</sup> UNPs were separated from the aggregation products and un-reacted reagents via GPC fractionation, and collected samples were run in analytical scale GPC, using a 300 mm x 7.8 mm Waters BioSuite high resolution size exclusion chromatography column at 1 mL/min flow rate to check for sample purity via the occurrence of a single-peak chromatogram. These are the GPC control runs reported in the main text (Figure 4.4c,f,i).

### ***Characterization of Ultrasmall Nanoparticles***

Fluorescence correlation spectroscopy (FCS) measurements were performed on different UNPs using a home built setup as described previously.<sup>13,15,16</sup> A Varian Cary 5000 spectrophotometer was used to measure UV-vis absorption spectra of the samples in order to calculate, together with concentration information from FCS data analysis, the number of dyes and DFO chelators per particle by deconvolution as described previously.<sup>15</sup> Transmission electron microscopy (TEM) was performed on particle samples using a FEI Tecnai T12 Spirit microscope operated at 120 kV as described previously.<sup>5,12</sup>

To study the integrity of dodecahedral cages and rings after circulation and excretion from mice injected with 250  $\mu\text{L}$  of 15  $\mu\text{M}$  UNPs, at the 2- hour time-point post *i.v.* injection urine was collected from the mouse bladder while the animal was under anesthesia. After extraction, the urine sample was immediately diluted with denionized water for TEM sample preparation. For samples collected from urine, more than 15 TEM images were taken per nanoparticle. These images were then averaged to increase the signal-to-noise ratio as described elsewhere.<sup>5</sup>

### ***<sup>89</sup>Zr Radiolabeling of DFO-functionalized Ultrasmall Nanoparticles***

For chelator-based <sup>89</sup>Zr labeling, 1.5 nmol of DFO-functionalized samples were mixed with 1 mCi of <sup>89</sup>Zr-oxalate in HEPES buffer (pH 8) at 37°C for 60 min; final labeling pH was kept around 7-7.5. The labeling yield was monitored by radio ITLC. An EDTA challenge process was then introduced to remove any non-specifically bound <sup>89</sup>Zr to the silica UNP surface. As synthesized <sup>89</sup>Zr-DFO-UNP samples were then purified by using a PD-10 column with the final radiochemical purity quantified using ITLC.

### ***Quantitative Renal and Hepatic Clearance Study on Silica Rings***

To study the renal and hepatic clearance of <sup>89</sup>Zr-DFO-functionalized silica rings, each healthy mouse (6-8 week-old female nude mouse) was injected with about 50  $\mu\text{Ci}$  (1.85 MBq) of <sup>89</sup>Zr-DFO-UNP. Individual mice were kept in a metabolic cage.

At varied post i.v. injection time points (*i.e.*, at 4, 24, 48, 72, 120 and 168 h), both the radioactivity in mouse urine and feces were measured using a CRC® -55tR Dose Calibrator and presented as %ID (mean  $\pm$  SD).

### ***In-Vivo PET Imaging, and Ex-Vivo Biodistribution Studies for Ultrasmall Nanoparticles with Different Topologies***

For PET imaging, mice were *i.v.* injected with  $\sim$ 300  $\mu$ Ci (11.1 MBq)  $^{89}$ Zr-DFO-UNP. PET imaging was performed in a small-animal PET scanner (Focus 120 microPET; Concorde Microsystems) at 1, 24, 48, 72 h and 168 h (one week) post *i.v.* injection. Image reconstruction and region-of-interest (ROI) analysis of the PET data were performed using IRW software, with results presented as percentage injected dose per gram tissue (%ID/g). On day 7, post *i.v.* injection, accumulated activity in major organs was assayed by an Automatic Wizard<sup>2</sup>  $\gamma$ -Counter (PerkinElmer), and presented as %ID/g (mean  $\pm$  SD).

### ***Acknowledgements***

This work was funded by the National Cancer Institute of the National Institutes of Health (NIH) under Award Number U54CA199081. Melik Turker thanks the Ministry of National Education of the Republic of Turkey for his student scholarship support. Melik Turker, Kai Ma, Feng Chen, Michelle Bradbury, and Ulrich Wiesner designed the experiments. Fluorescent silica nanoparticle topologies were synthesized and characterized by Melik Turker, Kai Ma, and Fem Woodruff.

Thomas Gardinier performed analytical scale GPC. Feng Chen performed animal experiments. Melik Turker, Kai Ma, Feng Chen, Michelle Bradbury, and Ulrich Wiesner interpreted the results. Melik Turker, Kai Ma, and Ulrich Wiesner wrote the manuscript with the input of all the authors.

## Figures

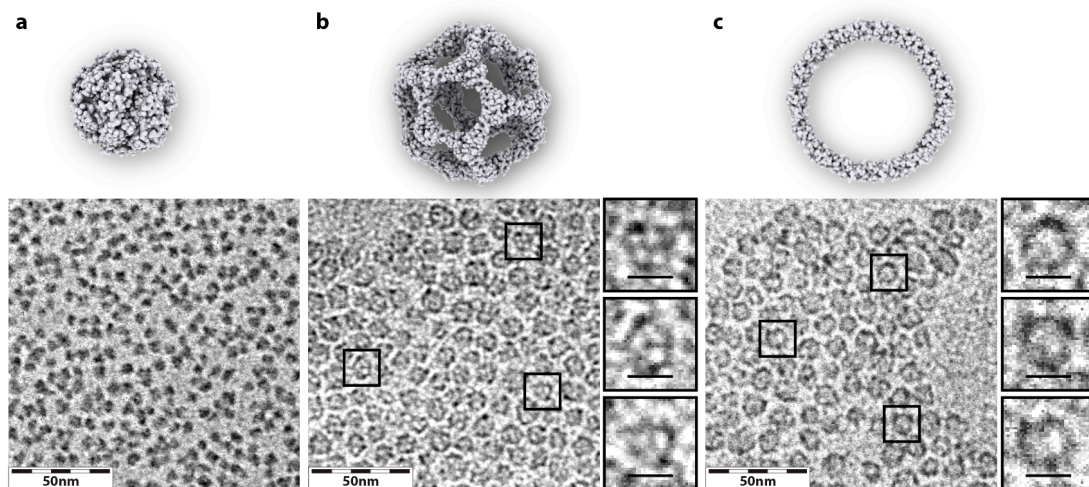


**Figure 4.1:** The three silica nanoparticle topologies studied. Illustration of silica sphere (a), dodecahedral cage (b), and ring (c) topologies, respectively, together with their representative TEM images (d), (e), and (f), respectively. Insets in (b) and (c) show individual particles (scale bar 10 nm).

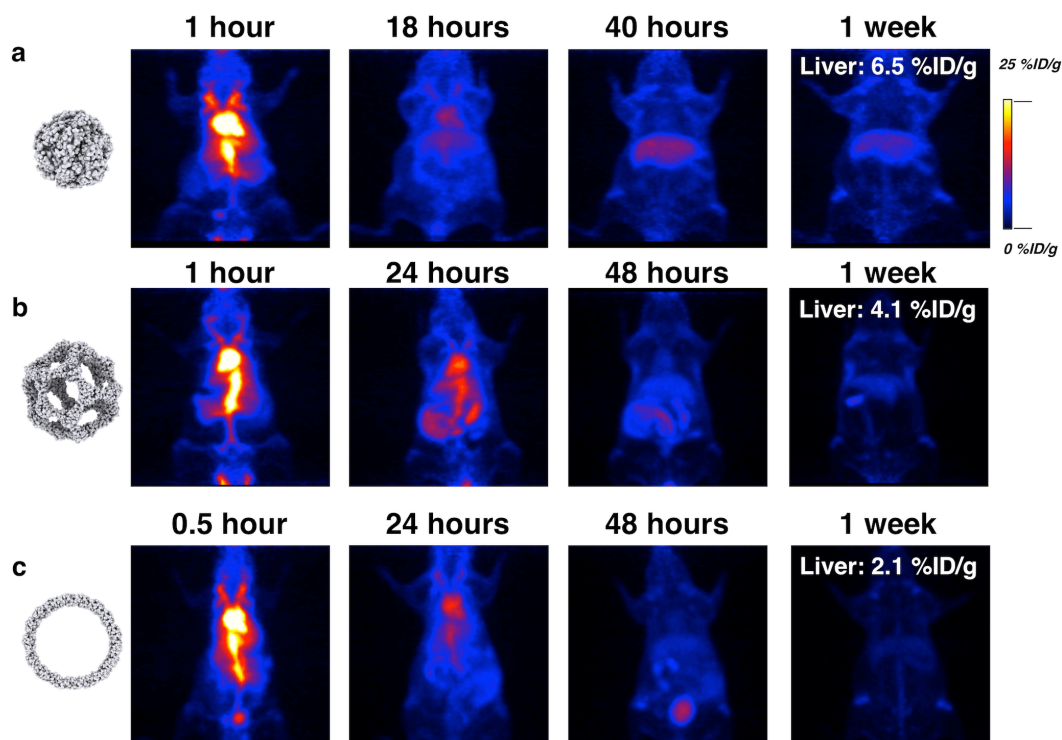


**Figure 4.2:** *In-vivo* PET imaging studies of UNPs with three different topologies in mice ( $n=1$ ). (a) PET images of UNPs with silica core diameters as determined by TEM of (a) 7.3 nm (spheres), (b) 11.8 nm (cages), and (c) 12.1 nm (rings) at 1, ~24, 48 hours, and 1 week time points after *i.v.* injection showing liver uptake of 6.5, 4.1, and 2.1 %ID/g, respectively, at the final 1 week time point.

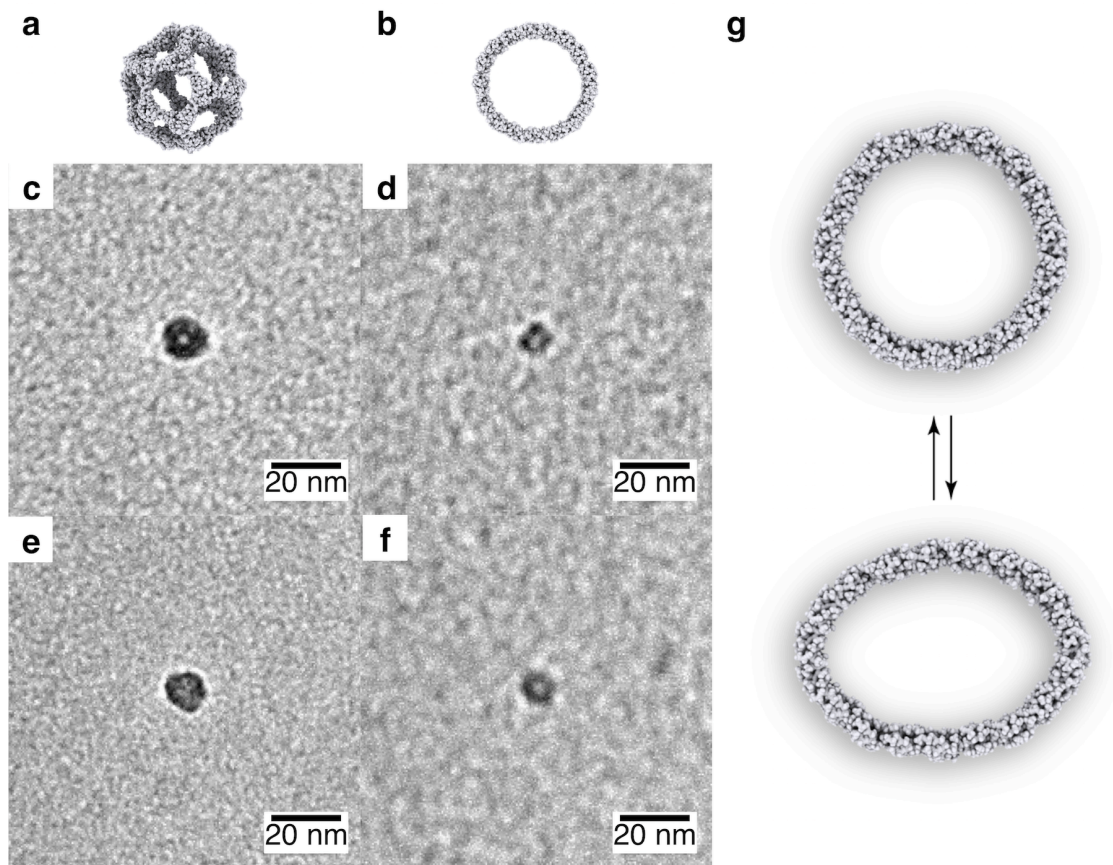


**Figure 4.3:** TEM images of intact UNPs in animal urine, *i.e.*, after getting renally cleared out from the body. Averaged TEM images (see Methods) of two different nanoparticles of each cages (c, e) and rings (d, f), collected from mice urine at the 2-hour time point after i.v. injection together with their illustrations (a, b). (g) Illustration of ring deformation enabling renal clearance.

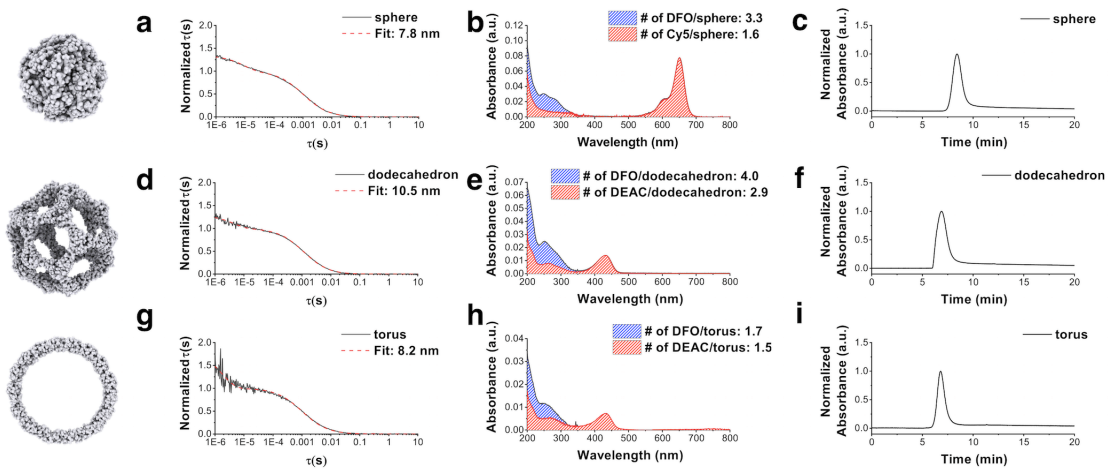


**Figure 4.4:** Comprehensive characterization of particles with different topologies. Characterization of ultraspherical (a-c), dodecahedral cage (d-f), and ring (g-i) particles. (a, d, g) FCS correlation curves with their fits for hydrodynamic sizes. (b, e, h) Deconvolution of the UV-vis spectra for the calculation of numbers of dyes and radiolabel chelators per particle. (c, f, i) Analytical scale GPC chromatograms for purified nanoparticles.

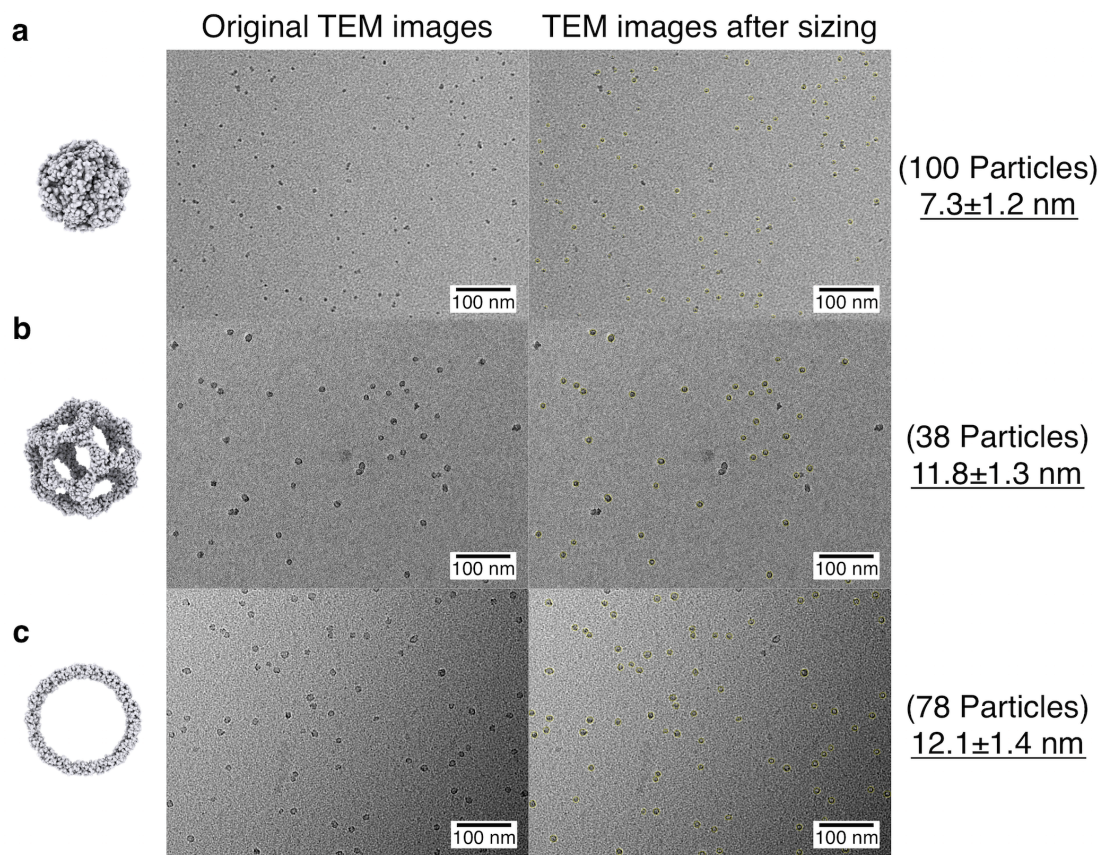


**Figure 4.5:** TEM images for particles with three different topologies for size analysis. Original TEM images with size analysis for spherical (a), dodecahedral cage (b), and ring (c) particles, respectively.

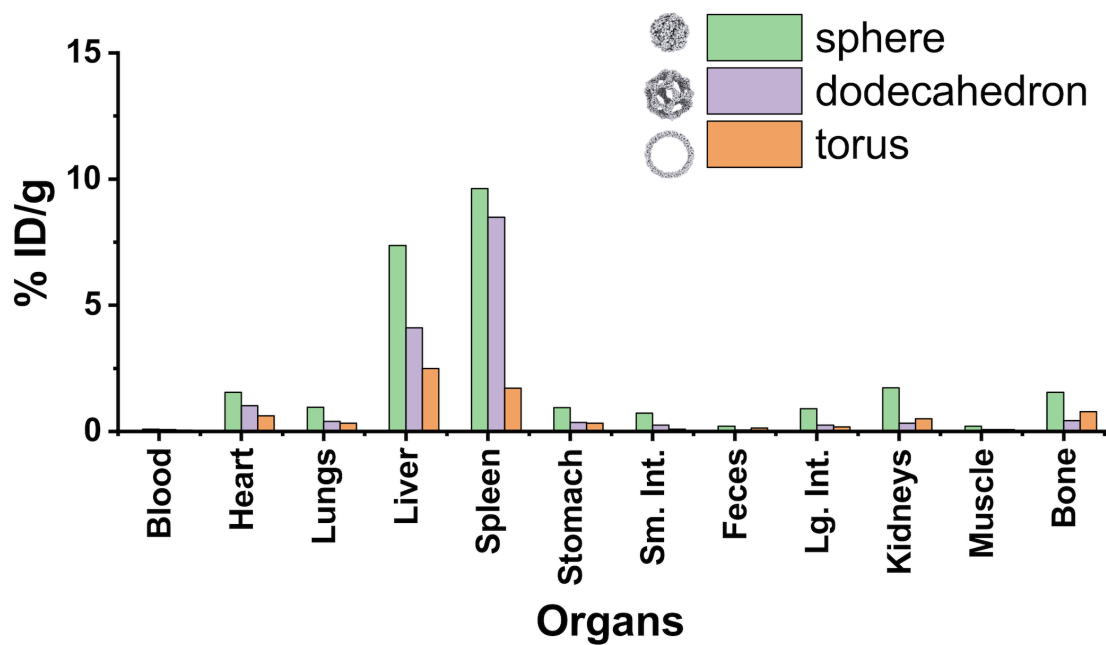


**Figure 4.6:** Biodistribution studies for three UNPs with three different topologies. Biodistribution for ultrasmall spherical (green), dodecahedral cage (purple), and ring (orange) particles at 1 week after *i.v.* injection (n=1).

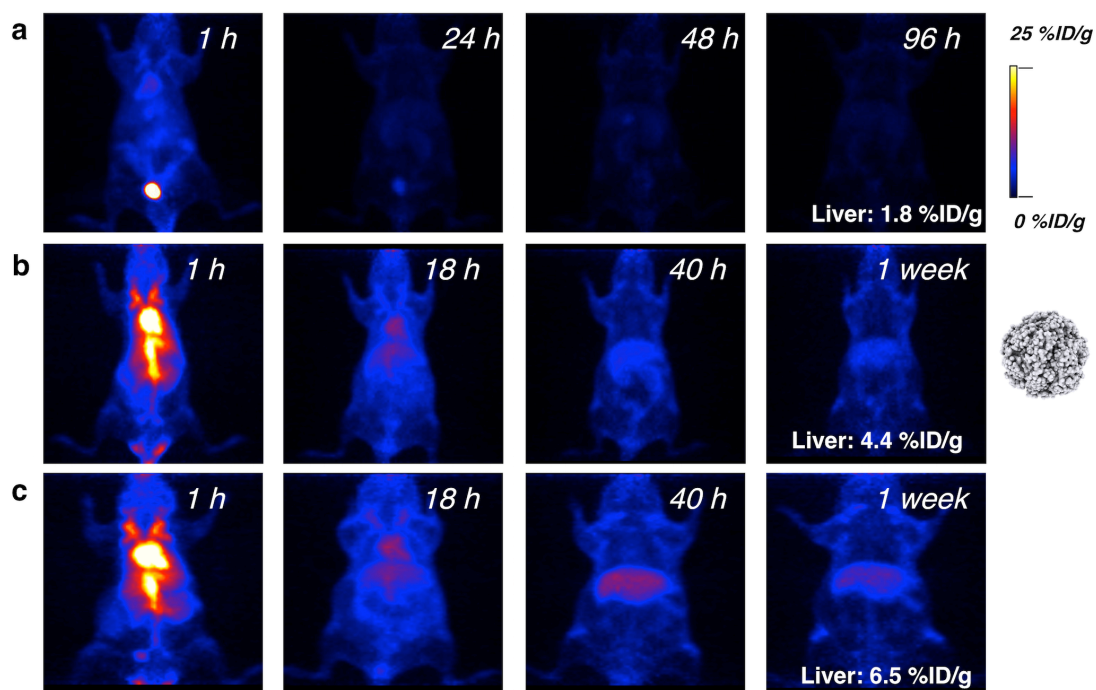


**Figure 4.7:** In vivo PET imaging studies of three differently sized ultrasmall spherical nanoparticles in mice (n=1). (a) PET images of (a) 5.1 nm, (b) 6.9 nm, and (c) 7.8 nm (all by FCS) sized spherical nanoparticles at 1, ~24, ~48, and ~96 hour time points after *i.v.* injection showing 1.8, 4.4, 6.5 %ID/g liver uptake, respectively, in the liver at the final 1 week time point.

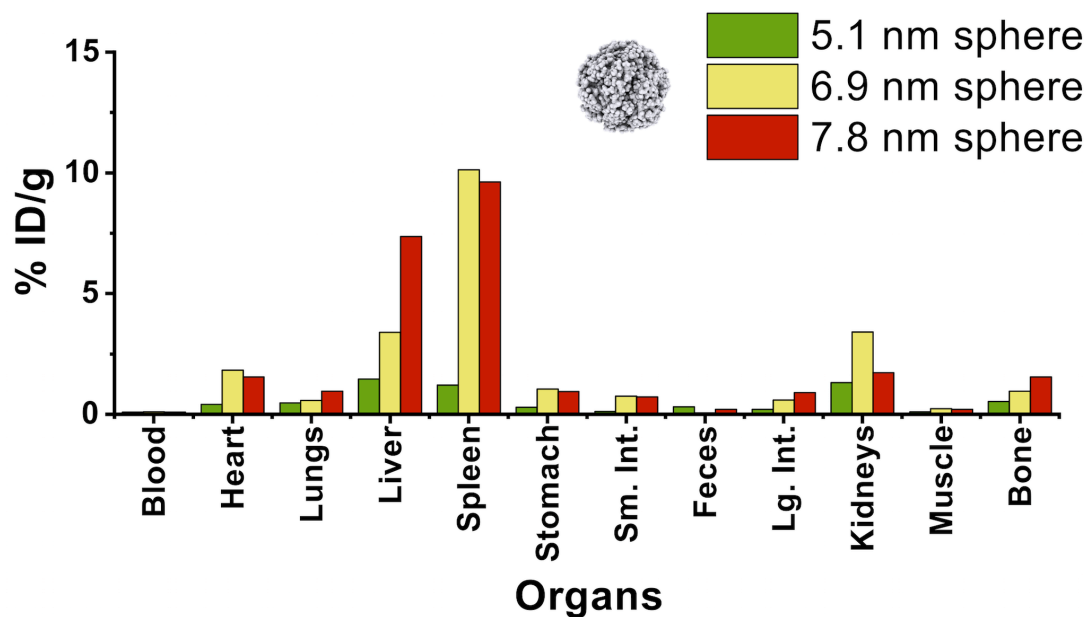


**Figure 4.8:** Biodistribution studies for three differently sized ultraspherical nanoparticles in mice (n=1). Biodistribution results for 5.1 nm (green), 6.9 nm (yellow), and 7.8 nm (red) sized ultraspherical silica nanoparticles (by FCS) at 1 week after *i.v.* injection (n=1).

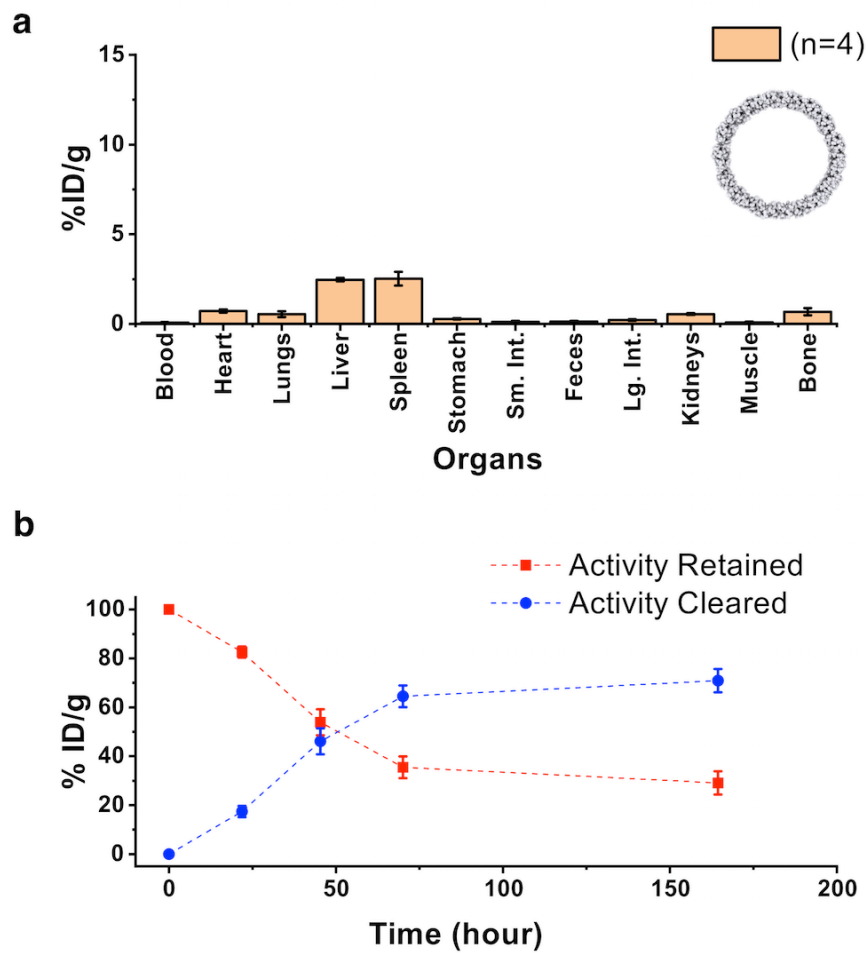


**Figure 4.9:** Biodistribution and clearance profile for ultrasmall nanorings in mice. (a) Biodistribution studies (n=4) on ultrasmall silica rings 1 week after *i.v.* injection showing average of 2.5 %ID/g liver uptake. (b) The activity retention (red), and clearance (blue) profiles for the same rings showing 70.1% total activity clearance (n=4) 1 week after *i.v.* injection.

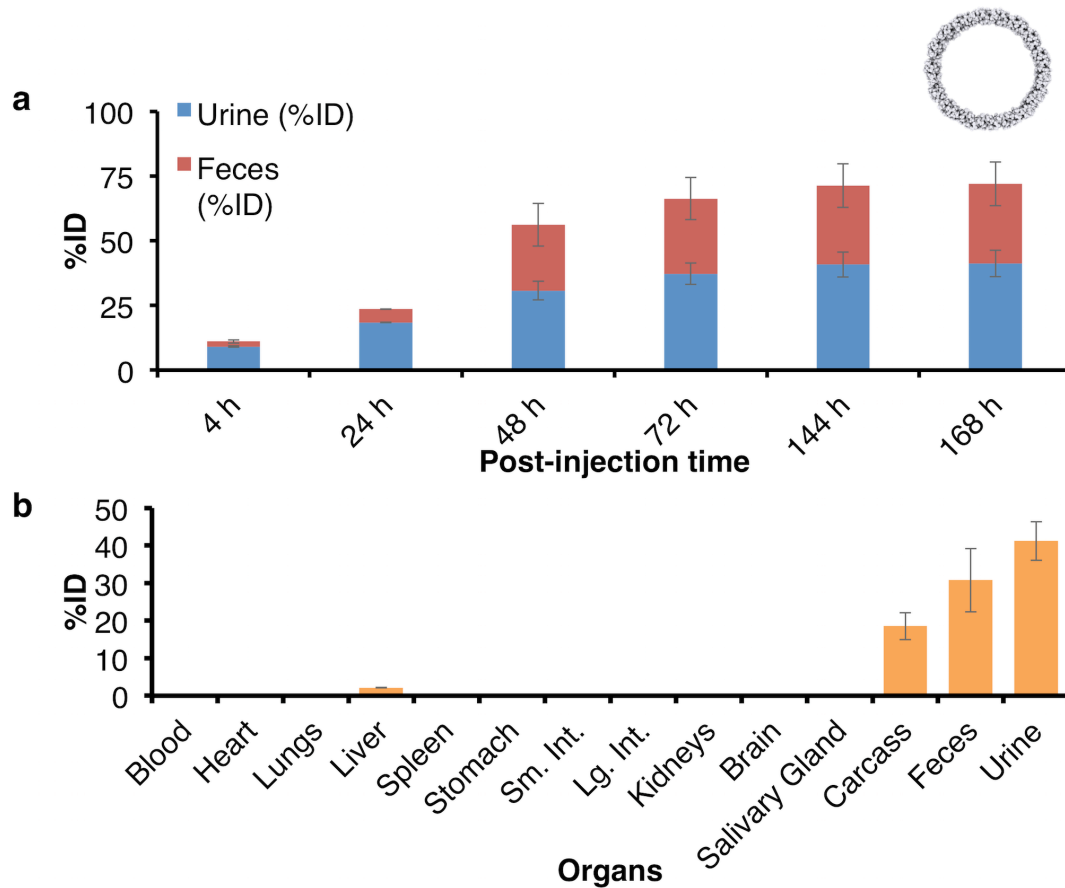


**Figure 4.10:** Metabolic cage study with ultrasmall silica nanorings for the quantitative renal and hepatic clearance analyses (n=2). (a) Total activity change in urine (blue), and feces (red) at different time points after *i.v.* injection. (b) Biodistribution profile from metabolic cage studies 1 week after *i.v.* injection.

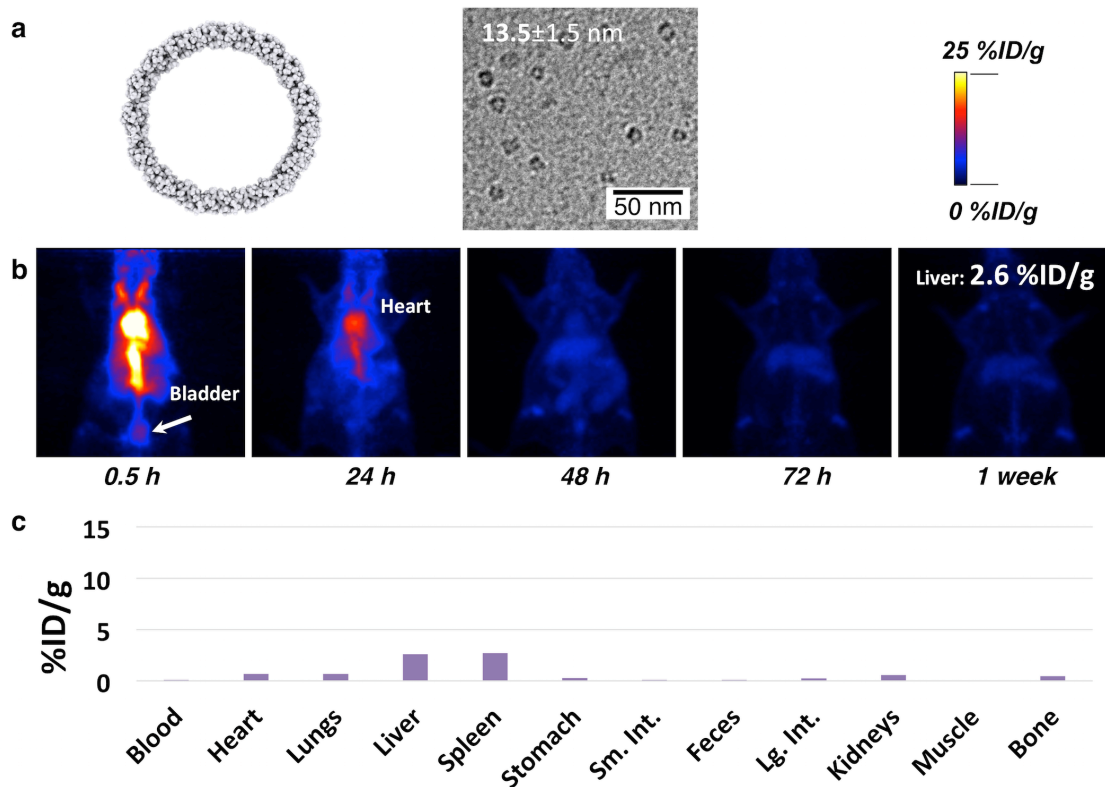


**Figure 4.11:** Studies with 13.5 nm diameter ultrasml silica nanorings. (a) Illustration (left) and TEM image (right) of silica nanorings thwith 13.5±1.5 nm average TEM diameter (from 150 particles) (b) PET images of the same rings as in (a) at 0.5, 24, 48, 72 hours, and 1 week time points after *i.v.* injection showing of 2.6 %ID/g liver uptake at the final time point of 1 week. (c) Biodistribution studies (n=1) on for the same rings at 1 week after *i.v.* injection.

## REFERENCES

1. Watson, J. D.; Crick, F. H. C. Structure of Small Viruses. *Nature* **1956**, *177*, 473–475.
2. Geng, Y.; Dalhaimer, P.; Cai, S.; Tsai, R.; Tewari, M.; Minko, T.; Discher, D. E. Shape Effects of Filaments versus Spherical Particles in Flow and Drug Delivery. *Nat. Nanotechnol.* **2007**, *2*, 249–255.
3. Gref, R.; Minamitake, Y.; Peracchia, M. T.; Trubetskoy, V.; Torchilin, V.; Langer, R. Biodegradable Long-Circulating Polymeric Nanospheres. *Science* **1994**, *263*, 1600–1603.
4. Liu, Z.; Cai, W.; He, L.; Nakayama, N.; Chen, K.; Sun, X.; Chen, X.; Dai, H. In Vivo Biodistribution and Highly Efficient Tumour Targeting of Carbon Nanotubes in Mice. *Nat. Nanotechnol.* **2007**, *2*, 47–52.
5. Ma, K.; Gong, Y.; Aubert, T.; Turker, M. Z.; Kao, T.; Doerschuk, P. C.; Wiesner, U. Self-Assembly of Highly Symmetrical, Ultrasmall Inorganic Cages Directed by Surfactant Micelles. *Nature* **2018**, *558*, 577–580.
6. Choi, H. S.; Liu, W.; Misra, P.; Tanaka, E.; Zimmer, J. P.; Itty Ipe, B.; Bawendi, M. G.; Frangioni, J. V. Renal Clearance of Quantum Dots. *Nat. Biotechnol.* **2007**, *25*, 1165–1170.
7. Du, B.; Yu, M.; Zheng, J. Transport and Interactions of Nanoparticles in the Kidneys. *Nat. Rev. Mater.* **2018**, *3*, 358–374.
8. Huang, X.; Li, L.; Liu, T.; Hao, N.; Liu, H.; Chen, D.; Tang, F. The Shape Effect of Mesoporous Silica Nanoparticles on Biodistribution, Clearance, and Biocompatibility in Vivo. *ACS Nano* **2011**, *5*, 5390–5399.
9. Truong, N. P.; Whittaker, M. R.; Mak, C. W.; Davis, T. P. The Importance of Nanoparticle Shape in Cancer Drug Delivery. *Expert Opin. Drug Deliv.* **2015**, *12*, 129–142.
10. Choi, H. S.; Liu, W.; Liu, F.; Nasr, K.; Misra, P.; Bawendi, M. G.; Frangioni, J. V. Design Considerations for Tumour-Targeted Nanoparticles. *Nat. Nanotechnol.* **2010**, *5*, 42–47.
11. Phillips, E.; Penate-Medina, O.; Zanzonico, P. B.; Carvajal, R. D.; Mohan, P.; Ye, Y.; Humm, J.; Gonen, M.; Kalaigian, H.; Schoder, H.; Strauss, H. W.; Larson, S. M.; Wiesner, U.; Bradbury, M. S., Clinical Translation of an Ultrasmall Inorganic Optical-PET Imaging Nanoparticle Probe. *Sci Transl Med* **2014**, *6* (260), 1-9.

12. Ma, K.; Spoth, K. A.; Cong, Y.; Zhang, D.; Aubert, T.; Turker, M. Z.; Kourkoutis, L. F.; Mendes, E.; Wiesner, U. Early Formation Pathways of Surfactant Micelle Directed Ultrasmall Silica Ring and Cage Structures. *J. Am. Chem. Soc.* **2018**, *140*, 17343–17348.
13. Ma, K.; Mendoza, C.; Hanson, M.; Werner-Zwanziger, U.; Zwanziger, J.; Wiesner, U. Control of Ultrasmall Sub-10 Nm Ligand-Functionalized Fluorescent Core-Shell Silica Nanoparticle Growth in Water. *Chem. Mater.* **2015**, *27*, 4119–4133.
14. Gardinier, T. C., Turker, M. Z., Hinckley, J. A., Katt, W. P., DomNwachukwu, N., Woodruff, F., Hersh, J., Wang, J., Cerione, R., Wiesner, U. Controlling Surface Chemical Heterogeneities of Ultrasmall Fluorescent Core-Shell Silica Nanoparticles As Revealed by High Performance Liquid Chromatography. (2019), *submitted*.
15. Ma, K.; Wiesner, U. Modular and Orthogonal Post-PEGylation Surface Modifications by Insertion Enabling Penta-Functional Ultrasmall Organic-Silica Hybrid Nanoparticles. *Chem. Mater.* **2017**, *29*, 6840–6855.
16. Turker, M. Z.; Gardinier, T. C.; Hinckley, J. A.; Contreras, C. B.; Woodruff, F.; Ma, K.; Kohle, F. F. E.; Wiesner, U. Orthogonal Pathways to Inner and Outer Surface Functionalized Ultrasmall Single-Pore Mesoporous and Fluorescent Silica Nanoparticles as Shown by High-Performance Liquid Chromatography. *Chem. Mater.* 10.1021/acs.chemmater.9b01236
17. Burns, A. A.; Vider, J.; Ow, H.; Herz, E.; Penate-Medina, O.; Baumgart, M.; Larson, S. M.; Wiesner, U.; Bradbury, M., Fluorescent Silica Nanoparticles with Efficient Urinary Excretion for Nanomedicine. *Nano Lett* **2009**, *9* (1), 442-448.
18. Chen, F.; Ma, K.; Zhang, L.; Madajewski, B.; Zanzonico, P.; Sequeira, S.; Gonen, M.; Wiesner, U.; Bradbury, M. S. Target-or-Clear Zirconium-89 Labeled Silica Nanoparticles for Enhanced Cancer-Directed Uptake in Melanoma: A Comparison of Radiolabeling Strategies. *Chem. Mater.* **2017**, *29*, 8269–8281.
19. Eisner, C.; Ow, H.; Yang, T.; Jia, Z.; Dimitriadis, E.; Li, L.; Wang, K.; Briggs, J.; Levine, M.; Schnermann, J.; *et al.* Measurement of Plasma Volume Using Fluorescent Silica-Based Nanoparticles. *J. Appl. Physiol.* **2012**, *112*, 681–687.
20. Shahrjerdi, D.; Bedell, S. W. Extremely Flexible Nanoscale Ultrathin Body Silicon Integrated Circuits on Plastic. *Nano Lett.* **2013**, *13*, 315–320.
21. Yu, M.; Zheng, J. Clearance Pathways and Tumor Targeting of Imaging Nanoparticles. *ACS Nano* **2015**, *9*, 6655–6674.

## CHAPTER 5

### CONCLUSIONS

In this dissertation, the surface chemistry and topology of ultrasmall (hydrodynamic diameter below 10 nm) fluorescent silica nanoparticles was explored in order to generate design criteria for next generation cancer nanomedicines. Three topologies were investigated: spherical, dodecahedral, and ring-type torus-shaped nanoparticles. In the first part, orthogonal surface functionalization pathways were elucidated in order to distinguish the inside and outside surface of silica rings. When engineered appropriately, as evidenced by high performance liquid chromatography (HPLC), hydrophobic cargo could be successfully loaded inside the rings and be “hidden” from interaction with the environment. Careful investigations with HPLC demonstrated, that beyond a specific loading capacity, which depends on the details of the molecular structure, the benefits of the inside of the rings disappear. This is an important insight, which helps define design parameters, *e.g.* when working with hydrophobic and toxic moieties for biomedical applications. The work further demonstrated that HPLC is a powerful and largely unexplored tool to characterize such nano-vehicles for applications in bioimaging and nanomedicine.

The next study explored details of the formation mechanisms of spherical fluorescent silica nanoparticles. Studies revealed that optimized synthesis conditions for full encapsulation of organic chromophores sensitively depend on pH as well as the details of the dyes employed, and can therefore not be easily generalized from one

system to another. In these investigations, HPLC was employed to characterize the surface “patchiness” of ultrasmall fluorescent core-shell silica nanoparticles, which are the result of organic dyes sitting on the surface of the silica core and therefore preventing formation of a homogeneous poly(ethylene glycol) (PEG) shell around the silica core. In turn, employing a silica nanoparticle induced cell death program referred to as ferroptosis as a test bed, it was demonstrated that this patchiness resulted in modulations of the biological response. The work illustrated how important it therefore is, to quantitatively assess surface chemical heterogeneities of such nanomaterials in order to optimize a particular system for a given application in bioimaging or nanomedicine.

Finally, using three distinct topologies of ultrasmall silica nanoparticles, *i.e.* spherical, dodecahedral, and torus-shaped ring structures, and studying their pharmacokinetics (PK) and biodistribution in mice, it was shown that topology has marked effects on biological response including uptake by the reticuloendothelial system (RES), blood circulation time, and renal clearance. In particular, the observation of renal clearance for rings with diameters well beyond the associated cut-off suggested that elastic deformability of such nanoparticle is a parameter that has been largely undervalued. In turn, this suggested that larger rings, which relative to renally clearable spheres provide substantially elevated surface areas for further functionalization with drugs and/or targeting moieties, might provide a viable alternative to more conventional spherical nanoparticles for advanced designs of nanomedicine.

One important outcome of these investigations is the appreciation, that despite many years of research into both synthesis and application of ultrasmall silica nanoparticles, there still remain numerous unexplored fundamental questions. For example, it is still not well established in the field of silica sol-gel chemistry what exactly the surface charge of these clusters is and how it evolves, e.g. as a function of pH. This lack of knowledge is partly due to the lack of appropriate measurement techniques of surface charge for such small and reactive entities. As the synthesis of non-spherical silica nanoparticles around 10 nm in size are becoming more and more common, there is also a growing need for structural characterization tools, as conventional *e.g.* electron microscopy techniques are reaching their limits in terms of material stability under the beam and resulting resolution constraints. Through work in this dissertation, the community becomes more aware of the importance of primary silica clusters in nanoparticle formation, with or without the use of *e.g.* micellar templates. Interaction of these clusters is a really important parameter that governs the final nanoparticle topology, and the surface chemical homogeneity of silica nanoparticles. Having an improved fundamental understanding of the behavior of primary silica clusters would also make it possible to create bio-inspired materials with more sophisticated architectures using different templates under different conditions.

The other important outcome of this dissertation is the effects of topology of clinically relevant inorganic nanoparticles on modulating biological response. Since

the dodecahedron and torus silica nanoparticle topologies investigated here were only discovered relatively recently, and no other similar ultrasmall inorganic materials platform has provided such flexibility in choice of topology, the studies undertaken in this dissertation open a relatively unexplored area of research, which from first results reported here are very promising. Most importantly, based on studies with spherical nanoparticles the renal clearance cut off was thought to be around 3-7 nm. This ignored the fact, however, that nanoparticles with larger dimensions but different topologies like *e.g.* a ring, can deform and thereby successfully pass through glomerular filtration process in the kidney, resulting in renal clearance. This new information opens up many possibilities. Based on these results, silica torus nanoparticles will likely be explored more for tumor targeting, *e.g.* via the enhanced permeation and retention (EPR) effect. They could also be loaded with drug molecules for therapeutic applications. At the same time, micelle templating could be used for other sorts of inorganic compositions, including metals like gold and silver, or transition metal oxides, to produce alternative deformable particle structures.

APPENDIX 1  
SUPPLEMENTARY METHODS

***Gel permeation chromatography (GPC)***

For the precise elution time comparison of reference samples in Figure 3b and samples in Figure 6.3, an automated GPC setup was also used to avoid the operator variations in the sample-loading step. Analytical scale gel permeation chromatography was performed on as made solutions prior to preparative scale GPC purification. Injection volumes were 30  $\mu$ L 15  $\mu$ M C rings diluted with 70  $\mu$ L deionized water. The mobile phase used was the same as for the preparative scale GPC, prepared the same way directly prior to use. The column used was a 300 mm x 7.8 mm Waters BioSuite High Resolution Size Exclusion Chromatography column. The separations were performed under isocratic conditions with a flow rate of 1mL/min. Ring samples eluted within 30 minutes of injection.

***High Performance Liquid Chromatography (HPLC)***

Two separation methods were used for analysis of inside and outside surfaces of C rings; they were as follows:

***For analysis using the 150 mm column***

The sample was first injected onto the column in a flow of 90:10 water:acetonitrile at a flow rate of 0.75 mL/min. These conditions were maintained for 20 minutes to allow equilibration of the analyte with the stationary phase. After 20 minutes the mobile phase composition was changed to 45:55 water:acetonitrile in a step-like fashion and the baseline was allowed to equilibrate. Finally, a composition gradient of 45:55 to 5:95 water:acetonitrile was carried out for 20 minutes, during which the analyte elutes from the column. The analytical run above was followed by a short washing step and column equilibration period to ensure that all material from the previous run had eluted from the column and that the column conditions for the next sample analysis were identical to those for the previous sample analysis. The data was collected and analyzed in Empower 3. The ApexTrack integration algorithm native to the Empower 3 software was used to identify peaks and determine the area percentage associated with each eluting peak. For plotting purposes, data was exported after analysis and baseline subtracted with a blank taken before the chromatographic run using OriginLab.

***For analysis using the 50 mm column***

The sample was first injected onto the column in a flow of 70:30 water (with 0.1 vol% trifluoroacetic acid): acetonitrile at a flow rate of 1.2 mL/min. A linear 30-minute gradient to a final composition of 30 water (0.1 vol% TFA):70 acetonitrile was started immediately following injection of a C ring sample. The column was washed

with a composition of 5 water (0.1 vol% TFA): 95 acetonitrile to ensure that all materials eluted. After the washing step the column was equilibrated to the initial run conditions for 5 minutes before the next injection. The data was collected and analyzed in Empower 3. The ApexTrack integration algorithm native to the Empower 3 software was used to identify peaks and determine the area percentage associated with each eluting peak. For plotting purposes, data were exported after analysis and baseline subtracted with a blank taken before the chromatographic run using OriginLab.

Supplemental Figure 1 shows the comparison of the methods on the analysis of the C ring samples from Figure 3 and 4, using 150 mm, and 50 mm columns, named Method 1, and Method 2, respectively. Unless otherwise stated, Method 2 is used as the primary HPLC protocol.

### ***Fluorescence Correlation Spectroscopy (FCS)***

FCS experiments were performed on a home-built instrument inspired by a confocal microscope setup as described previously.<sup>34, 35</sup> A 635 nm solid state diode laser was used as excitation source (excitation intensity 5 kW/cm<sup>2</sup>) for the Cyanine5 dye and Alexa Fluor 647 was used to align and measure the size of the confocal volume due to its known diffusion coefficient.

Data was collected in sets of five consisting of five 30 s runs each then fit to a correlation function,  $G(\tau)$ , accounting for translational diffusion, as well as for fast photophysical processes, as shown in equation (6.1):

$$G(\tau) = 1 + \frac{1}{N} \cdot \left(1 + \frac{\tau}{\tau_D}\right)^{-1} \cdot \left(1 + \frac{\tau}{\kappa^2 \tau_D}\right)^{-1/2} \cdot \frac{1}{1-A} \cdot (1 - A + A \cdot e^{-\tau/\tau_A}) \quad (6.1)$$

Here,  $N$  is the mean number of particles within the detection volume, and  $\kappa$  is the structure factor calculated from a known diffusion coefficient and given by  $\kappa = \omega_z/\omega_{xy}$ , where  $\omega_{xy}$  and  $\omega_z$  are the radial and axial radii, respectively, of the observation volume.  $\tau_D$  is the characteristic diffusion time of a particle through the observation volume.  $\tau_D$  is defined as  $\tau_D = \omega_{xy}^2/4D$ , where  $D$  is the respective particle diffusion coefficient.  $A$  is the time- and space-averaged fraction of fluorophores undergoing fast photophysical processes such as photoisomerization that must be accounted for to achieve a good fit and  $\tau_A$  is the characteristic relaxation time that is related to the fast photophysical process. The Stokes-Einstein relation was applied to determine particle diameters, equation (6.2):

$$d = 2 \frac{k_B T}{6\pi\eta D} \quad (6.2)$$

with  $k_B$  being the Boltzmann's constant,  $T$  being the absolute temperature, and  $\eta$  being the dynamic viscosity. The average number of dyes per particle,  $n$ , was calculated according to equation (6.3):

$$n = \frac{C_{\text{dye}}}{C_{\text{particle}}} \quad (6.3)$$

Here  $C_{\text{dye}}$  is the measured dye concentration derived from the dye extinction coefficient using the relative absorbance, and  $C_{\text{particle}}$  is the particle concentration determined by FCS.

Supplementary Figures

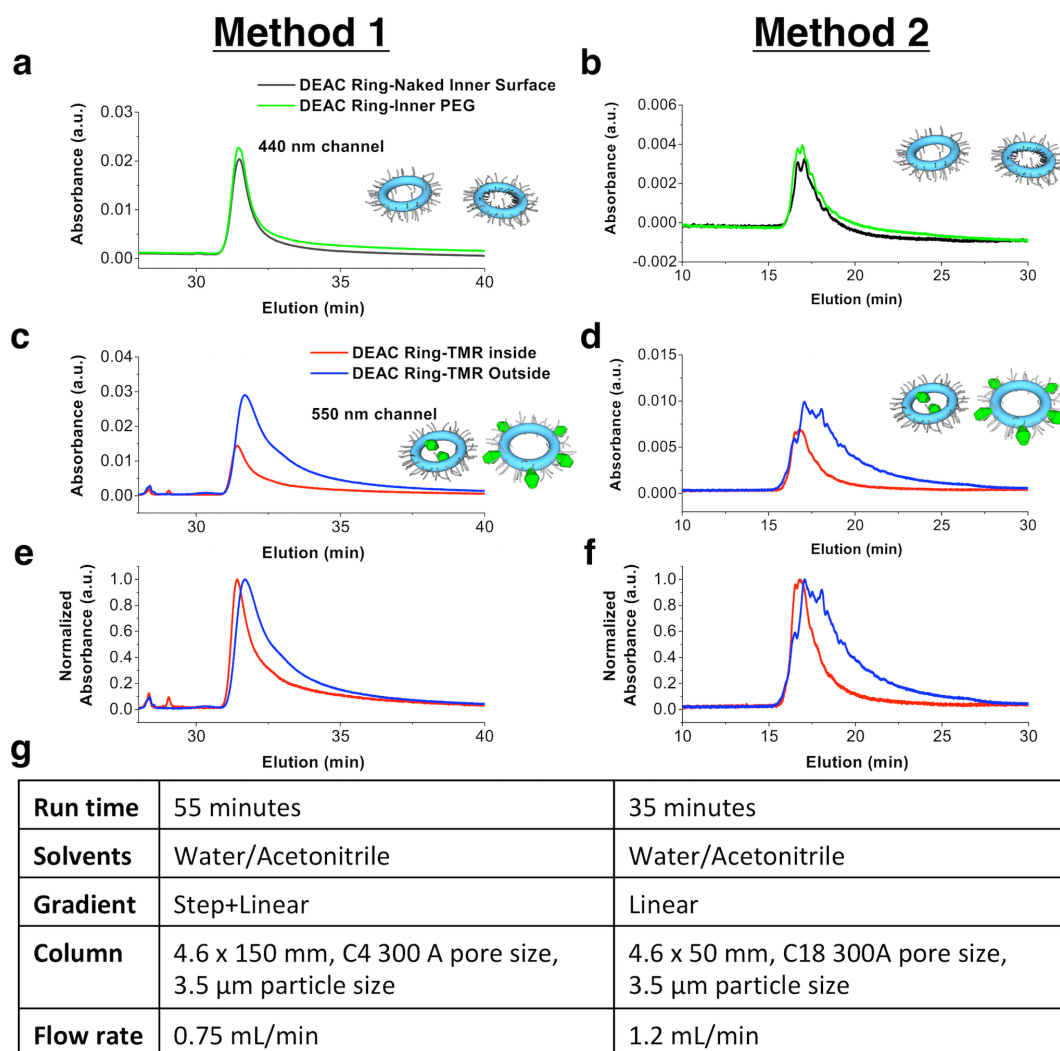


**Figure 6.1:** Comparison of results from HPLC Method 1 (left) and Method 2 (right) applied to different ring batches. (a,b) Comparison of DEAC-rings with and without inner surface PEGylation, and (c,d) DEAC-rings with inside and outside TMR-functionalization, respectively. (e,f) Same data as in (c,d) but normalized to same maximum absorbance. (g) Comparison of parameter sets used for the two HPLC methods.

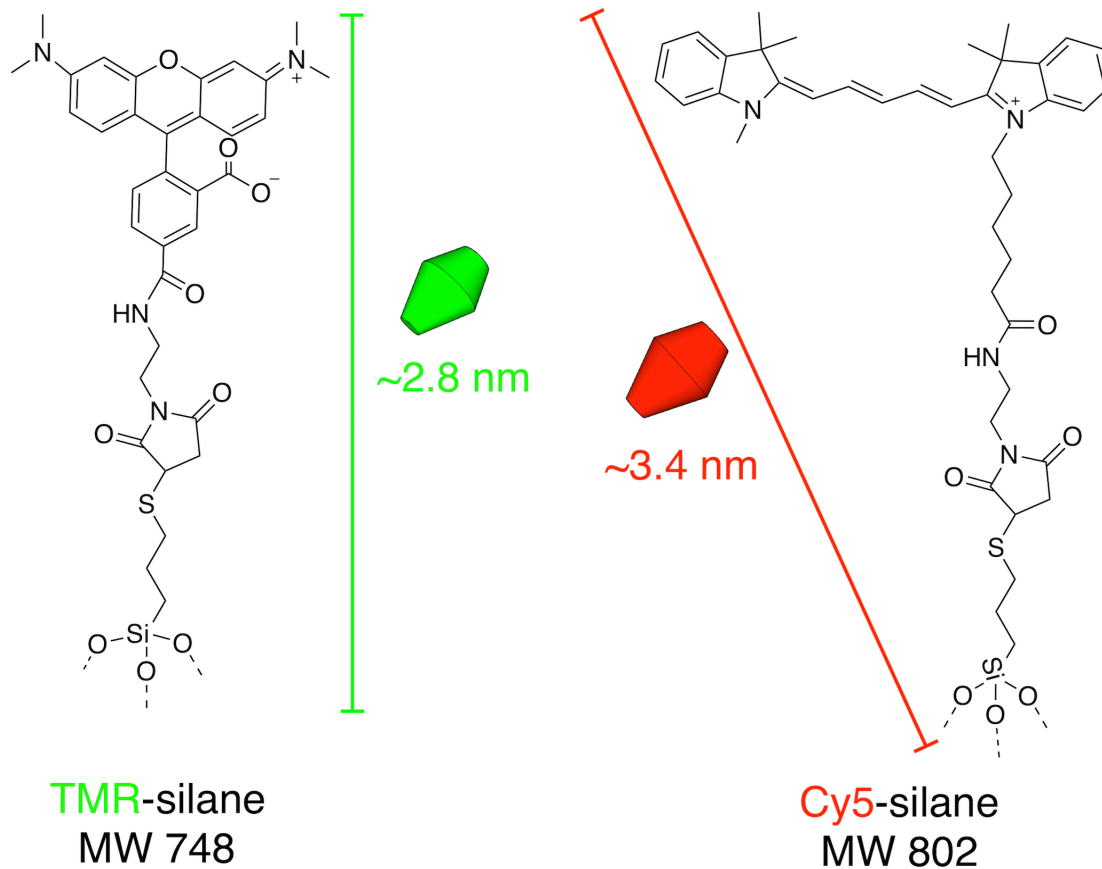


**Figure 6.2:** Molecular structures and dimensions of “stretched” TMR-silane (left) and Cy5-silane (right) dye conjugates.

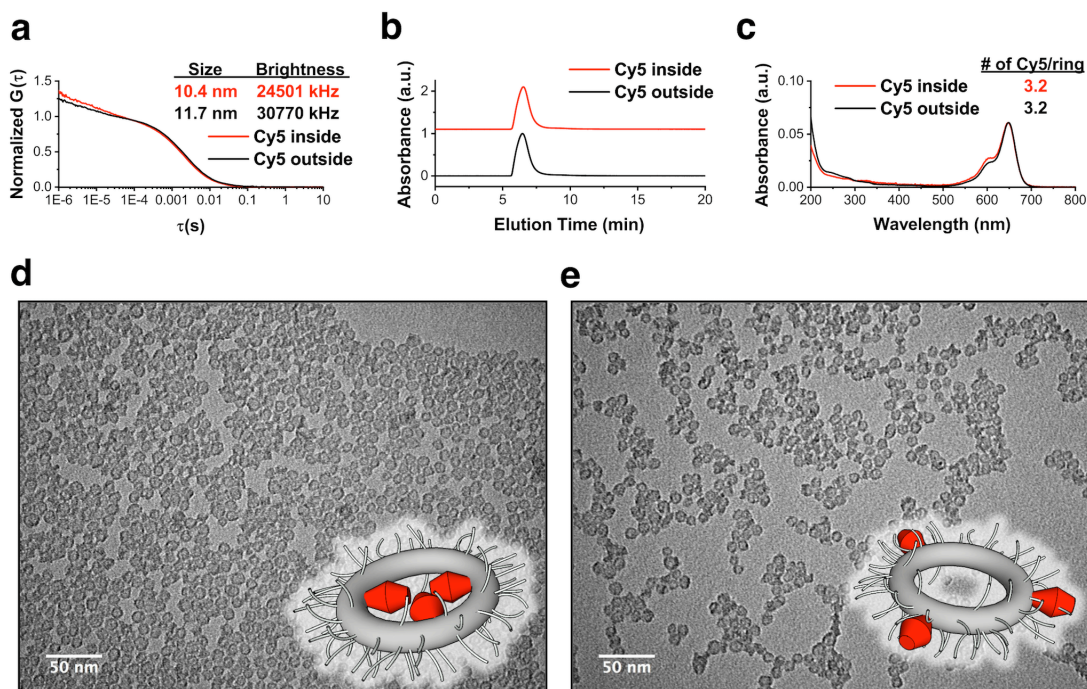


**Figure 6.3:** Characterization of plain rings (*i.e.* no DEAC in the silica ring matrix) with inner and outer surfaces functionalized with Cy5 dye. (a) FCS auto-correlation curves of inside (red) and outside (black) Cy5 functionalized silica nanorings suggesting 10.4 nm and 11.7 nm hydrodynamic sizes, and brightness as photon counts of 24501 kHz and 30770 kHz, respectively. (b) GPC chromatograms at 647 nm read out channel (Cy5 dye absorption) of batches in (a). (c) Absorption spectra of the same batches as in (a) normalized to the maximum Cy5 absorption. Combined with FCS results these features translate to the same Cy5 dye number per ring of 3.2 for both samples. The increase in absorption of the shoulder on the left of the main Cy5 absorption peak observed for the inside functionalized rings (red) suggests increased non-radiative energy transfer between dyes in close proximity, consistent with decreased brightness as measured by photon counts in FCS shown in (a). (d, e) TEM images of inside (d) and outside (e) Cy5 functionalized silica nanorings. Insets show illustrations of the Cy5 dye (red) functionalized and PEGylated silica nanorings (grey color indicates that there is no DEAC dye covalently incorporated into the silica matrix of the rings).